Politecnico di Milano
SCHOOL OF INDUSTRIAL AND INFORMATION ENGINEERING
Master of Science – Mechanical Engineering

A modified actuator line model for the optimization of wind farm simulations

Supervisor
Prof. Paolo SCHITO

Co-Supervisor
Ing. Claudia MUSCARI

Candidate
Luca GAJONI–928679

Academic Year 2020 – 2021

Ringraziamenti

Giunto alla conclusione di questo lavoro, vorrei esprimere tutta la mia gratitudine alle persone che mi hanno accompagnato durante questo percorso di ricerca.

Vorrei innanzitutto ringraziare il mio relatore, il Professor Paolo Schito, per avermi guidato, ascoltato e aiutato durante tutto il lavoro.
Un grande grazie va anche all'Ing. Claudia Muscari per i suoi preziosi consigli che mi hanno permesso di superare diversi ostacoli.
Sono grato inoltre al Professor Giacomo Persico e al Professor Vincenzo Dossena. Le conoscenze apprese grazie a loro sul mondo della CFD e dell'eolico mi hanno permesso di affrontare questo lavoro con una maggiore preparazione e più consapevolezza.

Un enorme grazie va alla mia famiglia, in particolare ai miei genitori, Chiara e Gherardo, e a mio fratello, Paolo. Il loro affetto e supporto sono stati fondamentali durante questi anni universitari. Il loro costante sostegno mi ha aiutato a superare anche i momenti più difficili.

Grazie agli amici di una vita e non. I momenti passati con loro, di grande spensieratezza e ricchi di risate, hanno reso il percorso universitario più leggero e sereno.

Grazie ai miei compagni di università. Con loro ho condiviso fatiche e affanni, ma anche gioie e soddisfazioni.

Grazie a Filippo, un grande amico. Le giornate trascorse con lui a confrontarsi sui rispettivi lavori sono state di enorme aiuto per arrivare fin qui.

Infine grazie a Giulia, per la sua pazienza, il suo affetto e il suo costante supporto.

Sommario

L'importanza dell'utilizzo dell'energia eolica per la produzione di potenza è costantemente aumentata negli ultimi decenni. L'impossibilità di studiare questo settore solo sperimentalmente, specialmente quando è necessario occuparsi di interi parchi eolici, ha portato allo sviluppo di diversi metodi per simulare il funzionamento delle turbine eoliche. La CFD (Computational Fluid Dynamics) assume un ruolo fondamentale in questo contesto. Tuttavia metodi basati solo su di essa, i cosiddetti Fully Resolved (FR) methods, in cui l'intera geometria della macchina viene ricostruita, rischiano di essere estremamente pesanti dal punto di vista computazionale. Esistono però anche metodi, come il BEM (Blade Element Momentum), che non fanno uso della CFD. Nonostante il suo basso costo computazionale, il BEM ha però il grande limite di non riuscire a rappresentare in modo realistico le condizioni del flusso all'ingresso della turbina. I metodi ibridi (Actuator Disk Method (ADM) e Actuator Line Method (ALM)) cercano dunque di combinare l'accuratezza dei metodi basati solo sulla CFD con il basso costo computazionale del BEM. La vera geometria della turbina non viene ricostruita all'interno del dominio, ma la sua presenza è simulata da un certo numero di punti attuatori, su cui delle forze vengono applicate. La CFD ha il ruolo di risolvere il flusso, ricavando le condizioni all'ingresso della macchina. In questo modo le forze scambiate possono essere calcolate mediante dei valori tabulati. Queste forze vengono poi diffuse nella zona che circonda le linee (o il disco), al fine di evitare instabilità di tipo numerico.

Una delle maggiori carenze dei metodi ibridi è la forte dipendenza dei risultati finali dalla dimensione caratteristica della funzione gaussiana utilizzata per diffondere le forze nel dominio. Tramite studi precedenti ([1], [2]) il suo valore ottimale è stato definito pari a $\epsilon_{ott} = 0.25\ corda$. Questo valore permette di ottenere come output delle simulazioni delle performance molto simili a quelle reali. Tuttavia, specialmente quando interi parchi eolici vengono simulati, esso è difficilmente raggiungibile e valori maggiori devono essere considerati. Nel 2018 Martìnez Tossas e Meneveau [3] hanno sviluppato un modello basato sulla cosiddetta *Filtered Lifting Line Theory*, in grado di rendere i risultati di una simulazione svolta mediante l'ALM indipendenti dalla suddetta dimensione caratteristica. I due autori hanno testato il modello con profili statici, caratterizzati da differenti distribuzioni di corda, ottenendo promettenti risultati indipendenti dal valore di ϵ. Mediante questo lavoro di Tesi, si è voluto implementare il modello in SOWFA (Simulator for Offshore Wind Farm Applications), uno strumento di simulazione sviluppato da NREL (National Renewable Energy Laboratory), che fa uso dell'ALM. L'obiettivo era quello di raggiungere l'indipendenza dalla ϵ anche nel caso di turbine eoliche. Due macchine sono state testate: la turbina NREL-5MW e la versione ridotta in scala della turbina DTU-10MW.

I risultati ottenuti dalle simulazioni si sono dimostrati promettenti ed in linea con le aspettative, tuttavia l'introduzione del modello in SOWFA dovrà essere approfondita maggiormente in lavori successivi.

Parole chiave: Energia eolica, CFD, Actuator Line, funzione gaussiana, Filtered Lifting Line Theory, SOWFA

Abstract

The importance of wind energy has increased more and more during the last decades. The impossibility to study this field only experimentally, especially when the behaviour of large wind farms has to be investigated, has brought to the introduction of many different methods for simulating the operation of the machines. Computational Fluid Dynamics (CFD) plays a fundamental role. However methods based only on CFD, the so called Fully Resolved (FR) methods, in which the entire geometry is reconstructed, may be extremely expensive from a computational point of view. On the opposite side there are some methods, like the Blade Element Momentum (BEM) method, that do not make use of CFD. Although its very reduced computational cost, the BEM method has the important limit not to allow a realistic representation of the conditions of the incoming flow field. Hence, the hybrid methods (the Actuator Disk Method (ADM) and the Actuator Line Method (ALM)) try to combine the accuracy of the FR methods with the limited computational cost of the BEM, in order to gain as much as possible from both these two categories. The real geometry of the turbine is not reconstructed inside the computational domain, but its presence is mimicked by a certain number of actuator points on which some forces are applied. CFD has the role of resolving the flow, obtaining the conditions at the inlet of the machine. In this way the exchanged forces can be computed (thanks to some tabulated values). These forces are then spread over the lines (or the disk) in order to avoid numerical instabilities.

One of the biggest weakness of the hybrid methods is the extreme dependence of the final solution from the width (ϵ) of the Gaussian projection function chosen in order to spread the forces. From previous studies ([4], [2]) its optimal value was found equal to $\epsilon_{blade,opt} = 0.25\ chord$. This value allows to reach evaluated performances very close to the real ones. However, especially when wind farms are simulated, this value is very difficult to be reached and much bigger values are considered. In 2018 Martìnez Tossas and Meneveau [3] developed a model based on the *Filtered Lifting Line Theory*, able to make the results of a simulation performed using the ALM independent of the Gaussian projection function width. They tested the model with static wings, characterized by different chord distributions, obtaining very good results independent of the ϵ value.

The aim of this thesis was to implement the model in the Simulator for Offshore Wind Farm Applications (SOWFA), a simulating tool developed by the National Renewable Energy Laboratory (NREL), that makes use of the ALM. The objective was to try to make the simulations independent of the ϵ value, also in the case of a wind turbine. The model was tested with two different machines: the NREL-5MW wind turbine and the scaled representation of the DTU-10MW reference wind turbine.

The results obtained from the simulations have been shown to be promising and consistent with the expectations. Nevertheless, the introduction of the model in SOWFA will have to be further investigated in future works.

Keywords: Wind energy, CFD, Actuator Line, gaussian projection function width, Filtered Lifting Line Theory, SOWFA

Contents

List of Figures

List of Tables

Chapter 1

Introduction

The huge quantity of fossil fuels based plants spread all over the world is the main source of pollution affecting our planet. They in fact loads in a very heavy way the atmosphere with toxic chemicals (like sulfur dioxide, carbon dioxide and oxides of nitrogen) that are generated during the energy conversion process. This causes phenomena that can be very dangerous. Sulphur dioxide and nitrogen oxides released into the atmosphere cause acid rains that are able to creates severe health and environment impacts and to damage buildings and structures as well. Moreover, a very high percentage of the global emission of CO_2 is due to burning of fossil fuels. The accumulation of CO_2 in the atmosphere causes green house effect. Green house gases allow the rays of the sun to enter the atmosphere but trap the reflected infrared radiation. The atmosphere gets warmer (global warming), the weather pattern changes, the sea level rises and the land configuration is altered. The necessity to try to limit the global warming and the pollution in order to preserve our planet, together with the continuously increasing in the energy demand and the limited reserves of fossil fuels, push the countries towards clean and renewable resources to obtain power. The wind can be seen as the best choice to play this role. Wind energy systems are able in fact to avoid the generation of polluting gases and harmful particulates, meeting our energy demand in a sustainable and environment-friendly way. These are the reasons for which during the last decades the importance of wind energy has grown more and more. Nowadays a huge number of researchers work everyday in order to get as much as possible from the wind potentialities and a bigger and bigger number of wind turbines, both onshore and offshore, are installed all over the world.

1.1 Historical remarks

Historically, people always tried to govern the force of the wind. They exploited it for the propulsion of ships using sails, for grinding grain or to pump water for irrigation and later to obtain electricity.

Some believe that the first attempts of using wind for mechanical power date back to the reign of the Babylonian emperor Hammurabi during which its strength was used for some irrigation projects during the 17^{th} century B.C. . Others think that the wind was exploited for the first time in India during the 4^{th} century. However, the first documented project of wind mills dates back to the Persian empire of the year

200 B.C. . They were constituted by vertical axis machines and were used in order to grind grains.
Starting from the 13^{th} century, grain grinding mills became popular also in most of Europe. Differently from the Persian design, European machines had horizontal axis. The rotor was manually oriented to the wind direction and the mill was protected against too strong winds by turning the rotor in a position different from the one normal to the wind direction. The interest for this type of machines grew more and more, especially in Holland where rotors were equipped with crude airfoil profiles in order to improve the efficiency of the mill. Starting from the middle of the year 1700, these machines reached America too, thanks to the Dutch settlers.
Thanks to the continuously increasing knowledge about this topic, other applications could be possible. The American multi bladed wind turbine appeared for the first time by the mid-1800. Its main role was to pump water for the agriculture. Over six millions of such units were installed in US between 1850 and 1930.
The first wind turbine designed in order to generate electricity was built in Denmark in 1890. Starting from 1910, thanks to the higher and higher efficiency of the aerodynamically designed blades, a lot of such machines were employed in order to give electricity to the villages in Denmark.
As the years go by, the technology at the basis of wind turbines improved more and more and in 1931 a 100 kW turbine was installed on the Caspian sea shore. After it many experimental wind plants were constructed in many countries and in 1941 a large-scale 1250 kW turbine was installed in Vermont. The machine worked for five years, until the blades failed in 1945. This installation was a big success because it demonstrated the feasibility of large-scale wind-electric generation.
Many other designs were experimented in this period. For example, two vertical axis wind turbines were invented: the Darrieus and the Savonius turbines. Moreover other materials, like the fibre glass, were tested in order to construct the blades.
Unfortunately, especially in 1970, the cost of electricity from fossil fuels became more and more tempting and the interest in wind energy declined gradually. However, the oil crisis of 1973 was fundamental in order to understand the importance of using renewable resources. The role of the wind was enhanced once again and people restarted to exploit as much as possible its strength. During the last decades, in fact, the steps in this field were enormous and nowadays wind energy is seen as one of the best solution in order to fight against the global warming and the pollution that affects our planet.

1.2 Current and possible future scenarios

Historically 2020 was the best year ever for the global wind industry: with the installation of more than 90 GW of wind power a growth year-to-year of 53% was observed. 2020 was also the year during which renewables generated more electricity in the EU than fossil fuels, powered by 14.7 GW of new wind plants. In a so difficult year for the entire humanity and for most of the sectors of the global economy, affected by the COVID-19 pandemic, the resilience and the strength of the wind industry has been demonstrated. The huge number of new installations brought the global cumulative wind power capacity to 743 GW. Considering only the onshore market, an increase of 59% with respect to 2019 occured. China and US were the two countries where wind industry grew most and together they increased their market share from 15% to 76%. For what regards the regional level, the biggest success was registered in Asia Pacific, North America and Latin America. Together the three regions installed a total of 74 GW of new onshore wind capacity (76% more than the previous year). Europe instead saw only a growth year-to-year of 0.6%, whereas in Africa and Middle East the number of new installations was almost the same of 2019. The world's top five markets in 2020 for new installations were China, the US, Brazil, Netherlands and Germany.

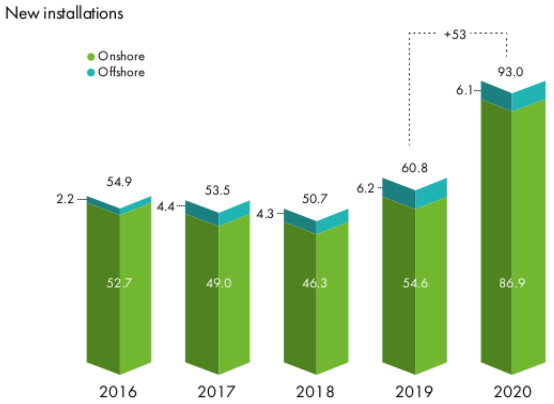

Figure 1.1. Amount of new installations from 2016 to 2020

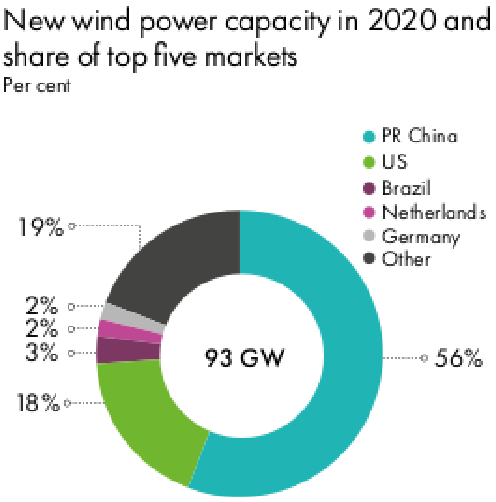

Figure 1.2. Share of the new wind power capacity among the top five markets

For the Global Wind Energy Council (GWEC) Market Intelligence [5] also the next years will be promising. The outlook is based on input from regional wind associations, government targets, available project information and input from industry experts and GWEC members. 469 GW of new onshore and offshore wind capacity is expected to be installed in the next five years. Especially a steep increase for the offshore installations was forecasted. Offshore's market share in global new installations is expected to grow from the current 6.5% to 21% in 2025.

Next years will be fundamental in order to limit global warming to “well below” 2°C, as set out in the Paris Agreement. EU, Japan, South Korea, Canada and South Africa pledged to reach net Green House Gases (GHG) emissions by 2050, China set its target by 2060 and US expressed the intention to reach net zero by 2050. These countries now represent 63% of global GHG emissions. 2021 is an extremely important year that must be characterized by concrete policy interventions, interim target-setting and robust delivery plans, otherwise it will be impossible to reach these targets. Important decisions must be taken and practical solutions must be adopted. This will be the only way in order to preserve our planet.

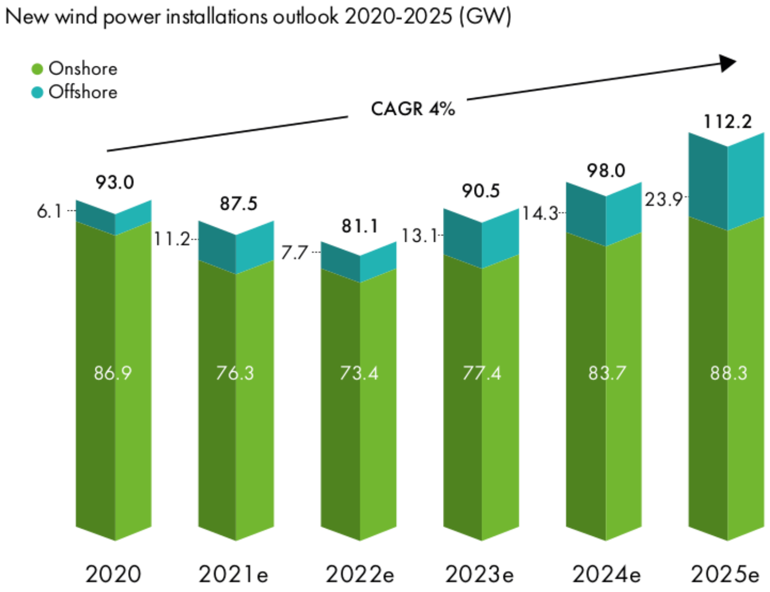

Figure 1.3. New wind power installations outlook until 2025

1.3 Wind turbines modelling and reasons behind this work

A big obstacle to the diffusion of the wind energy industry has always been the difficulty in modelling and testing the wind turbines operation. The experimental approach cannot be used as often as it would be necessary. It needs in fact a huge use of resources and often a very big amount of time. Moreover it does not allow to test whatever configuration and the number of machines that can be observed during an experimental test is very limited. An entire wind farm obviously cannot be study following an experimental approach. For these reasons, Computational Fluid Dynamics (CFD) plays a fundamental role in this field. Since its introduction in this sector it has led to enormous advantages. However, even in the case of the application of the CFD tools, the time required in order to perform the simulations can be extremely high. If one in fact wants to represent the real geometry of the simulated machine inside the computational domain, the total number of cells increases a lot. This happens because all the very small turbulent structures (characterized by different scales) near the blades (such as the boundary layer) need to be captured. When the number of wind turbines to be simulated at the same time becomes relevant, the computational time increases dramatically and this could make the simulations unfeasible. All these problems brought to the introduction of other methods. They can be considered hybrid methods because they are able to combine the efficiency of the BEM (whose principles will be explained in the next chapter) and the precision of CFD. They are the actuator disk method (ADM), presented for the first time by Sørensen in [6], and the actuator line method (ALM), introduced by Sørensen and Shen in [7]. A comparison with some experimental results that highlights the differences among the three methods can be found in [8]. The big advantage of the ADM and of the ALM lies in the fact that they do not consider the real geometry of the machine, but its presence is mimicked by the application inside the computational domain of the forces exchanged by the blades. These forces are placed in correspondence of some actuator points spread over a disk, in the ADM case, or along lines, in the ALM case. The two methods will be deeply described in 3.5. In this thesis work the attention will be put on the actuator line method. This approach was in fact the one chosen for performing the simulations.

Although all the great advantages obtained by the introduction of the ALM, there are still some big limitations. The results coming from the application of this method, in fact, highly depend on the set parameters that characterize it. For example, the way in which the incoming velocity is sampled could influence the final results. Usually it is sampled in correspondence of the actuator points (local sampling), but other approaches were presented in different works ([9], [10], [11], [1], [12], [13]). Also the number of actuator points along each actuator line (representing the blade) could cause some variations in the obtained performance. Typically, as can be read for example in [14], the blade is discretized into 25-40 points. Nevertheless, probably the parameter that most influences the outputs of the simulation is the width (ϵ) of the gaussian function used for projecting the forces. The computed forces in fact are not simply applied to the actuator points, but they are also spread inside the computational domain. The higher is the ϵ value the wider is the zone influenced by the presence of the forces. Unfortunately, the variation of the extension of the affected zone with the value of ϵ, also causes a variation of the generated turbulent structures, that, in turn, affect the final outputs of the simulation. Many studies were performed in order to reach an optimal value for the gaussian projection function width able to reproduce turbulent structures as close as possible to the real ones [14], [1], [4], [15], [2]. The main problem is that the optimal value for the width of the gaussian function is very small with respect to the dimensions of the domain, especially if one wants to simulate a certain number of machines. In this case the optimal value cannot be reached, much bigger values of ϵ must be used and this introduces many inaccuracies inside the final results, due to their dependence from the gaussian projection function width. In 2019 Martinez and Meneveau tried to find a solution to this problem [3]. They developed a model, based on the *Filtered Lifting Line Theory*, able to bring the actuator line method to the optimal results, whatever is the ϵ value. The objective of this thesis work was to implement this model inside SOWFA, the Simulator for Offshore Wind Farm Applications, that is the tool chosen for performing the simulations. The description of the model, its implementation in SOWFA and the analysis of the obtained results are contained in the next chapters. The objective was to obtain outputs independent of the ϵ value and as close as possible to the ones that can be reached with the optimal

value of the gaussian projection function width (and so to the real ones).
Finally, another important aspect able to influence, even in a very heavy way, the final results of a simulation is the grid resolution. This is not a specific problem related to the ALM, but it characterizes any simulation, based on CFD, in which a certain computational domain needs to be analysed. The only way to ensure that the mesh has no effects on the outputs is to reach the grid independence. However, this is not always possible, especially when wind farms consisted by several machines are treated. In that case, in fact, the number of cells would increase dramatically, together with the time required for performing the simulations. This would make them unfeasible from a computational point of view. In SOWFA, as can be read in [1], a finer mesh generates an increase in the resultant power. For this reason, two levels of grid refinement for both the machines considered for this thesis were tested. This was done in order to see if the model is able to have any effect also on the way in which the mesh influences the results. The aim is to try to obtain a final solution that is independent not only of the gaussian projection function width, but also of the grid resolution that characterizes the computational domain taken into account.

Chapter 2

Wind turbines overview

2.1 2D aerodynamics principles at the basis of wind turbines operation

Aerodynamics principles govern the way in which the forces are exchanged along the blades of a wind turbine. Each blade can in fact be represented as a huge number of sections, each of them characterized by a specific aerodynamic profile (airfoil). A simple sketch showing some sections along a generic blade can be observed in Figure 2.1.

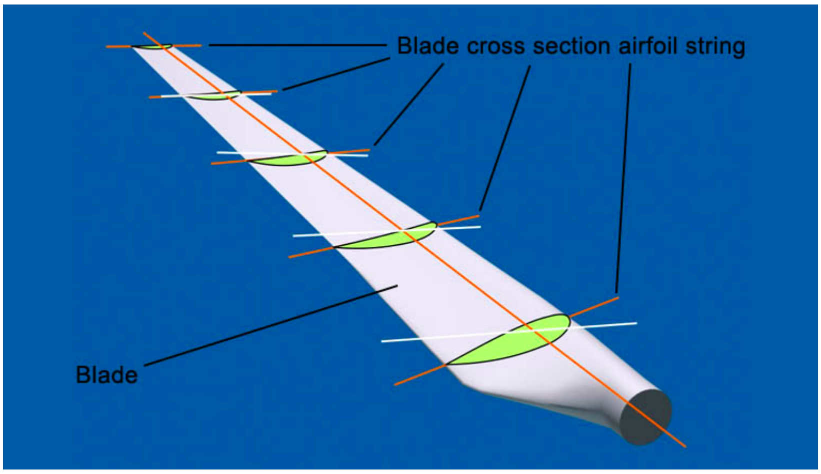

Figure 2.1. Some highlighted sections of a generic blade

Due to the fact that the blades are long and slender structures, the component of the velocity in the spanwise direction is much lower than the component in the streamwise direction and the flow can be usually considered as two-dimensional in correspondence of each section. Actually, the flow would be two-dimensional only with a blade of infinite length. In reality in fact the blades are characterized by a finite length, that causes some three-dimensional effects at the extremities (these phenomena will be better explained in the next chapters). Nevertheless, the 2D approximation is acceptable for most of the radial positions and different types of corrections are used for the sections where the 3D effects are more relevant.

Focusing now only on one generic section of the blade and neglecting all 3D effects, it is possible to describe the interaction between the wind and the blade by considering an airfoil subjected to an incoming flow (for a wind turbine the incoming velocity to the blade is the relative one, that takes into account the rotation of the blades). The airfoil experiences a force that depends on the angle of attack, so the angle between the undisturbed incoming velocity (the one not influenced by the generation of the bound vortex around the airfoil) and the chord of the profile. This force can be seen as the sum of two different forces: the first one parallel to the undisturbed velocity (the drag force) and the second one perpendicular to it (the lift force). For an aerodynamic profile it is of fundamental importance that the lift force is much higher than the drag force. In the case of a wind turbine for example it is in fact the force responsible for the generation of the torque and so the one that allows the extraction of power from the machine. The drag force, instead, is a resistance force and so it must be minimized in order to maximize the efficiency. From the definition of the lift and of the drag it is possible to define two other quantities: the lift coefficient and the drag coefficient. They can be respectively computed as:

$$C_L = \frac{L}{\frac{1}{2}\rho V_0^2 S} \tag{2.1}$$

$$C_D = \frac{D}{\frac{1}{2}\rho V_0^2 S} \tag{2.2}$$

Where L is the lift, D is the drag, ρ is the density of the air, V_0 is the undisturbed incoming velocity and S is the area of the profile.
In Figure 2.2 it is possible to observe the angle of attack and the forces generated on a generic profile.

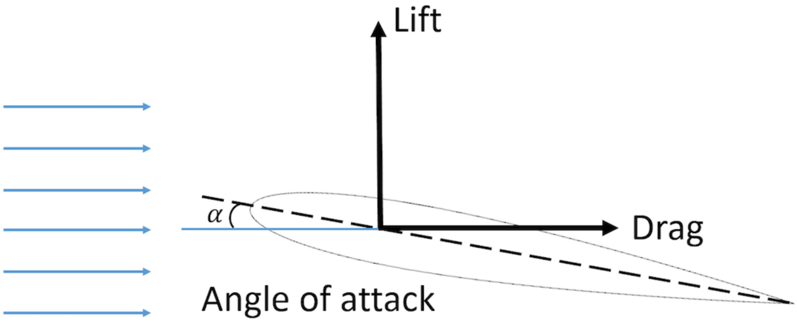

Figure 2.2. A generic profile subjected to an incoming flow

The force felt by the profile is generated by a difference in pressure between its two sides. The upper side in fact, called suction side, is characterized by a negative pressure distribution that pulls the airfoil, whereas the lower side, called pressure side, is subjected to a positive pressure distribution that pushes it. The contribution of the suction side to the total force generated is considerably higher than the one of the pressure side.

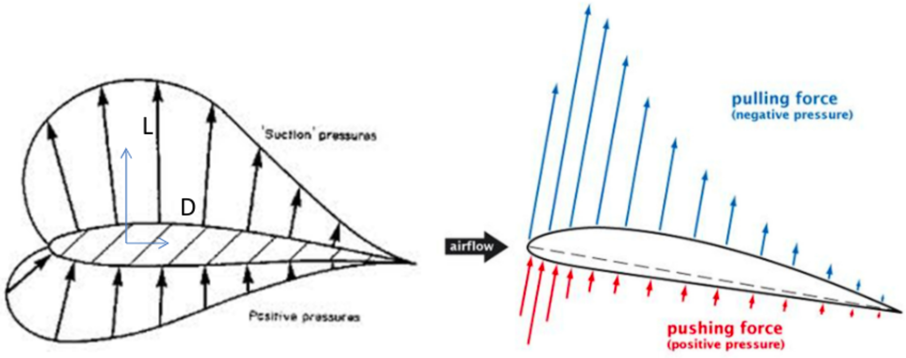

Figure 2.3. Pressure distribution on a profile

The intensity of the force generated on the aerodynamic profile mainly depends on the value of the angle of attack. The higher it is, the higher the force magnitude becomes. This is mainly due to the fact that the lift increases with the angle of attack, whereas the drag force remains constant for a quite large range of angles. However, at a certain angle a steep decrease of the lift occurs and a huge increase of the drag is observed. The efficiency rapidly decreases and the performances become worse and worse. This phenomenon is called stall. This happens for the presence of an adverse pressure gradient in correspondence of the rear part of the suction side of the profile. In fact when the flow approaches the airfoil, at the suction side it first experiences a positive pressure (and so it is accelerated), followed by a negative pressure gradient (and so it is decelerated). The higher the angle of attack, the higher the magnitude of these two pressure gradients. At a certain point the adverse pressure gradient becomes too high, the flow can no more remain attached to the profile and a detachment occurs. This represents the phenomenon of the stall. In figure 2.4 a sketch representing an airfoil subjected to stall is reported, whereas in figure 2.5 it is possible to observe the increase of the lift coefficient of a generic profile until the critical angle of attack and its sudden decrease after it.

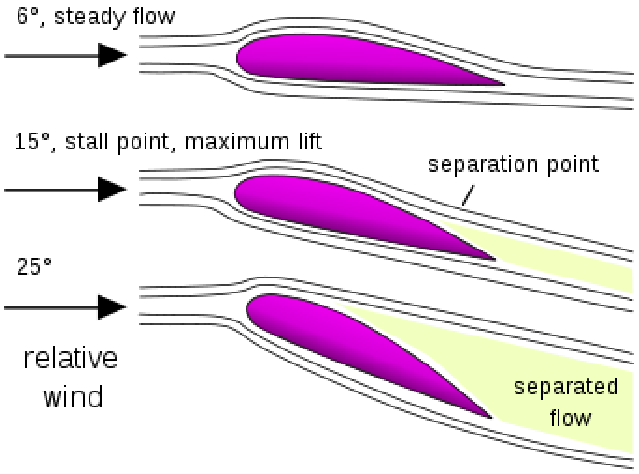

Figure 2.4. Stall phenomenon generated by increasing the angle of attack

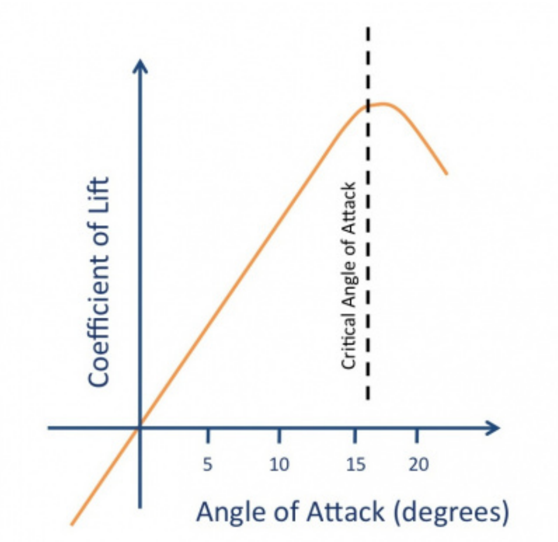

Figure 2.5. Trend of the lift coefficient function of the angle of attack

Obviously the phenomenon of stall is something that needs to be avoided in a wind turbine. It in fact not only causes a huge decrease in the performances, but it can bring to structural damages too.

2.2 Theories and methods for modeling the wind turbines operation

The need of modeling in a more and more accurate way the operation of a wind turbine has always been of fundamental importance. The way in which the flow interacts with the rotor of the machine has been deeply studied and a very huge variety of methods and theories behind it was developed. In the next sections some of the methods used in the past decades will be breefly described. The Betz's theory will be first presented, the effect of the wake rotation will be then added and finally the blade element momentum (BEM) theory will be discussed. The discussion will consider only the horizontal axis configuration, that is the one that characterizes the type of machine of interest for this thesis work. Some other useful concepts about these arguments can be found in [16] [17] [18].

2.2.1 1D Momentum theory: the Betz limit

In 1926 Betz developed a model able to determine the power from an ideal turbine rotor, the thrust on it and the effect of the rotor operation on the local wind field. The model is based on the one-dimensional momentum theory and considers the control volume reported in the figure below.

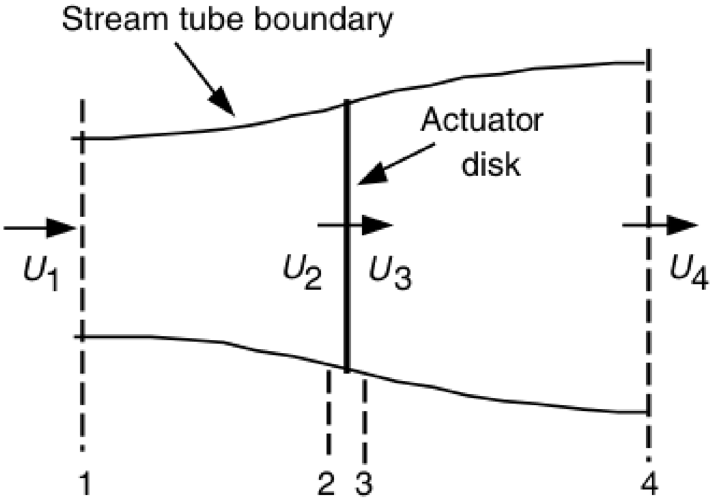

Figure 2.6. The control volume considered by Betz for his analysis

The boundaries of the control volume are represented by the surface of a stream tube and by two cross-sections (section 1 and 4). The turbine is modeled as an actuator disk (not rotating) that generates a pressure loss between the section 2 and 3. Some assumptions are at the basis of this model:

- the flow is homogeneus, incompressible and steady state;
- there is no frictional drag (ideal disk);
- the thrust is uniform all over the disk;
- the generated wake is not rotating;
- the static pressure far upstream and far downstream of the rotor is equal to the undisturbed ambient static pressure.

By applying the conservation of linear momentum to the control volume and considering the assumptions just introduced, it is possible to obtain an expression for the thrust:

$$T = \dot{m}(U_1 - U_2) \tag{2.3}$$

Moreover considering the Bernoulli principle between section 1 and 2 and between section 3 and 4:

$$p_1 + \frac{1}{2}\rho U_1^2 = p_2 + \frac{1}{2}\rho U_2^2 \tag{2.4}$$

$$p_3 + \frac{1}{2}\rho U_3^2 = p_4 + \frac{1}{2}\rho U_4^2 \tag{2.5}$$

and the fact that the thrust can also be expressed as:

$$T = A_2(p_2 - p_3) \tag{2.6}$$

it is possible to obtain:

$$T = \frac{1}{2}\rho A_2(U_1^2 - U_4^2) \tag{2.7}$$

By equating equation 2.3 and 2.7, the Froude condition is obtained:

$$U_2 = \frac{U_1 + U_4}{2} \tag{2.8}$$

Where U_1 is the velocity far upstream, U_4 is the velocity far downstream and U_2 is the velocity at the disk (the velocity across the disk remains the same: $U_2 = U_3$).
At this point an axial induction factor can be defined as:

$$a = \frac{U_1 - U_2}{U_1} \tag{2.9}$$

It represents the decrease in velocity between the free stream and the rotor plane.
Thanks to its definition it is also possible to write:

$$U_2 = U_1(1 - a) \tag{2.10}$$

$$U_4 = U_1(1 - 2a) \tag{2.11}$$

and to obtain an expression for the power output:

$$P = \frac{1}{2}\rho A U^3 4a(1 - a)^2 \tag{2.12}$$

where A is the rotor area and U the free stream velocity.
From the power, the power coefficient can also be derived by simply considering the ratio between the actual rotor power and the ideal power of the flow:

$$C_P = \frac{P}{\frac{1}{2}\rho U^3 A} = 4a(1 - a)^2 \tag{2.13}$$

Its maximum value can be computed for an axial induction factor of $\frac{1}{3}$ and is equal to $\frac{16}{27}$. This value is known as Betz limit and represents the maximum power coefficient that can be theoretically reached in ideal conditions.
The same reasoning can be done also for the thrust and for the associated thrust coefficient. Their expressions are:

$$T = \frac{1}{2}\rho A U^2 4a(1 - a) \tag{2.14}$$

$$C_T = 4a(1 - a) \tag{2.15}$$

The maximum value for C_T is equal to 1 and corresponds to a value of the axial induction factor of 0.5 (that means a downstream velocity equal to zero). After this value the Betz theory is no more valid and some corrections need to be introduced. Negative values for the downstream velocity in fact would be obtained.
In the figure below a graph showing the trend of C_P and C_T as a function of the axial induction factor is reported. Moreover the values for which the model is no more valid are evidenced.

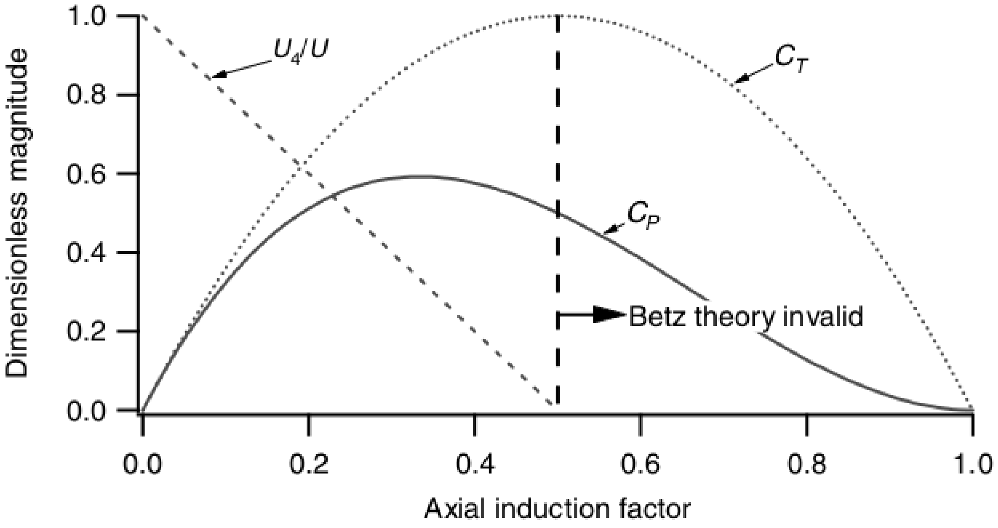

Figure 2.7. C_P and C_T evolution function of the axial induction factor

2.2.2 Effects of rotation: Glauert's results

In the previous section it was assumed that no rotation was imparted to the flow. However, in reality a wind turbine is characterized by a rotor that generates a wake rotating in the opposite direction. This happens in reaction to the torque exerted by the flow to the rotor. The higher is the torque, the higher is the rotational kinetic energy in the wake and this results in less energy extraction with respect to the case without wake rotation. This problem was first modelled by Glauert in 1935. In the figure below a simple sketch representing the phenomenon is reported. An annular stream tube characterized by a radius r and a thickness dr is considered for the analysis.

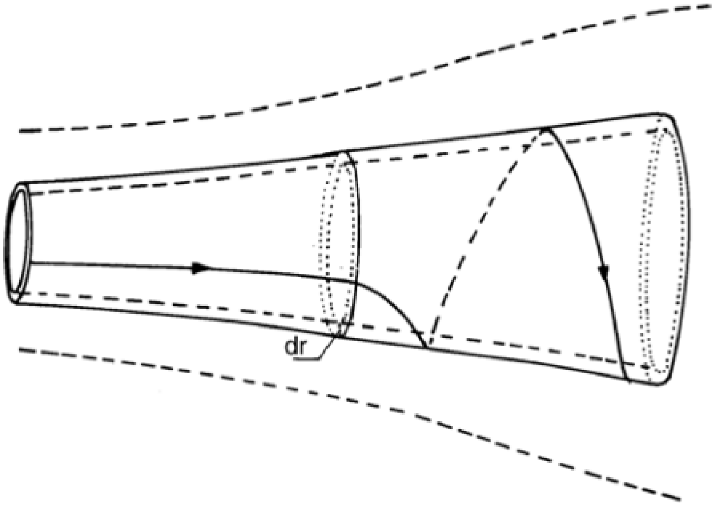

Figure 2.8. Sketch of an annular stream tube with wake rotation

A new expression for the thrust acting on an annular element that takes into account the wake rotation can be derived:

$$dT = [\rho(\Omega + \frac{1}{2}\omega)\omega r^2]2\pi r dr \tag{2.16}$$

where Ω is the angular velocity of the rotor and ω is the angular velocity of the wake. A parameter useful to model the wake rotation can be introduced. It is called tangential induction factor (a') and is defined as:

$$a' = \frac{\omega}{2\Omega} \tag{2.17}$$

So the expression for the thrust can be rewritten as:

$$dT = 4a'(1 + a')\frac{1}{2}\rho\Omega^2 r^2 2\pi r dr \tag{2.18}$$

At this point the formulation for the annular thrust obtained from the Betz theory can be considered again:

$$dT = 4a(1 - a)\frac{1}{2}\rho U^2 r^2 2\pi r dr \tag{2.19}$$

where U is the free stream velocity.
Equating the two expressions, a relation between the two induction factors is derived:

$$\frac{a(1 - a)}{a'(1 + a)} = \frac{\Omega^2 r^2}{U^2} = X^2 \tag{2.20}$$

The term at the end of the formula is the so called *local speed ratio* and is computed as the ratio between the velocity of the blade at a certain radial position and the free stream velocity.
Another similar coefficient can be derived: the *tip speed ratio* (λ). It is computed as:

$$\lambda = \frac{\Omega R}{U} \tag{2.21}$$

Where R is the radius of the blade in correspondence of the tip.
Obviously these two coefficients are linked by the following relation:

$$X = \frac{\lambda r}{R} \tag{2.22}$$

Considering now the conservation of angular momentum, also a formulation for the annular torque can be obtained:

$$dQ = 4a'(1 - a)\frac{1}{2}\rho U\omega r^2 2\pi r dr \tag{2.23}$$

Multiplying it by the rotor angular velocity, the annular power is found:

$$dP = \frac{1}{2}\rho A U^3[\frac{8}{\lambda^2}a'(1 - a)X^3 dX] \tag{2.24}$$

and the power coefficient integrated all over the rotor can be derived too:

$$C_P = \frac{8}{\lambda^2} \int_0^{\lambda} a'(1-a)X^3 dX \tag{2.25}$$

In order to maximize the power output (as already done in the previous section), an optimal relation between the two induction factors is found:

$$a' = \frac{1-3a}{4a-1} \tag{2.26}$$

Considering now the equation 2.20, the optimal distribution for both the induction factors along the radius can be computed. This allows to reach the maximum power for each annular section and so for the entire rotor.

In table 2.1 the optimal distribution of a and a' functions of X is reported, whereas in Figure 2.9 a comparison between the optimal power coefficient derived by Betz and the one that takes into account the wake rotation is shown.

a	a’	X
0.260	5.50	0.07
0.265	3.42	0.11
0.270	2.38	0.16
0.275	1.75	0.20
0.280	1.33	0.25
0.285	1.04	0.31
0.290	0.81	0.37
0.295	0.64	0.45
0.300	0.50	0.53
0.305	0.39	0.63
0.310	0.29	0.75
0.315	0.21	0.92
0.320	0.14	1.15
0.325	0.08	1.56
0.330	0.03	2.62
0.331	0.03	2.86
0.332	0.02	3.59
0.333	0.01	5.39

Table 2.1. Relation among the axial induction factor, the tangential induction factor and the local speed ratio

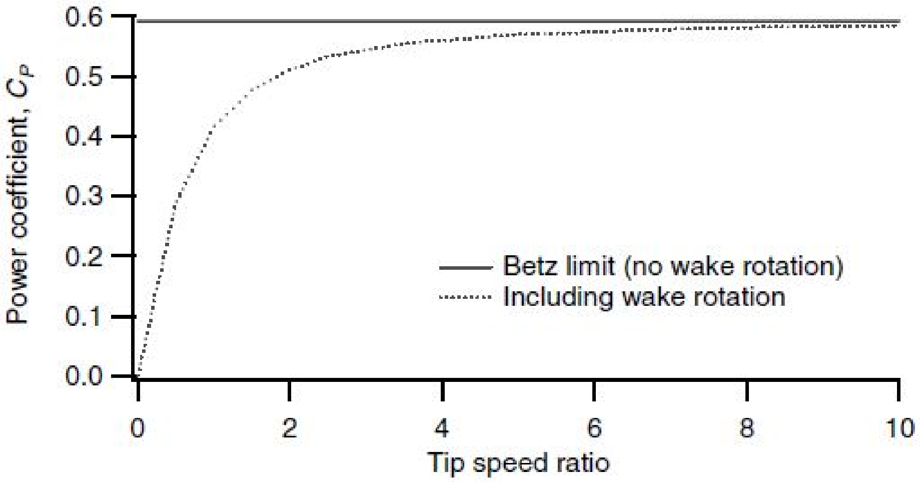

Figure 2.9. Trend of the C_P function of the tip speed ratio considering the wake rotation

As it is possible to note, the limit set by Betz of $C_P, max=\frac{16}{27}$ cannot be exceeded. However the more the *tip speed ratio* increases, the closer the curve is to the ideal value and the effect of wake rotation affects less the power extraction process.
Finally, if one wants to understand the effect of the two induction factors on the flow near the blades, the figure below shows what happens to the incoming velocity in correspondence of a section of a blade of the wind turbine.

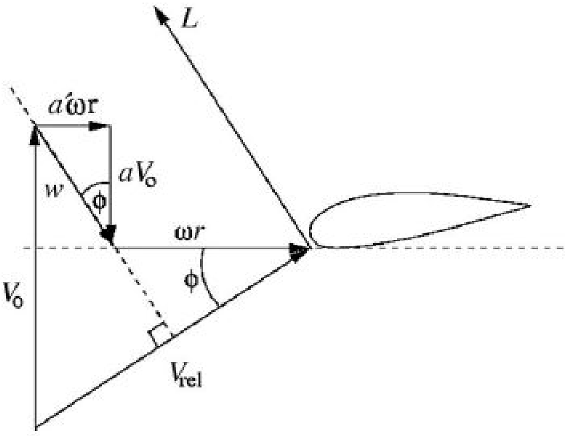

Figure 2.10. Effect of the induction factors on the incoming flow field

The absolute free stream velocity (the one previously named U) is affected by the axial induction factor (a), whereas the peripheral velocity (that represents the tangential velocity of the blade) is affected by the tangential induction factor (a'). The sum of these two modified velocities results in the relative velocity (V_{rel}): the real incoming velocity seen by the blade in its rotating frame of reference.

2.2.3 BEM method

The BEM (Blade Element Momentum) method is one of the most popular methods used in order to model the operation of wind turbines and many of the most recent methods are based on it. It can be seen as a further step of the Glauert's previous work. Its objective in fact is not only to take into account all the flow structures that develop behind a wind turbine rotor, but it also wants to consider the presence of the actual blades and to introduce the aerodynamic forces in the discussion. Moreover it wants to consider the presence of the drag too. In order to achieve these objectives the method couples the results obtained with the momentum theory and the ones that take into account what happens locally to the blades, when the turbine is subjected to an incoming wind flow. Once again the rotor needs to be divided in a certain number of annular sections. The expressions for the annular thrust and the annular torque based on the momentum theory were already derived in the two previous sections, whereas their expressions based on the local interaction of the blades with the incoming flow can be found looking at the following figure.

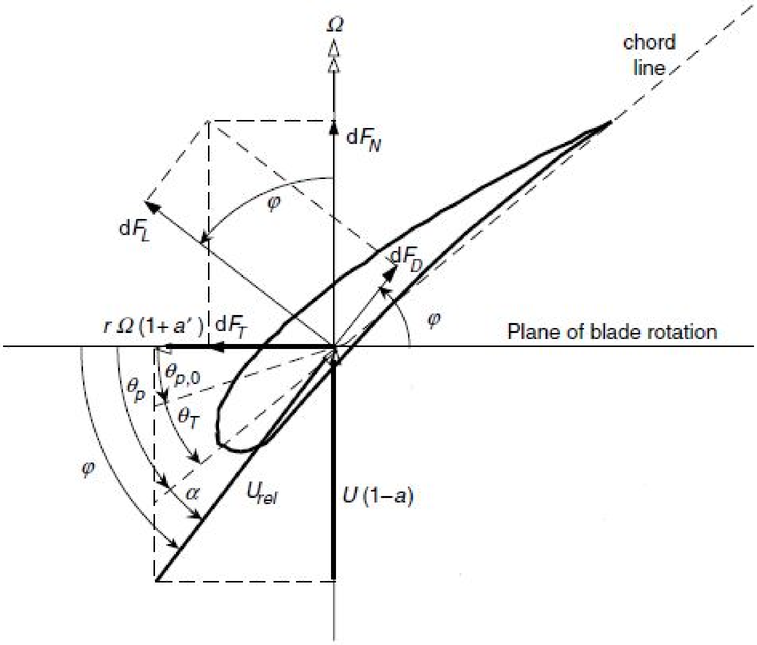

Figure 2.11. A representation of the angles characterizing a generic profile, of the incoming flow field and of the forces exchanged

φ is the angle between the relative incoming velocity and the plane of blade rotation and it is found as the sum of the section pitch angle θ_p (sum of the blade pitch angle $\theta_{p,0}$ and the section twist angle θ_T) and the angle of attack α. The latter, as already mentioned in section 2.1, is the angle that allows to find the value of the C_L and C_D for the specific section. Thanks to them also the value of the lift and of the drag can be obtained. In the figure the normal and the tangential forces are represented too. They are derived by simply projecting the total force acting on the section on a direction parallel to the plane of blade rotation and on a direction perpendicular to it. Therefore, the following expressions can be derived:

$$\tan(\varphi) = \frac{U(1-a)}{\Omega r(1+a')} \tag{2.27}$$

$$U_{rel} = \frac{U(1-a)}{\sin(\varphi)} \tag{2.28}$$

$$U_{rel} = \frac{\Omega r(1+a')}{\cos(\varphi)} \tag{2.29}$$

$$dF_L = C_L \frac{1}{2} \rho U_{rel}^2 c dr \tag{2.30}$$

$$dF_D = C_D \frac{1}{2} \rho U_{rel}^2 c dr \tag{2.31}$$

$$dF_N = dF_L \cos(\varphi) + dF_D \sin(\varphi) \tag{2.32}$$

$$dF_T = dF_L \sin(\varphi) - dF_D \cos(\varphi) \tag{2.33}$$

$$C_N = \frac{dF_N}{\frac{1}{2}\rho U_{rel}^2 c dr} \tag{2.34}$$

$$C_T = \frac{dF_T}{\frac{1}{2}\rho U_{rel}^2 c dr} \tag{2.35}$$

At this point, in order to consider the presence of the real blades, the number of them must be introduced. It is represented by the parameter B. In this way the total normal force (the thrust) on the section at a distance r from the center can be computed as:

$$dT = B \frac{1}{2} \rho U_{rel}^2 (C_L \sin(\varphi) - C_D \cos(\varphi)) c dr \tag{2.36}$$

Or (considering the relation between the relative velocity and the axial induction factor) as:

$$dT = B \frac{1}{2} \rho \frac{U^2 (1-a)^2}{\sin(\varphi)^2} C_N c dr \tag{2.37}$$

The parameter B can also be used to derive the expression of the torque generated by the tangential force acting at a distance r from the center:

$$dQ = B r dF_T = B \frac{1}{2} \rho U_{rel}^2 (C_L \sin(\varphi) - C_D \cos(\varphi)) c r dr \tag{2.38}$$

or:

$$dQ = B \frac{1}{2} \rho \frac{U(1-a)\Omega r(1+a)}{\sin(\varphi)\cos(\varphi)} c C_T r dr \tag{2.39}$$

At this point these final expressions for the annular thrust and the annular torque can be equated with the ones previously obtained (equations 2.19 and 2.23). Two new equations for the two induction factors, able to couple the momentum theory with the local flow effects, are found:

$$a = \frac{1}{\frac{4\sin(\varphi)^2}{\sigma C_N} + 1} \tag{2.40}$$

$$a' = \frac{1}{\frac{4\sin(\varphi)\cos(\varphi)}{\sigma C_T} - 1} \tag{2.41}$$

The parameter σ, called solidity, inside the two formulas is another coefficient able to take into account the effect of having a finite number of blades. It can be computed as:

$$\sigma(r) = \frac{c(r)B}{2\pi r} \tag{2.42}$$

In order to achieve a complete coupling between the results of the aerodynamics of the blades and the momentum theory, convergence has to be reached. The BEM method is in fact an iterative method.
Here below the steps of the iterative procedure for each annular control volume (considered independent of the others) are reported:

1. initialize a and a', typically $a = a' = 0$;
2. compute the flow angle φ;
3. compute the local angle of attack;
4. evaluate $C_L(\alpha)$ and $C_D(\alpha)$ from tabulated data;
5. compute C_N and C_T;
6. calculate a and a';
7. reiterate from step 2 up to reaching convergence;
8. compute the loads on the segment of the blades.

After the application of the method to all the annular control volumes, the distribution of the loads all over the rotor is known: the global quantities that characterize the machine can be computed.

Chapter 3

Computational Fluid Dynamics

In this chapter some features related to Computational Fluid Dynamics (CFD) will be described, its importance will be evidenced and the open-source software OpenFOAM based on it will be introduced. A description of the main methods based (or partially based) on CFD will be also present. Finally SOWFA, the tool chosen for this thesis work, will be presented. For more information about CFD arguments the reader can refer to [19], [20], [21], [22].

3.1 Role and Importance of CFD

Computational Fluid Dynamics (CFD) is the analysis of systems involving fluid flow, heat transfer and associated phenomena, such as chemical reactions, by means of computer-based simulations. It can be applied in so many different fields. It allows to study the aerodynamics of aircrafts and vehicles, the operation of power plants, the flows acting on turbomachines, weather predictions, the flows considered in the biomedical engineering field, the wind acting on civil structures, etc.
CFD was first introduced in the aerospace industry during the 1960s and then it spread to several other fields. The main obstacles to the diffusion of this tool were the complexity at its basis and the need of quite huge computational resources. Since the 1990s, thanks to the continuously increasing computational power and the introduction of some user-friendly interfaces, CFD started to grow in the industrial context and nowadays is becoming a fundamental tool in the design of industrial products and processes, with the aim of being comparable with the other Computer-aided engineering (CAE) tools. Its introduction in fact allows to reach many important advantages such as the reduction of lead times and costs for new designs, the opportunity to study systems that are impossible to be experimentally tested or to perform simulations in extreme conditions and the possibility to have a very high level of detail in the results. Moreover CFD is able to perform an extremely large number of simulations with almost zero added expenses. More and more skilled operators are required in order to use this extremely useful tool in a conscious way and to allow the continuous enhancement of it as a fundamental means for both the field of research and the industrial progress.

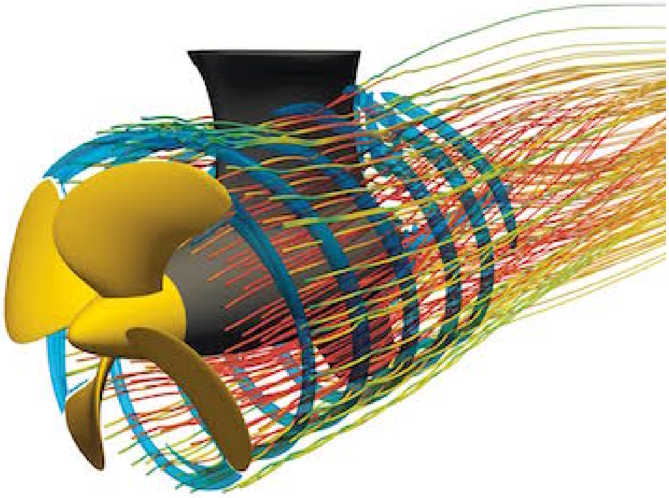

Figure 3.1. A CFD application for the simulation of a propeller

3.2 The three phases of a CFD study

The process that characterizes a CFD study can be divided in three main phases, that are common to all commercial CFD packages. They are:

- the pre-processing phase;
- the solving phase;
- the post-processing phase.

This section will be dedicated to a brief description of them, evidencing their main characteristics.

3.2.1 Pre-processing phase

This first phase is the one related to the insertion of the inputs of the problem by the CFD user. These will be then remanaged in order to be used by the solver.
During this phase, the actions concerning the user are:

- the definition of the geometry of the domain that need to be studied;
- the generation of a grid suitable for the domain defined (mesh generation process);
- the selection of the physical and chemical phenomena that need to be modelled;
- the definition of fluid and flow properties;
- the definition of appropriate boundary conditions for the cells in correspondence of the boundaries of the domain;
- the choice of numerical methods and turbulence models that will be used in the second phase.

For sure, the most important action for a user among the ones just listed is the mesh generation. A mesh can be structured or unstructured (or even a combination of the two) and can be characterized by some zones more refined than the others, in order to capture in a proper way the phenomena of interest. Usually the accuracy grows with the level of refinement that characterizes the mesh. However, the computational cost needed in order to perform a simulation with a very refined mesh increases a lot. A trade-off between the reachable accuracy and the computational cost required has to be always taken into account and the user must take this decision in a very careful and conscious way.

3.2.2 Solving phase

During this phase, the solution (velocity, pressure, temperature, etc.) has to be defined at nodes inside each cell. In the finite volume method (probably the most widespread method in the CFD field and also the one used for this thesis work) the cells are represented by small control volumes, whose properties are referred to their centroid. Conservation laws can be applied on them. For doing this the Navier-Stokes equations are considered:

$$\frac{\partial \rho}{\partial t} + \vec{\nabla} \cdot (\rho \vec{U}) = 0 \tag{3.1}$$

$$\frac{\partial (\rho \vec{U})}{\partial t} + \vec{\nabla} \cdot (\rho \vec{U} \vec{U} + p \bar{\bar{\mathbf{I}}} - \bar{\bar{\tau}}) = \rho \vec{f_e} \tag{3.2}$$

$$\frac{\partial \rho E}{\partial t} + \vec{\nabla} \cdot (\rho H \vec{U} - k \vec{\nabla} T - \bar{\bar{\tau}} \cdot \vec{U}) = \rho \vec{f_e} \cdot \vec{U} + q_H \tag{3.3}$$

They represent the mass balance (continuity) equation, the three momentum balance equations and the energy balance equation.
In order to be applied on every cell composing the domain, the Navier-Stokes equations are discretized thanks to the numerical methods defined in the pre-processing phase. This allows to obtain a system of algebraic equations describing the conditions of the simulated domain. The resulting system needs then to be solved in an iterative way, in order to reach the final solution by convergence.
Depending on the nature of the problem studied, different solvers exist. For a steady state case a typical choice is represented by the SIMPLE (Semi-Implicit Algorithm for Pressure-Linked Equations) solver. The algorithm gives a method that is able to calculate sequentially the pressure and the velocity, coupling them. The procedure is iterative and the solution is obtained by reaching convergence. For a transient phenomenon instead a suitable choice for the resolution algorithm is the Pressure-Implicit with Splitting of Operators (PISO) solver. Once again, it couples the pressure and the velocity and can be seen as an extension of the SIMPLE algorithm. The idea at the basis of this solver is that the linear pressure-velocity coupling is much stronger than the non linear convection term (that contains the velocity-velocity coupling). This is also the algorithm that was considered for the CFD simulations performed for this thesis work. For a deeper discussion about the available solvers the reader can refere to [20].

3.2.3 Post-processing phase

The post-processing phase is the third and last phase. It is of fundamental importance because during it the results of the simulation need to be collected, understood and used in order to reach a good comprehension of what happened inside the domain. Moreover during this phase the quality and the reliability of the results must be evaluated: it is necessary to understand if the obtained results are accurate enough. Finally the results can be compared with some experimental data or with some outputs from different methods.

In order to facilitate the post-processing phase, most of the CFD packages are now equipped with versatile data visualization tools, such as domain geometry and grid display, vectors plots, particle tracking, view manipulation, etc.

3.3 Introduction to turbulence and its implication on CFD modelling

Most of the flows studied by CFD are affected by turbulence. Turbulence is a phenomenon characterized by the presence of eddies of different sizes that cause chaotic fluctuations of flow quantities even with time-invariant boundary conditions. From a mathematical point of view these unstable structures that characterize a turbulent flow can be seen as non-linear terms inside the Navier-Stokes equatons, that need to be modeled.

The process that brings to the generation of turbulence (from the largest turbulent scales, to the smallest turbulent scales) is based on the energy cascade theory. According to this, the larger eddies are unstable, break up and transfer their energy to smaller eddies. When the dimension of the eddies is such that the Reynolds number is so small that the eddy is no more unstable, its energy is dissipated into thermal energy by friction. In this case the so called “Kolmogorov scale” has been reached.

In Figure 3.2 a chart linking the energy of the turbulent structures with their turbulent scale is shown.

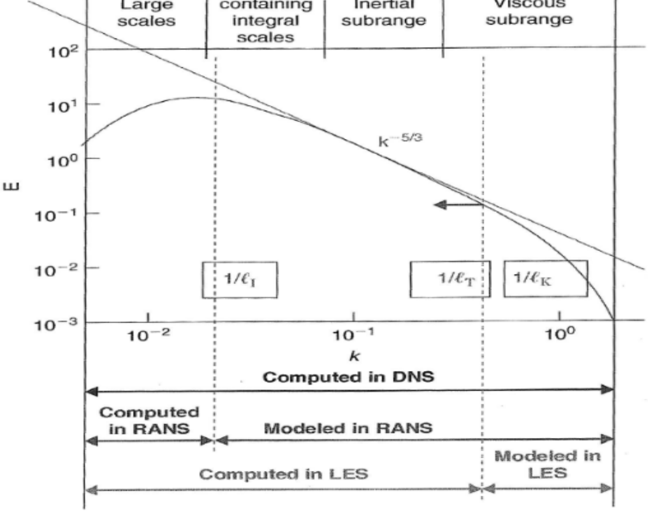

Figure 3.2. Energy cascade

The huge variety of turbulent structures dimensions has a big implication also in a CFD study. Usually in fact three different types of simulation, depending on the range of turbulent scales that is simulated, can be performed. They are:

1. Direct Numerical Simulations (DNS): They directly simulates all the scales of turbulence, from the largest to the smallest. The size of the smallest turbulent eddies is inversely proportional to $Re^{\frac{3}{4}}$. The spatial grid for this type of simulations needs to be sufficiently fine to resolve the Kolmogorov length scale and the time step considered has to be able to capture the period of the fastest fluctuations. These simulations have an extremely high computational cost and for this reason they are not suitable for industrial flow computations.

2. Large Eddy Simulations (LES): This second type of simulations has the objective of modeling the small turbulent scales, but simulating all the others. For this reason a subgrid scale is introduced: above it the turbulent fluctuations are simulated, below it the turbulence is modeled by semi-empirical laws. The effect of the unresolved eddies is included by means of a so called sub-grid scale model. The interaction between large and filtered vortexes gives rise to Subgrid-scale (SGS) stresses.
   Due to the fact that unsteady flow equations must be solved, the computational cost required is once again quite high. The total computational effort is in fact proportional to $Re^{\frac{9}{4}}$.
   Large eddy simulations are the ones used for this thesis work. The reason is that (as will be explained later) the real simulated machine is not present inside the computational domain and so all the very small turbulent structures near the physical blades (that characterize the boundary layer) do not need to be simulated.

3. Reynolds Averaged Navier Stokes (RANS) equations: They consider the mean flow and the effects that turbulence has on its properties. The Navier-Stokes equations are time averaged or ensemble averaged. This averaging process causes the appearance of some extra terms that need to be treated with some specific models. This third type of simulations has the lowest computational cost. For this reason RANS have begun to be largely applied in the industrial context.

3.4 OpenFOAM

OpenFOAM is an open source, freely available CFD toolbox, written in a highly efficient C++ object-oriented programming. It was born in the 1990s at The Imperial College of London, which has been a center of CFD research since the 1960s. The principal developers were Henry Weller and Dr. Hrvoje Jasak, under the supervision of Prof. David Gosman. Their objective was to create an object-oriented platform where it was possible to efficiently implement and test numerical and physical models. During the following years the number of users and developers increased more and more and now it is widely diffused both in the research and industrial field. OpenFOAM in fact constitutes a very powerful toolbox for customized numerical solvers that can perform simulations of basic CFD, combustion, turbulence modeling, electromagnetics, heat transfer, multiphase flow, stress analysis and even financial mathematics. In the figure below a scheme showing the structure of the code is reported.

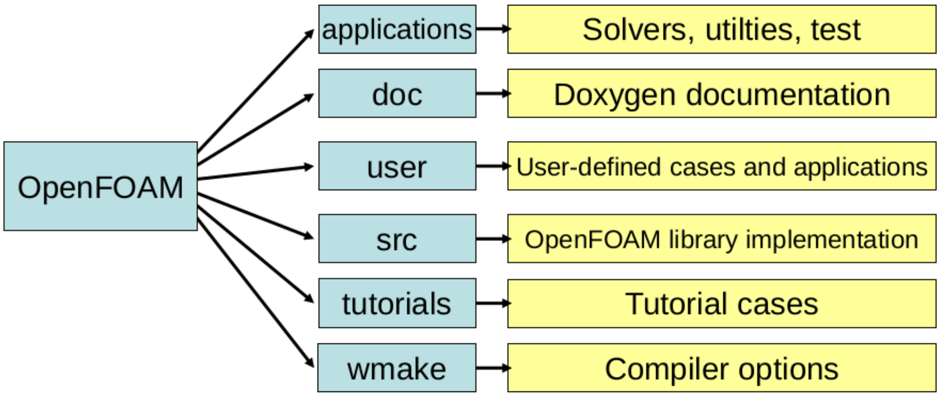

Figure 3.3. OpenFOAM structure

The representation of the complex physical models at the basis of Continuum Mechanics is achieved in OpenFOAM by mimicking the form of partial differential equations that characterize them. As an example it is possible to consider the turbulence kinetic energy equation in Reynolds Averaged Navier-Stokes models:

$$\frac{\partial k}{\partial t} + \nabla \cdot (\vec{u}k) - \nabla \cdot [(\nu + \nu_t)\nabla k] = \nu_t[\frac{1}{2}(\nabla\vec{u} + \nabla\vec{u}^T)]^2 - \frac{\epsilon_0}{k_0}k \tag{3.4}$$

that in OpenFOAM is translated in the following way:

```
solve
(
    fvm::ddt(k)
  + fvm::div(phi, k)
  - fvm::laplacian(nu() + nut, k)
 == nut*magSqr(symm(fvc::grad(U)))
  - fvm::Sp(epsilon/k, k)
);
```

The correspondence between the two formulations is clearly visible: each term of the partial differential equation is translated and the complex physics behind it can be well reconstructed.
Finally, in order to facilitate the post-processing phase and to make the simulations results more comprehensible, OpenFOAM can be coupled with ParaView: a data-visualization tool based on both qualitative and quantitative techniques.
The simulations performed for this thesis work have been made possible thanks to the version 2.4.0 of OpenFOAM.
Other useful information related to OpenFOAM can be found in [23] and [24].

3.5 Resolution methods based on CFD

In this chapter the main and most diffused methods based on CFD will be introduced and discussed. The attention will be focused only on those methods that are applied in the wind energy field. The reason is that this thesis work is a study related to the performances of wind turbines and so in this context only the methods that can be applied to them are of interest. Moreover one of the methods that will be described is the one chosen for the modeling of the simulated turbines operation.
The methods that will be considered are:

- the Fully Resolved (FR) method;
- the Actuator Disk (AD) method;
- the Actuator Line (AL) method.

3.5.1 Fully resolved (FR) method

The Fully Resolved method is based on the presence of the exact layout of the simulated wid turbine inside the computational domain. The geometry characterizing the real machine is in fact reconstructed in a very precise way. This is done in order to reproduce as accurately as possible the interaction of the wind turbine with the incoming wind flow.
The accuracy of this method can reach an incredibly high level. However, this also causes a very high increase in the required computational cost. This is due to the fact that a fine resolution near the blades is needed, that brings to a larger number of cells inside the domain. All the small flow structures characterizing the region near the blades (such as the boundary layer) must be properly represented. For doing this a lot of attention is required in the mesh generation process. A regular structured mesh around the blade is required in order to avoid spurious effects, that could lead to a wrong estimation of the machine performances. The smallest cell dimension needed depends on the turbulence model chosen.
Despite the extreme accuracy of this method, the very huge computational burden required makes the choice of it often unfeasible (especially when entire wind farms are simulated). Other less expensive methods are needed.

3.5.2 Actuator Disk (AD) method

The Actuator disk method represents the first attempt to couple the high accuracy of the CFD simulations in representing the flow with the very limited computational cost of the BEM method. CFD allows to obtain the incoming velocity by simply sampling it directly in correspondence of the position of the machine inside the simulated computational domain. In this way it is possible to take into account the real conditions of the incoming flow, so avoiding the main limitation of the BEM method. The difference with the fully resolved method is represented by the fact that the real machine is not considered inside the domain. Its presence is mimicked by an actuator disk (that corresponds to the area swept by the real turbine rotor), composed by many actuator points. In the figure below a possible representation of the actuator disk is shown.

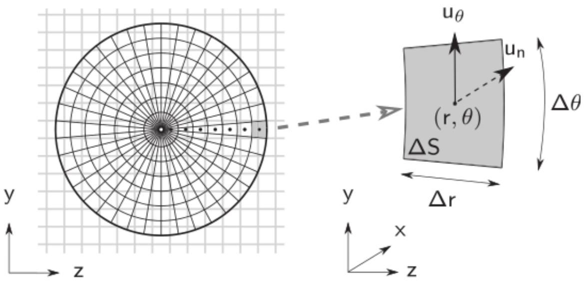

Figure 3.4. Actuator Disk method

The aim of the method is to represent the effect that the wind turbine rotor has on the incoming flow. This is done by applying in correspondence of each actuator point a force. Such force can be computed following the same procedure used for the BEM method. As already mentioned, the velocity (u) is in fact sampled in the computational domain for each actuator point and the relative velocity can be computed as:

$$U_{rel} = \vec{u} - \Omega r \hat{t} = u_n \hat{n} + (u_t - \Omega r)\hat{t} \tag{3.5}$$

where U_{rel} is the relative velocity, that takes into account also the rotation, u is the absolute sampled velocity and Ω is the rotational velocity. From the relative velocity vector also the angle of attack at the radial position considered is known, as already explained in the section related to the BEM method (2.2.3) . At this point, thanks to the computed angle of attack, the coefficients (C_L and C_D) needed for obtaining the forces are found thanks to some tabulated data. Finally the lift and drag forces are calculated from their common formulas and are summed up in order to find the total force acting on the considered actuator point:

$$\vec{F} = \vec{L} + \vec{D} \tag{3.6}$$

or, if there is the need to express it as a force per unit volume:

$$\vec{f} = \frac{\vec{L} + \vec{D}}{V_{cell}} \tag{3.7}$$

where $\vec{D}$ is the drag force, $\vec{L}$ is the lift force and V_{cell} is the volume of the cell the actuator point refers to.

This force needs then to be spread thanks to a Gaussian projection function, in order to avoid numerical issues. The role and the importance of the spreading function will be discussed more in detail in the next sections.

From a mathematical point of view the application of a force on an actuator point is seen as the insertion of a body force inside the Navier-Stokes incompressible equations:

$$\frac{\partial \vec{u}}{\partial t} + (\vec{u} \cdot \nabla)\vec{u} + \frac{1}{\rho}\vec{f} = -\frac{1}{\rho}\nabla p + \mu \nabla^2 \vec{u} \tag{3.8}$$

$$\nabla \cdot \vec{u} = 0 \tag{3.9}$$

The term $\vec{f}$ is in fact equal to the force per unit volume just computed. This causes a modification of the flow and the solution (that takes into account the presence of the turbine) can be achieved.

3.5.3 Actuator Line (AL) method

The actuator line method can be seen as an updated version of the actuator disk method. As already described in the previous section, in fact, the actuator disk method tries to reconstruct the area swept by the wind turbine rotor. In the actuator line method, instead, the aim is to reach a better representation of the machine. A number of lines equal to the number of blades is chosen. They are the so called actuator lines. Along each actuator line a certain number of actuator points is present. In correspondence of each of them a force is applied and the incoming flow feels its presence. The procedure needed for the identification and the application of the forces on the actuator points is the same followed for the actuator disk method and derives from the formulations for the aerodynamic loads at the basis of the BEM method too. In the figure below a simple scheme representing the way in which the method works is reported. It is possible to observe the discretization of the wind turbine in a certain number of actuator points, the sampled incoming velocity in correspondence of each point and the derived aerodynamic forces.

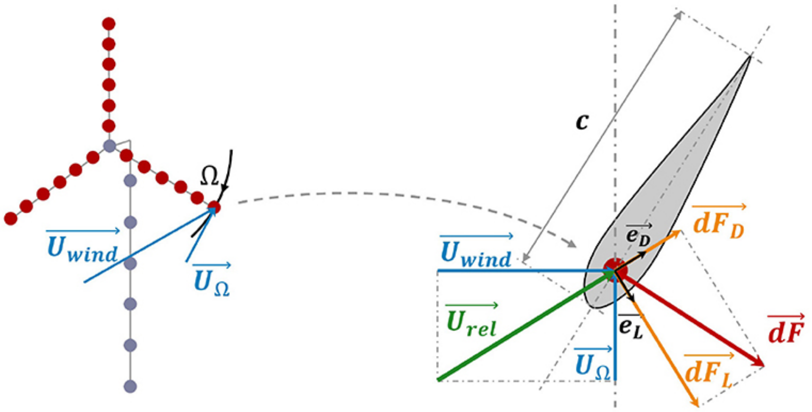

Figure 3.5. Actuator Line method

The big improvement generated by the presence of the actuator lines instead of the actuator disk is the fact that the operation of the machine can be simulated more properly. The turbulent structures characterizing the actual machine can in fact be represented in a much more realistic way. Tip vortices, root vortices and generic vorticities shed along the blades can be clearly observed, together with their effect on the downstream wake and on the performances of the machine.

With the aim of mimicking the real behaviour of the wind turbines in a way as precise as possible, this method was the one chosen for this thesis work. For this reason some words about some specific aspects of the method need to be spent. They are the velocity sampling and the projection of the forces in the computational domain.

Velocity Sampling

The velocity that needs to be sampled in order to be then used for computing the aerodynamic forces is the freestream one. This means that the velocity sampling should be done in a way such that the blade-local effects (upwash and downwash phenomena induced by the blade-circulation) are not seen, but the gross deceleration of the flow due to the rotor axial induction is taken into account.

Different methods exist. Some of them are based on sampling the velocity at a certain distance from the actuator line. The Effective Velocity Model (EVM) belongs to this category. The method was developed by Paolo Schito in his PhD Thesis [9] and further explored in successive works (such as [11] and [10]). Other attempts in considering a certain distance upstream of the actuator line for sampling the velocity were made for example by Mittal *et al* in [25]. However, the problem of this typology of sampling methods is the fact that the distance is a tunable parameter and often there is no general consensus about the sampling location. For this reason, with the aim of avoiding the ambiguity of the tunable distance, other methods were devised. For example, Shengbai Xie in [26] proposed a new approach in which a lagrangian averaging process is introduced in order to obtain the incoming velocity vector. Matthew J. Churchfield *et al*, instead, worked at a modified version of the actuator line method (called Advanced Actuator Line Method) and introduced a method for the computation of the incoming velocity that considers the integral of the velocity field weighted by the force projection function [1].

For this thesis work the local velocity sampling was chosen: the velocity is sampled in correspondence of each actuator point and this value is used for the computation of the forces. The reason at the basis of this choice is that, considering an isotropic Gaussian force projection function (as the one used in this work), the influence of the blade-local effects in correspondence of the actuator point can be negligible [2]. This happens because the actuator point is also the center of the bound vortex generated by the application of the force, that leads to the up-wash (upstream) and down-wash (downstream) phenomena. So, theoretically, by sampling the incoming velocity exactly on the actuator point, the free-stream velocity can be obtained. The criticality of this method is that in the region around the actuator line the gradient in the angle of attack of the velocity vector is very steep (for the presence of the bound-vortex). Just a small error in the interpolation of the velocity from the nearest cells, could lead to relevant error in the estimation of the angle of attack and of the forces. For this reason, the finer is the mesh, the better this method works and the closer the sampled velocity is to the free-stream one.

Forces projection

In the actuator line method, when the forces are computed from the sampled incoming velocity, they are not simply applied to the actuator points. Thanks to a Gaussian force projection function they are in fact projected into a body force field that affects the cells around the actuator lines. So the force is not concentrated in a single point but is smeared on a certain number of cells, depending on the parameters of the Gaussian function chosen. This is done mainly for two reasons. The first one is a mathematical reason: the smooth distribution of the force from the single actuator

point onto the neighbouring cells avoids the generation of spurious oscillations in the actuator line vicinity. The second reason, supported for example by Matthew Churchfield *et al* in [1], instead derives from the fact that in reality the force exchanged by the blade is spread out over the entire surface. Therefore, in order to mimic this physical reality, the force has to be spread out in the computational domain too.
Different types of Gaussian force projection functions exist. Shives and Crawford [27] for example tried to consider a three-dimensional Gaussian function that is isotropically wide, but that varies in width along the blade radius as a linear function of the chord. Churchfield *et al* [1] instead devised a method with the aim of trying to make the projection function looks more like the force distribution of an airfoil: they considered three different projection function widths along the chord-wise direction, the thickness-wise direction and the radial directions.
For this thesis work an isotropic Gaussian projection function (the same used by Sørensen ans Shen in [7]) was considered. As already said, the reason of this choice lies on the fact that with this type of projection function the velocity in correspondence of the actuator point should be the free-stream one.
The function is given by:

$$g_{AL}(x,y,z) = \frac{1}{\epsilon^2 \pi^{\frac{3}{2}}} exp(-\frac{(x-x_0)^2+(y-y_0)^2+(z-z_0)^2}{\epsilon^2}) \tag{3.10}$$

where ϵ is the Gaussian width, x, y and z are the three coordinate directions and x_0, y_0 and z_0 represent the location on which the function is applied (the actuator points).
The body force surrounding the actuator point is then simply given by:

$$\vec{f}(x,y,z) = g_{AL}(x,y,z)\vec{F} \tag{3.11}$$

where $\vec{F}$ is the force computed in correspondence of the actuator point thanks to the sampled incoming velocity. This operation is then performed for all the actuator points composing each blade. The result is a sort of cylindrical tube of force surrounding each actuator line. A visualization of it can be observed in the figure below, where the rotor of the NREL5MW wind turbine, composed by three actuator lines, is represented. The distribution of the forces around each line is clearly visible.

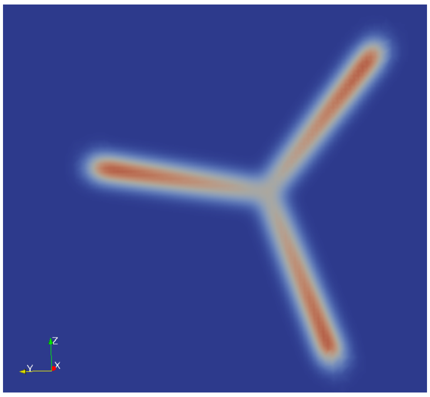

Figure 3.6. Projection in the surrounding area of the forces exchanged by the NREL5MW wind turbine

3.6 SOWFA (Simulator fOr Wind Farm Applications)

SOWFA is probably the most advanced and diffused tool for the simulation of wind turbines with the AL and AD methods. It was also the tool chosen for this thesis work and, more precisely, the actuator line approach was used. The aim of this section is to briefly describe its main characteristics and potentialities. For further information about it the reader can refere to [28] and [29].

3.6.1 Introduction to SOWFA

SOWFA (Simulator fOr Wind Farm Applications) is a set of CFD solvers, boundary conditions and turbine models, based on OpenFOAM. It was developed by NREL (National Renewable Energy Laboratory), a government-owned, contractor-operated facility, funded and overseen by the U.S. Department of Energy and specialized in the research and development of renewable energy, energy efficiency, energy systems integration and sustainable transportation. The objective of NREL was to develop a high-fidelty tool able to couple CFD with wind turbines operation, by considering Large Eddy Simulations (LES). In this way SOWFA allows to investigate a huge number of aspects characterizing a wind farm. For example it offers the possibility to reconstruct in a way as precise as possible the atmospheric conditions that characterize the real location in which the wind turbines are placed. This is done by performing precursor simulations on the Atmospheric Boundary Layer. Planes of data are saved from them and used as inflow boundary conditions for the domain containing the wind turbines, in order to mimic the real incoming conditions. The performances of the single wind turbine are then computed with an AL or AD approach. Finally, SOWFA can be also coupled with FAST, an NREL aero-elastic code able to compute the turbine structural and system response. High-fidelity simulations that take into account both the real characteristics of the incoming flow and the structural response of the turbine can therefore be performed.

3.6.2 Available Solvers

The solvers available in SOWFA are:

- **ABL solver**: it is an atmospheric solver, that can be run in PISO or SIMPLE mode, able to simulate a variety of atmospheric stabilities. Usually it is used in LES mode in order to compute turbulent atmospheric precursor wind fields.
- **ABLTerrainSolver**: it is basically the same solver of the previous one, but with the difference that the planar averaging performed in ABLSolver is replaced with a time averaging.
- **windPlantSolver**: it is a version of the ABLTerrainSolver able to perform LES of wind farm flows. The AD or the AL methods are included in order to simulate the presence of the turbines.
- **pisoFoamTurbine**: it is the OpenFOAM's standard pisoFoam solver, but with the actuator turbine models included. This solver can be used for simple cases

or for cases in which the importance of the atmospheric effects is negligible. An example of the application of it can be the testing of wind turbines inside a wind tunnnel. This was the solver chosen for this thesis work.

- **turbineTestHarness**: it is a very simple code that, coupled with the actuator line model, allows to test its setup. It works as pisoFoam, but the governing equations are not actually solved and the velocity field is constant through the domain, with the possibility of varying it in time. For this reason, the axial induction is not considered.

The characteristics of the three last solvers change a little bit depending on the turbine model chosen. For the windPlantSolver and the pisoFoamTurbine in fact five typologies are present: ADM, ALM, ADMAdvanced, ALMAdvanced and ALMAdvancedOpenFAST (when the coupling wth FAST is considered). For the turbineTestHarness instead only two options are allowed: ALM and ALMAdvanced. As already mentioned, the last solver is in fact used only for testing the actuator line model setup.

3.6.3 Inputs and Outputs

When a wind turbine (or a certain number of wind turbines) needs to be simulated, the structure of a case of SOWFA is basically the same of a common OpenFOAM case. The computational domain, with also the parameters of the mesh that characterizes it, has to be determined and the boundary and initial conditions are assigned. Then the numerical schemes, needed to perform the calculations in order to reach the solution, are chosen and the parameters related to the simulation (time step, start time, end time, etc.) are set. Three fundamental dictionaries that are able to characterize the simulated machines in a very complete way are:

- turbineArrayProperties
- turbineProperties
- airfoilProperties

Here all the information regarding the specific wind turbines present inside the domain are in fact contained. Inside these dictionaries, for example, the position and the dimensions of each turbine are specified, the polars for the blade profiles distributed along the blades are present, the number of actuator points and the characteristics of the projection function are chosen and all the parameters related to the control strategy are set.

At the end of a simulation, the results for each wind turbine at each time step can be found inside the postProcessing folder. Here two types of quantities are present: the global and the local ones. The global quantities are represented by a single number characterizing the entire machine for each time step, whereas the local quantities are distributed along all the actuator points composing the blades: a value for each of them can be found. Here below two tables containing the main global and local quantities are reported.

Global turbine quantities	Measurement unit	Description
rotorAxialForce	[N]	Thrust
rotorTorque	[Nm]	Torque
rotorPower	[W]	Power
rotorSpeed	[rpm]	Rotational Speed
rotorAzimuth	[°]	Position of the blades

Table 3.1. Global quantities

Blade local quantities	Measurement unit	Description
bladePitch	[°]	Pitch Angle
bladePointAlpha	[°]	Angle of Attack
bladePointCl	[-]	Lift Coefficient
bladePointCd	[-]	Drag Coefficient
bladePointLift	[N]	Lift Force
bladePointDrag	[N]	Drag Force
bladePointVradial	[m/s]	Radial Velocity
bladePointVtangential	[m/s]	Tangential Velocity
bladePointVaxial	[m/s]	Axial Velocity

Table 3.2. Local quantities

Almost the same quantities are computed also for the nacelle and the tower of each machine. However, their values are much less important and their effect on the performances of the machines is usually negligible.

Chapter 4

An ALM weakness: the shed vorticity representation problem

This chapter will be dedicated to the description of the phenomenon of the vorticities shed along the blades during a wind turbine operation. The difficulty in representing them with an AL approach will be then discussed and a model aimed at solving this problem will be introduced. In conclusion, the implementation of the model in SOWFA in order to try to take into account the real effect of the shed vorticities will be presented.

4.1 3D Aerodynamics

In section 2.1 the main characteristics related to a two-dimensional flow acting on a profile were already described. However, in reality the length of a wing in the third dimension plays a very important role in the determination of the exchanged forces. Every time a wing (or a blade) is subjected to an incident flow a pressure side and a suction side are generated (as already described for the 2D aerodynamics). The fact that the wing has a finite length together with the pressure difference between the two sides cause another flow along the span: it is pushed by the positive pressure towards the negative one. At the extremities of the wing the flow can pass from a side to the other one and the tip vortices are therefore generated. In the figure below a sketch representing the phenomenon for an airplane is reported.

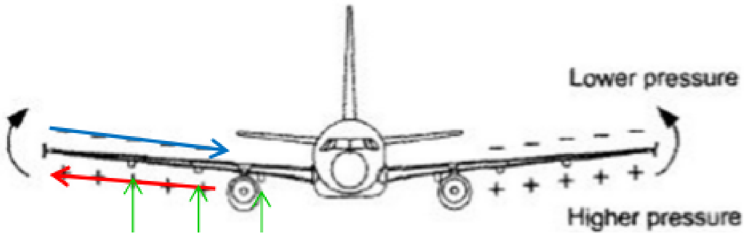

Figure 4.1. Sketch representing the difference in pressure between the two sides of an airplane wings

Moreover, the spanwise flow (both the one of the pressure side and the one of the suction side) is composed with the incoming one. This causes the generation of a series of vortices all along the wing length. They are the so called trailing-edge vortices and their intensity is much less than the one of the tip vortices. In figure 4.2 all the vortices shed by the wing are clearly visible.

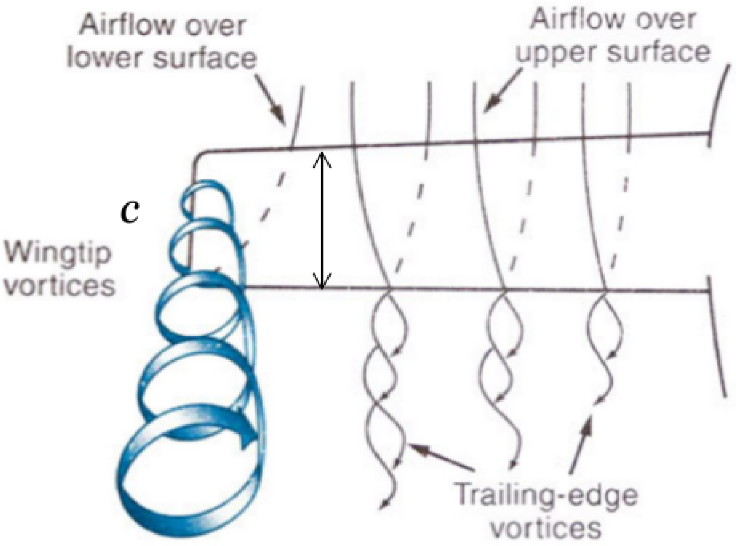

Figure 4.2. Sketch representing the shed vorticity along an airplane wing

The presence of this continuous sheet of streamwise vorticity does not affect only the turbulent characteristics of the flow downstream of the wing, but it influences also the way in which the aerodynamic forces are exchanged. A phenomenon called Downwash in fact occcurs. It is represented by the generation of a downwards velocity component at any spanwise position of the wing. The local angle of attack is therefore reduced of a quantity proportional to the intensity of the vortices and the effective angle of attack becomes:

$$\alpha_e = \alpha_g - \alpha_i \tag{4.1}$$

where α_g and α_i are respectively the geometrical and the induced angle of attack. This reduction in the angle of attack obviously causes a reduction also of the lift exchanged by the wing. In figure 4.3 the induced velocity $\vec{w}$, the undisturbed velocity $\vec{V_\infty}$ and the effective velocity $\vec{V_e}$ are shown. The resultant local lift force $\vec{R}$ is represented too: it is perpendicular to the effective incoming velocity. Moreover, also the induced drag $\vec{D_i}$ can be observed. It is the component of the resulting local lift force in the direction of the undisturbed flow. This is another effect of the downwash phenomenon.

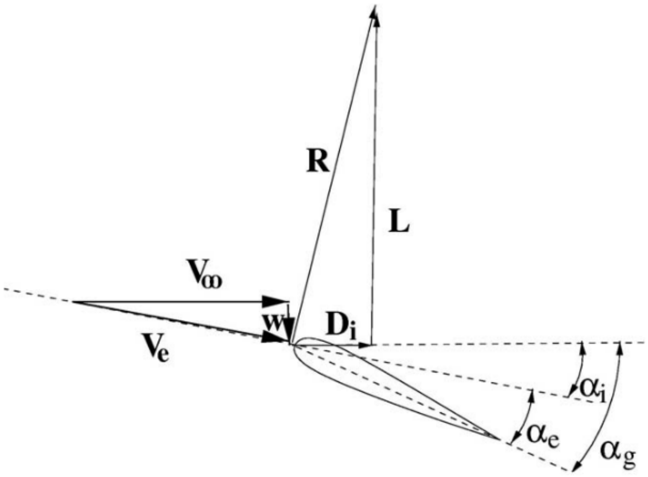

Figure 4.3. Sketch representing the effect of the downwash phenomenon on the angle of attack of the incoming flow

Also wind turbines are characterized by the presence of finite length rotating blades subjected to an incoming flow. For this reason, the continuous sheet of streamwise vorticity is generated downstream of the machine and the downwash phenomenon affects the upstream zone. The angle of attack of the effective relative incoming velocity is lower than the one of the undisturbed relative incoming velocity and so the obtainable power decreases too. In figure 4.4 the tip vortices (that are the ones with the highest intensity) are clearly visible. Due to the rotation of the blades a helical pattern is generated behind the machine.

Figure 4.4. A visualization of the tip vortices characterizing a wind turbine

For a deeper discussion about 3D aerodynamics the reader can refer to [16].

4.2 Influence of the projection width on the vorticity representation with an AL approach

One of the biggest advantages of the ALM with respect to the ADM is the capability of reconstructing the tip and the root vortices that characterize also a real wind turbine. However, their representation is extremely dependent on the width of the Gaussian projection function chosen in order to project the forces in the cells surrounding the blades. In fact the higher is the value of the projection width, the more the forces are spread over a larger zone. This affects the generation of the vortices: a bigger projection width means more diffused (and so less intense) vortices. In the figure below an application of the ALM considering different values for the projection width (ϵ) is reported.

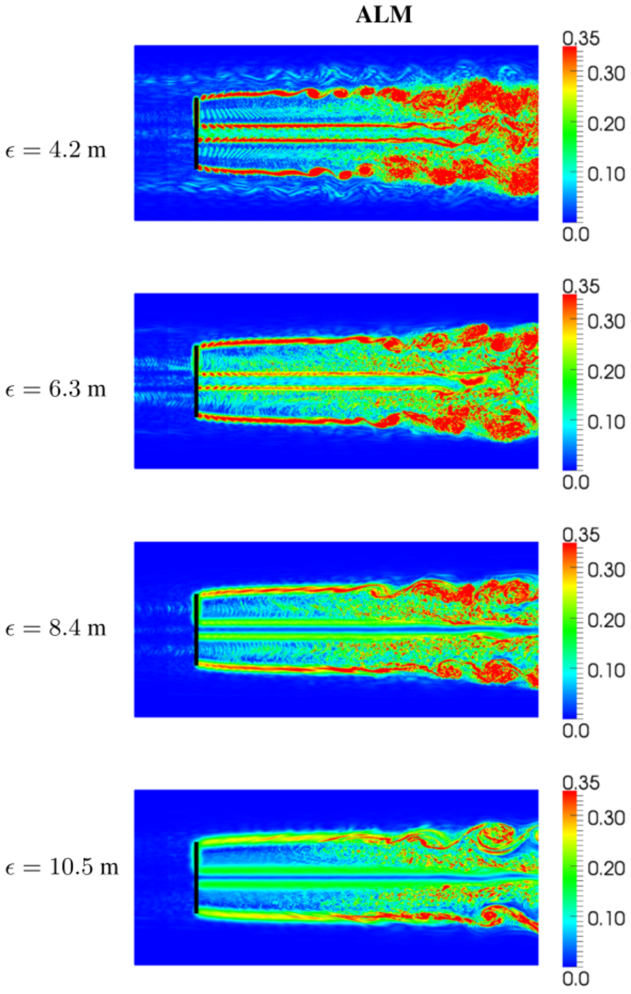

Figure 4.5. Influence of the ϵ value on the shed vorticity representation

It is clearly visible that by decreasing the ϵ value the turbulent structures generated downstream of the machine become more and more sharpened, intense and concentrated. As in a real case, the intensity of the generated vorticity does not influence only the turbulent characteristics of the flow, but also affects in a heavy way the

performances of the machine. Weaker shed vorticities mean in fact a less important effect of the downwash phenomenon to the incoming flow: the decrease in the angle of attack is less than in reality. This causes the fact that the higher is the value of the projection function width, the more the obtainable power is overestimated.
An optimal ϵ value able to reconstruct the tip and the root vortices in a way as realistic as possible was determined. In 2017 Martinez-Tossas, Churchfield and Meneveau [2] set the value for ϵ_{opt} approximately equal to one quarter the value of the chord. By choosing this value the real downwash effect could be recovered, the real angle of attack found and a power as close as possible to the real one reached.
However, due to the fact that ϵ needs to be at least twice the local grid cell length in order to avoid spurious flow field oscillations ([30]), this value is often very difficult to be reached. Especially when considering a certain number of wind turbines, larger values than the optimal one are chosen. Otherwise, the grid refinement should be increased a lot, leading to a much higher computational cost, often unsustainable.

4.3 Filtered Lifting Line Theory

The dependence of the ALM results from the width of the Gaussian function used for projecting the forces inside the computational domain was deeply investigated by many scientists. As already mentioned, this problem is especially important in the context of coarse-scale large-eddy simulations that cannot afford the fine resolutions required to resolve the optimal projection width ($\epsilon_{opt} \approx 0.25 chord$). This could happen, for example, when wind farms need to be simulated. In those cases the dimensions of the domain are very large and the number of cells should be extremely high if one wanted to reach the optimal width. This would lead to too high computational cost and time.
In 2018 Luis A. Martínez-Tossas and Charles Meneveau, with the aim of overcoming this obstacle in the representation of wind turbines with an AL approach, developed a model based on the well-known lifting line theory and reported it in an article published in 2019 titled “Filtered lifting line theory and application to the actuator line model” [3]. The lifting line theory is a model commonly used in order to describe the cumulative effect of shed vorticity from finite span lifting surfaces. In this case the lifting lines are the actuator lines used in order to simulate the presence of the rotating wind turbine blades. The difference with respect to the classical version of the theory is the presence in the ALM of the Gaussian projection function. This causes the smoothing of the generated vorticity: the higher is the value of ϵ, the thicker and weaker are the generated tip vortices. In order to reconstruct the induced velocity caused by the vortices in the zone upstream of the machine (downwash phenomen) the lifting line theory cannot be applied in its original version, but it needs to be filtered to take into account the effect of the projection function width. In this way an induced velocity vector in correspondence of each actuator point $\mathbf{x}_i(x_i, y_i, z_i)$ and dependent on the ϵ value can be obtained. The link between the unperturbed velocity, the sampled velocity and the induced velocity can be well represented by the following expression:

$$\mathbf{U}_\infty(\mathbf{x}_i) = \tilde{\mathbf{u}}(\mathbf{x}_i) - u_y(z_i; \epsilon^{LES})\mathbf{j} \tag{4.2}$$

where $\mathbf{U}_\infty$ is the unperturbed velocity, so the one that is not affected by the induced velocity caused by the shed vorticity, $\tilde{\mathbf{u}}$ is the velocity sampled in correspondence of each actuator point, u_y is the induced velocity that causes a decrease in the angle of attack and so also in the lift exchanged, ϵ^{LES} is the actual projection function width and $\mathbf{j}$ is the unit vector perpendicular to the direction of U_∞ (lift direction). As can be observed, u_y is a function of ϵ^{LES} and so it varies with the characteristics of the projection function. For this reason, as already said, this induced velocity is not able to represent the real effect on the incoming flow field.

However, the filtered lifting line theory can be applied also to a forces distribution characterized by the optimal projection function width ϵ_{opt}. In this way a mathematical formulation for the induced velocity that considers the optimal distribution can be derived. This is the induced velocity able to reproduce the real downwash phenomenon and that allows to recover the real exchanged forces. At this point, considering the difference between the two induced velocities ($u_y(z_i;\epsilon_{opt})$ and $u_y(z_i;\epsilon_{LES})$) a subfilter-scale velocity model can be obtained and applied to simulations that need to use a projection width larger than the optimal one. The application of the correction to the sampled velocity is represented by the following expression:

$$\hat{\mathbf{u}}(\mathbf{x}_i) = \tilde{\mathbf{u}}(\mathbf{x}_i) + [u_y(z_i;\epsilon^{opt}) - u_y(z_i;\epsilon^{LES})]\mathbf{j} \tag{4.3}$$

where the difference $\Delta u_y = u_y(z_i;\epsilon^{opt}) - u_y(z_i;\epsilon^{LES})$ is the subfilter velocity model that is applied to the sampled velocity $\tilde{\mathbf{u}}$ in order to recover the real incoming velocity $\hat{\mathbf{u}}$. In this way the same effect reachable with ϵ_{opt} can be obtained, the downwash phenomenon can be well reconstructed and the actual performances can be recovered. Hence, the results from the ALM can become independent of the ϵ value and the problems in using a projection function width larger than the optimal one can be solved.

Here below the main steps for the implementation of the model in the ALM are reported.

First of all, the following quantity is computed for each actuator point, considering the results of the previous time step:

$$G^{n-1} = \frac{1}{2}c(z_j)U_\infty^2(z_j)C_L(z_j) \qquad \text{for j=1,...,N} \tag{4.4}$$

where c is the chord at the position along the span in correspondence of the j^{th} actuator point, U_∞ is the unperturbed incoming velocity, C_L is the lift coefficient and N is the number of the actuator points.

At this point, it is possible to compute:

$$\Delta G^{n-1}(z_j) = \frac{1}{2}[G^{n-1}(z_{j+1}) - G^{n-1}(z_{j-1})] \qquad \text{for j=2,3,...,N-1} \tag{4.5}$$

and

$$\Delta G^{n-1}(z_1) = G^{n-1}(z_1) \qquad \text{for the first actuator point} \tag{4.6}$$

$$\Delta G^{n-1}(z_N) = -G^{n-1}(z_N) \qquad \text{for the last actuator point} \tag{4.7}$$

Then the induced velocity for both the optimal and the actual ϵ can be computed with the following expression:

$$u_y^{n*}(z_i;\epsilon_i) = -\sum_{j=1}^{N} \frac{1}{U_\infty(z_j)}\Delta G^{n-1}(z_j)\frac{1}{4\pi(z_i - z_j)}(1 - e^{-(z_i-z_j)^2/\epsilon_j^2}) \tag{4.8}$$

Finally the subfilter velocity can be obtained by considering the difference between the two induced velocities:

$$\Delta u_y^n(z_i) = f_u[u_y^{n*}(z_i;\epsilon_i^{opt}) - u_y^{n*}(z_i;\epsilon_i^{LES})] + (1-f_u)[u_y^{n-1}(z_i;\epsilon_i^{opt}) - u_y^{n-1}(z_i;\epsilon_i^{LES})] \quad (4.9)$$

and applied to the incoming sampled velocity:

$$\hat{\mathbf{u}}(\mathbf{x}_i) = \tilde{\mathbf{u}}(\mathbf{x}_i) + \Delta u_y^n(z_i)\mathbf{j} \quad (4.10)$$

For more information related to the different quantities considered and the way in which they are computed the reader can refere to [3].
The authors tested the proposed subfilter-scale velocity model in large-eddy simulations of flow over several fixed finite wings with uniform, non-turbulent inflow. They considered the LES code 'LESGO' in order to perform the simulations. The results were very promising, in fact they observed that the application of the correction allowed to eliminate the ϵ-dependence of the predicted aerodynamic forces. They were able to reconstruct in a very precise way the effects of the downwash phenomenon upstream of the wing and, in this way, results as close as possible to the real ones could be reached.

4.4 Implementation of the Filtered Lifting Line Theory in SOWFA

In [3] Martínez-Tossas and Meneveau showed that their model based on the filtered lifting line theory is able to well reproduce the effect of the downwash phenomenon in a way independent of the width of the gaussian projection function used for spreading the forces in the zone surrounding the actuator lines. They in fact applied it during the simulation of flows over several fixed wings and observed that, considering different values for ϵ, the same results can be always obtained.
The objective of this thesis work was to apply the model also to a wind turbine simulated by an AL approach. In this case in fact the characteristics of the flow are quite different with respect to the ones of the uniform flow over a fixed wing: unsteadiness and turbulence affect it in a heavy way.
As already said, the tool used in order to perform the simulations was SOWFA. For this reason the model was implemented inside it. The class that was modified in order to take into account the presence of the model is the *horizontalAxisWindTurbinesALMAdvanced* class.

4.4.1 Two different options for the model implementation

Two different options for the implementation of the model in SOWFA were considered. The difference between them stands in the capability of reaching the ϵ-independence. In fact, the results obtained with the first option seem to show a stronger independence from the ϵ value. However, the first option does not influence the wake generated by the presence of the machine and so it is not useful if one wants to observe the effect on the flow or to study the interaction with another turbine placed downstream. Instead the second option, although the ϵ-dependence increases a little bit with respect to the

first option, causes a variation in the flow field with respect to the standard version of SOWFA and this allows to study the effect of the model on the wake and not only on the wind turbine performances.
The way in which the two different options work will be explained in the two following sections, whereas their effect on the performed simulations will be clearer when the results will be examined.

First Option

The first option for the model implementation can be clearly described thanks to the following scheme:

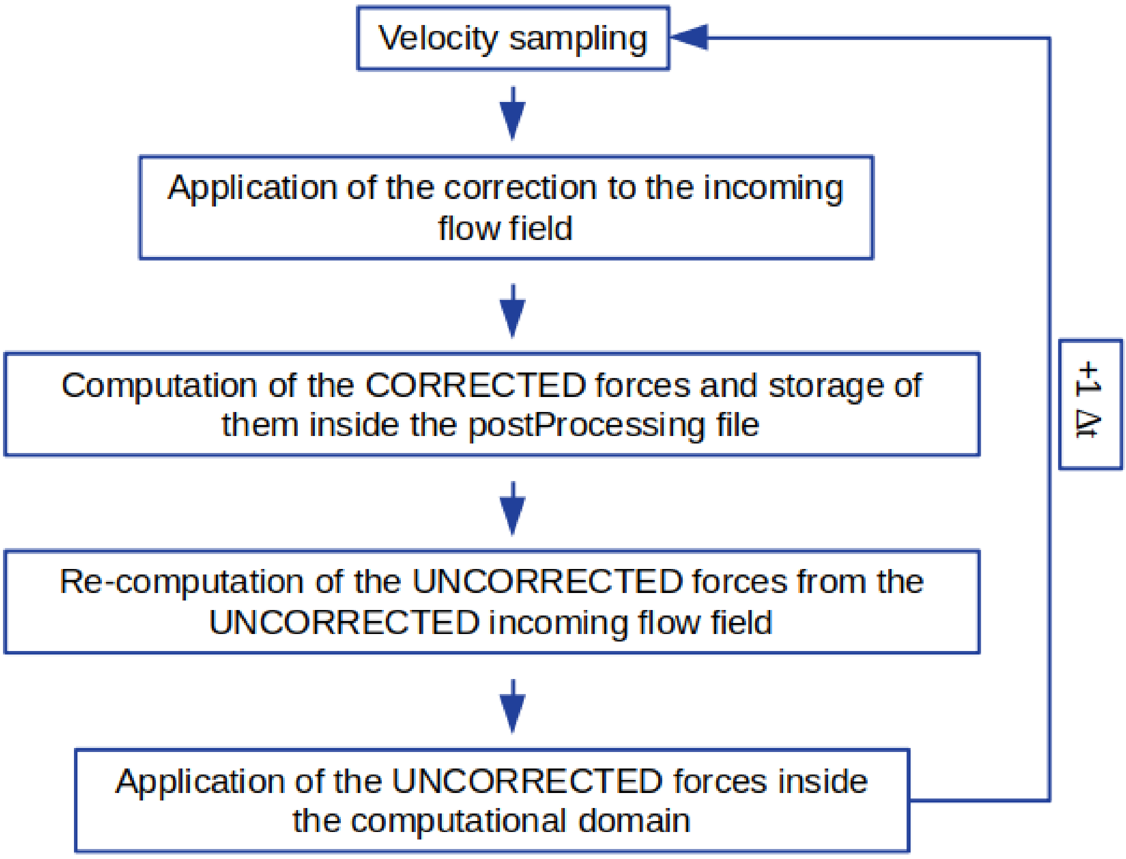

The velocity is sampled in correspondence of each actuator point (the local velocity sampling is considered). By summing up also the effect of the blade rotation, the incoming velocity seen by the blade in the standard version of SOWFA can be found. At this point the subfilter-scale velocity model can be applied and the angle of attack is corrected. The forces that consider the new angle of attack of the incoming flow can therefore be computed and stored inside the post-processing file. Then, considering the uncorrected flow field (the one sampled by the standard version of SOWFA), the uncorrected forces are computed and applied inside the computational domain. In this way, the incoming flow field at the next time step will feel the presence of the uncorrected forces and so at each time step the correction is applied exactly to the

same conditions that occur with the standard version of SOWFA.
As already said, this first option seems to reach a stronger independence from the ϵ value (as will be shown in the results), but does not allow to study the effect of the model on the flow field.

Second Option

Once again a scheme can be useful in order to understand how the second option of the model implementation works:

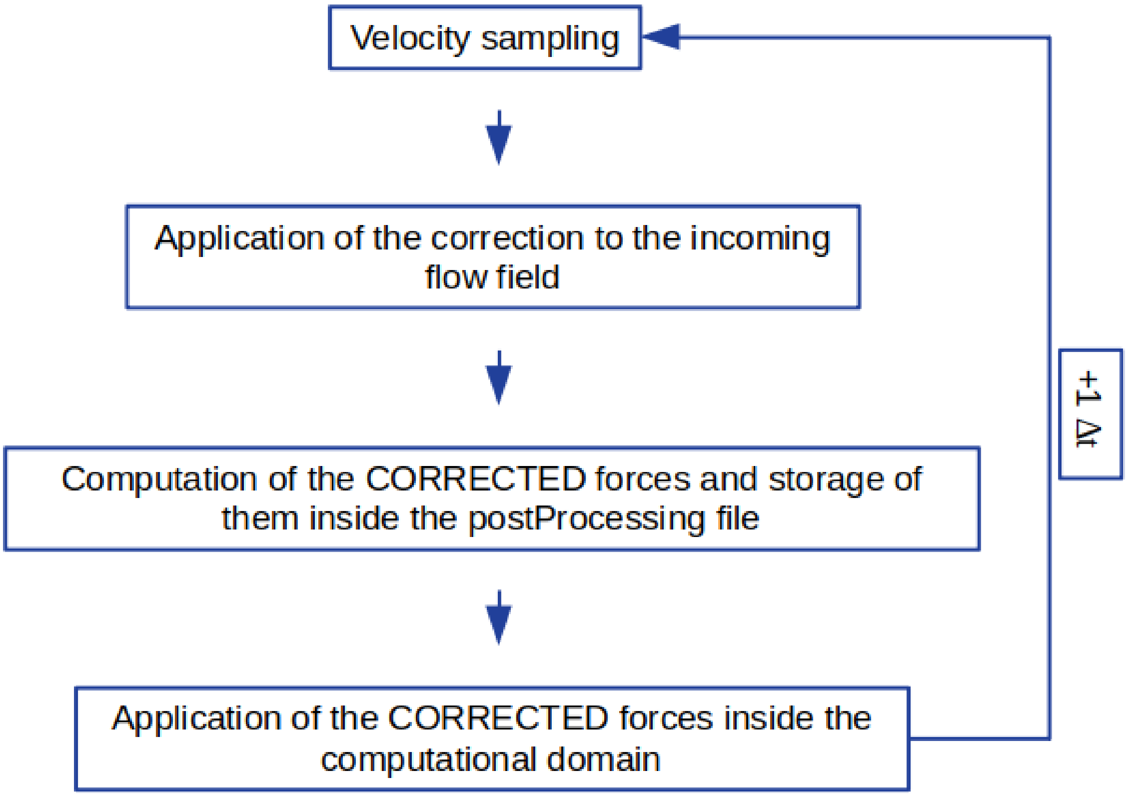

As for the first option, the velocity is sampled, the correction is applied and the corrected forces are computed. At this point the corrected forces are not only stored inside the post-processing file, but they are also applied inside the computational domain. This causes a variation of the flow field with respect to the standard version of SOWFA. For this reason at the next time step the incoming flow will feel the presence of the already corrected forces, it will be influenced by them and so it will be different from the one sampled by SOWFA in normal conditions. This second option therefore allows to observe the effect of the model on the flow field, especially on the wake. However, the dependence on the ϵ value seems to increase a little bit with respect to the first option, as will be shown in the results.

4.4.2 Introduction of the new variables and of the new function

In order to implement the model in SOWFA, two files were modified. They are the *horizontalAxisWindTurbineALMAdvamced.H* and the *horizontalAxisWindTurbineALMAdvanced.C* files. Inside the first one the new variables useful for the introduction of the correction on the incoming flow field were declared, whereas in the second one the function able to compute the correction was added. In the following table the new variables are listed and their type indicated:

Name	Type
bladePointClOld	DynamicList<scalar>
G	DynamicList<scalar>
dG	DynamicList<scalar>
sumLES	Scalar
sumOPT	Scalar
bladePointPerturbation	DynamicList<scalar>
bladePointPerturbationOld	DynamicList<scalar>
notInfluencedVelocityParallelVector	Vector
bladePointPerturbationVector	Vector
bladePointAlphaNoCorrection	DynamicList<scalar>
bladeWindVectorsSampled	DynamicList<vector>

Table 4.1. New variables

These variables can be referred to the expressions of 4.3, where the main steps for the implementation of the model are reported.

The variable *bladePointClOld* in fact is introduced in order to save the corrected lift coefficient of the previous time step and to be considered inside the calculation of $G^{n-1}(z_j)$, that in SOWFA is represented by the variable G. The quantity $\Delta G^{n-1}(z_j)$, instead, is translated with the variable *dG*. *sumLES* and *sumOPT* are the summatories of the expression 4.8: the first one is referred to the actual ϵ value, whereas the second one is referred to the optimal value of it. *bladePointPerturbation* and *bladePointPerturbationOld* are the modules of the correction at the current time step and at the previous time step. Both are needed because the real correction that is applied is a combination of the two (otherwise numerical issues arise). The direction parallel to the incoming uncorrected flow is saved in the variable *notInfluencedVelocityParallelVector* and the correction is applied in the direction perpendicular to it and to the blade-span direction. The subfilter-scale velocity vector is then saved in *bladePointPerturbationVector*. Finally, the two last variables *bladePointAlphaNoCorrection* and *bladeWindVectorsSampled* are used in order to save respectively the uncorrected angle of attack and the uncorrected incoming velocity vector.

All these variables are then considered inside the new function in the *horizontalAxisWindTurbineALMAdvanced.C* file. The part of the code related to the new function *computeBladeFilteredWindVectors* is reported in Appendix A.

4.4.3 Differences in the implementation for the two options

The function introduced in the previous section is present in both the options of the implementation of the model. In fact the procedure for computing the correction is the same for both. As already said, what changes is the type of forces that are applied inside the computational domain and that cause a variation of the flow field. For the first option the forces that are applied are the uncorrected ones. In this way, the incoming flow field feels the presence of the same forces considered by the standard version of SOWFA and introduces the correction on them. For the second option, instead, the corrected forces are applied directly inside the computational domain. The incoming flow field feels their presence and is modified accordingly.

Inside the *horizontalAxisWindTurbineALMAdvanced.C* file, this is taken into account in the function named *computeBladePointForce*. This is already used by the standard version of SOWFA for computing the forces exchanged by the blades, considering the incoming velocity sampled in correspondence of each actuator point.

For what regards the second option, this function remains almost unchanged. In fact the new incoming velocity vector is already found in the *computeBladeFilteredWindVectors* function. The *computeBladePointForce* function then takes it as input and computes the forces that are directly applied inside the domain. For the first option instead some modifications had to be performed. A part in which the uncorrected incoming velocity is considered again in order to compute the uncorrected forces was added. In this way both the corrected and the uncorrected forces are computed. The first ones are saved inside the *postProcessing* file, whereas the second ones are applied inside the domain.

Finally, some other small differences needed to be introduced inside the *horizontalAxisWindTurbineALMAdvanced.C* file. They are related especially to the way in which the quantities are saved inside the *postProcessing* file, useful for analyzing the performances of the tested machine.

Chapter 5

Cases studied

This chapter is dedicated to the description of the two cases considered in this thesis work: the NREL 5 MW wind turbine and the scaled version of the DTU 10 MW wind turbine. For both, the machine will be introduced and a precise description of the setup of the simulations that were performed will be made.

5.1 NREL 5 MW wind turbine

This section has the aim of introducing the first machine considered. It is the NREL 5 MW reference wind turbine, a machine designed by NREL.

For what regards instead the setup of the simulations, both the options for the implementation of the model were considered in order to observe the difference in the obtained results. Moreover, four different values for the gaussian projection function width were taken into account. This was done in order to test the effectiveness of the correction, introduced by the model. Finally, two different levels of refinement were considered for the mesh characterizing the computational domain. However, a grid independence analysis was not performed. The objective of this thesis in fact is not to reach the grid independence or to study the effect of the level of refinement of the mesh on the results. The model has to be able to work whatever is the level of refinement of the mesh considered and its effect on the ϵ-dependence should always be observable. Two meshes were considered just to observe if the refinement level could have any influence on the effectiveness of the model.

5.1.1 Description of the machine

The “NREL offshore 5 MW baseline wind turbine” is not a real machine, but it is a large wind turbine designed by NREL, based on realistic and standardized input data, that is representative of typical utility-scale land- and sea-based multimegawatt turbines and suitable for deployment in deep waters. In the table below the general characteristics of the machine are reported:

Rating	5 MW
Rotor orientation, configuration	Upwind, 3 Blades
Control	Variable Speed, Collective Pitch
Drivetrain	High Speed, Multiple-Stage Gearbox
Rotor, Hub diameter	126 m, 3 m
Hub height	90 m
Cut-In, Rated, Cut-Out Wind Speed	3 m/s, 11.4 m/s, 25 m/s
Cut-In, Rated Rotor Speed	6.9 rpm, 12.1 rpm
Rated Tip Speed	80 m/s
Overhang, Shaft Tilt, Precone	5 m, 5°, 2.5°

Table 5.1. NREL 5 MW wind turbine characteristics

As it is possible to observe in the table, the machine is equipped with two basic control systems: a generator-torque controller and a full-span rotor-collective blade-pitch controller. They are designed to work independently and allow the variation of the rotational speed of the turbine and of the pitch angle of the blades. The objective of the generator-torque controller is to maximize the power capture below the rated operation point, whereas the one of the blade-pitch controller is to regulate the generator speed above the rated operation point. However, for this thesis work any type of control system was disabled. This was done in order to put the attention only on the aerodynamic aspects and to avoid the influence of any other factors. The way in which the flow interacts with the blades and the generation of the aerodynamic forces are in fact of fundamental importance for the overall performance of the machine. The shape of the sections of the blades is at the basis of them. The table below contains the blade profiles distributed along the span. Moreover the chord and the twist angle in correspondence of each radial position are reported.

Radius	Chord	Twist angle	Profile
2.8667 m	3.542 m	13.308°	Cylinder1
5.6000 m	3.854 m	13.308°	Cylinder1
8.3333 m	4.167 m	13.308°	Cylinder2
11.7500 m	4.557 m	13.308°	DU40
15.8500 m	4.652 m	11.480°	DU35
19.9500 m	4.458 m	10.162°	DU35
24.0500 m	4.249 m	9.011°	DU30
28.1500 m	4.007 m	7.795°	DU25
32.2500 m	3.748 m	6.544°	DU25
36.3500 m	3.502 m	5.361°	DU21
40.4500 m	3.256 m	4.188°	DU21
44.5500 m	3.010 m	3.125°	NACA64
48.6500 m	2.764 m	2.319°	NACA64
52.7500 m	2.518 m	1.526°	NACA64
56.1667 m	2.313 m	0.863°	NACA64
58.9000 m	2.086 m	0.370°	NACA64
61.6333 m	1.419 m	0.106°	NACA64

Table 5.2. Distribution of the Aerodynamic Properties along the blade

Each profile is characterized by a specific trend for the lift coefficient and the drag coefficient, functions of the angle of attack.
For more information about the NREL 5 MW reference turbine the reader can refer to [31].

5.1.2 Computational domain and mesh characteristics

For testing the NREL 5 MW reference turbine, the domain considered is cubique and the center of the turbine rotor is located at the center of it. The mesh is structured and characterized by cubique cells. This was allowed by the use of the ALM for modeling the turbine. Indeed, as already said, the fact that the geometry of the machine is not reconstructed inside the domain and that the presence of the turbine is just mimicked by the insertion of the exchanged forces in correspondence of the actuator points, leads to a much simpler mesh generation process.
The mesh is also characterized by a certain number of local refinements, that allow to better capture some phenomena in some zones of interest without decreasing the cell dimension in the entire domain. They were performed by considering a certain number of concentric cylinders (equal to the number of local refinements). They have the center in correspondence of the turbine rotor center, whereas the two bases are defined in such a way that the refined zone begins a bit upstream of the machine and is able to capture the wake generated by it. The two figures below show the computational domain with the second level of refinement. The first one represents a global view of it, whereas in the second one it is possible to observe a local view of the refined zone seen from behind.

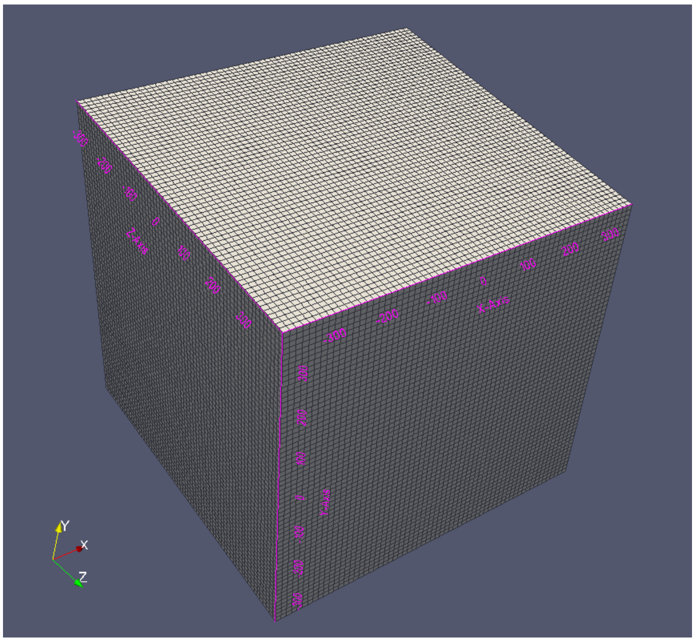

Figure 5.1. Computational domain for the NREL 5 MW wind turbine case

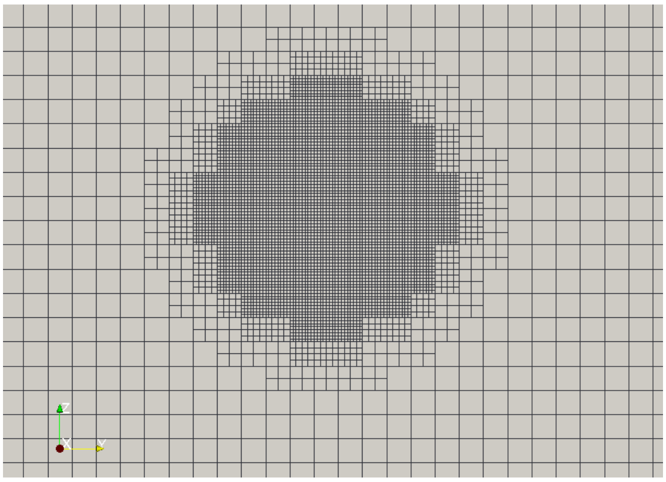

Figure 5.2. View of the refined zone in the area near the machine

The x direction represents the direction of the incoming wind flow, whereas the y-z plane is the one that contains the area swept by the turbine rotor. The extension of the domain along each direction is of 756 m (6 times the dimension of the rotor diameter).

As already mentioned, two meshes with two different levels of refinement were considered. Their characteristics are reported in the table below.

	First refinement level	Second refinement level
Number of cells	989316	2551101
Cell dimension in the refined zone	2 m	1.5 m
Number of cells along the rotor diameter	64	84

Table 5.3. Characteristics of the two meshes

5.1.3 ALM parameters

The most important parameters that need to be set with an actuator line approach are the way in which the incoming velocity is sampled, the number of actuator points and the gaussian projection function width (ϵ).
As already described in 3.5.3, the approach chosen for the velocity sampling was the local one: the incoming velocity was sampled in correspondence of each actuator point.
For what regards instead the number of actuator points, the choice taken was not the common one. In literature in fact the recommended number of actuator points for each blade is about 40. This should allow to reach a reliable representation of the wind turbine and of its exchanged forces. However, for the simulations performed for this thesis work a much higher number was chosen: it was set to 300 for each blade. The reason is that 40 actuator points are not enough to reconstruct in a very precise way the real effect of the shed vorticity. The use of 300 points, instead, allows an optimal application of the model, especially in the tip region.
Finally, for the gaussian projection function width four different values were tested: 5 m, 8 m, 10 m, 12 m. As already explained, this was done in order to study the effectiveness of the model on the final solution and to observe how the ϵ-dependence varies comparing the standard version of SOWFA and the one with the correction applied. The final objective of the model is in fact to obtain outputs that are independent of the width set for the projection function.

5.1.4 Boundary conditions

As in any OpenFOAM case, the boundary conditions need to be set. This means that the flow conditions in correspondence of the boundaries of the computational domain are specified. They are reported in the table below:

	p	U	k	nuSgs
Inlet	zeroGradient	fixedValue	fixedValue	fixedValue
Outlet	fixedValue	InletOutlet	zeroGradient	zeroGradient
Lateral patches	Cyclic	Cyclic	Cyclic	Cyclic
Upper	Cyclic	Cyclic	Cyclic	Cyclic
Lower	Cyclic	Cyclic	Cyclic	Cyclic

Table 5.4. Boundary conditions

5.1.5 Numerical Schemes

The different terms inside the Navier Stokes equations need to be discretized in order to reach the solution. The numerical schemes used are:

- the backward scheme for the time discretization;
- the Gauss linear scheme for the gradient discretization;
- the Gauss linear scheme for the divergence discretization;
- the Gauss linear scheme for the laplacian discretization.

The backward scheme is a useful scheme for simulating transient phenomena (as in this case) and it is a second order implicit, potentially unbounded scheme. The Gauss linear scheme is a second order unbounded scheme, based on linear interpolation.

5.1.6 Resolution Algorithm

As already anticipated in chapter 3 the algorithm chosen for the resolution process was the PISO (Pressure-Implicit with Splitting of Operators) algorithm. The number of correctors was set to 3. It represents the number of iterations of the momentum predictor and the pressure correction for each time step.

For what regards the linear equations solution a conjugate-gradient solver with a Generalised Algebraic Multi-Grid (GAMG) pre-conditioner was considered for the pressure. For the velocity, instead, a bi-conjugate gradient solver with a diagonal incomplete LU pre-conditioner was used.

5.1.7 Other simulation settings

In order to perform the simulations needed for testing the model implemented in SOWFA, some other choices had to be taken and other parameters had to be set.

For example the time step, that represents the time discretization of the simulations, was fixed equal to 0.015 s. This choice was taken in order to have a Tip Courant number lower than one. This parameter is found by making the ratio between the time step set and the time taken by the blade tip for passing through one cell. Maintaining it below 1 allows to better capture the phenomena simulated and to avoid spurious oscillations in the results, that could lead to divergence.

Another decision taken was to not consider the presence of the nacelle and the tower. This was done basically for two reasons. The first one is that the model acts only on the incoming flow to the blades and it does not influence the velocity in correspondence of the tower and the nacelle. Therefore, they were not considered in order to put the attention only on the aerodynamics of the blades. The second one is based on the fact that the influence of the tower and the nacelle on the performance of the machine is very limited and so the difference in the final results is almost null.

Finally, two other values were fixed: the wind velocity at the inlet of the domain and the rotational velocity of the machine. The first one was maintained constant for all the duration of the simulations and set equal to 8 m/s. The second one instead was introduced equal to 9.16 rpm. As already said any type of control strategy was disabled. This forced the rotational velocity to remain constant during all the simulations.

5.2 DTU 10 MW wind turbine

This section is dedicated to the introduction of the scaled version of the DTU10MW reference wind turbine [32] [33] and to the description of the setup of the simulations that were performed on it. The machine was considered during the Unsteady Aerodynamics of FLOating Wind turbines (UNAFLOW) project [34]. It was a collaborative project, that started in June 2017 and ended in April 2018, that involved four research institutions: Politecnico di Milano (POLIMI), The Netherlands Organisation for applied scientific research (TNO), University of Stuttgart (USTUTT) and Technical University of Denmark (DTU). The main objective was to compare wind tunnel tests with high-fidelity simulations results of a Floating Offshore Wind Turbine (FOWT) under imposed surge motion. However, for this thesis work only the fixed configuration of the wind turbine was tested and the model was applied to it. As already done for the NREL 5 MW, the simulations were performed considering the standard version of SOWFA and the one with the model implemented with both the options. Also in this case four different values for the gaussian projection function width were considered and two different levels of refinement for the mesh were tested, even if, as already explained, the model must be able to work independently from the cell dimension. Finally, for what regards instead the number of actuator points along each blade two different options were taken into account: 300 and 40. The first one is the same adopted for the NREL 5 MW case, whereas the second one was introduced in order to show what happens to the reconstruction of the effects of the vortices when a too low number is considered.

5.2.1 Brief introduction about the experimental campaign

In order to study and observe the behaviour of the real scaled wind turbine, a vast experimental campaign was conducted in the wind tunnel of Politecnico di Milano (GVPM). The tests were performed inside the Boundary Layer Test Section, which is characterized by a width of 13.84 m, a height of 3.84 m and a length of 35 m. The section is devoted to studies about structures that are subjected to atmospheric flow conditions. Moreover, neither roughness elements nor turbulence generators were used. This was done in order to obtain an inflow velocity profile as constant as possible. In the rotor zone in fact the wind speed could be considered constant with a turbulence intensity of about 2%. In the figure below the wind speed and the turbulence intensity vertical profiles are shown.

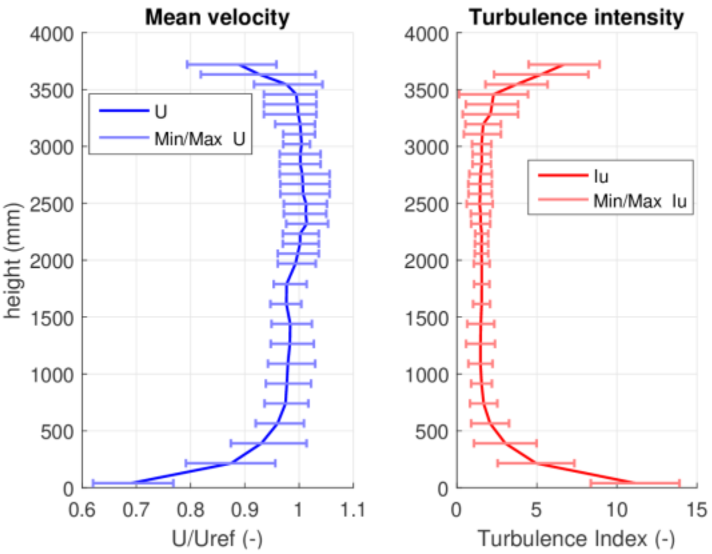

Figure 5.3. Wind speed and turbulence intensity vertical distributions of the flow inside the GVPM

As already said, the tested machine was a scaled version of the DTU10MW Reference Wind Turbine. It was designed by Politecnico di Milano for the LIFES50+ project in 2015 and some minor changes were introduced ahead of the UNAFLOW project. In order to test the turbine, it was mounted on a slider, able to reproduce a surge motion by means of an hydraulic actuator. Moreover, also the pitch motion could be represented thanks to the presence of a second hydraulic actuator. However, as already mentioned, only the fixed configuration was considered for this Thesis work. In the figure below a schematic representation of the experimental set up is reported.

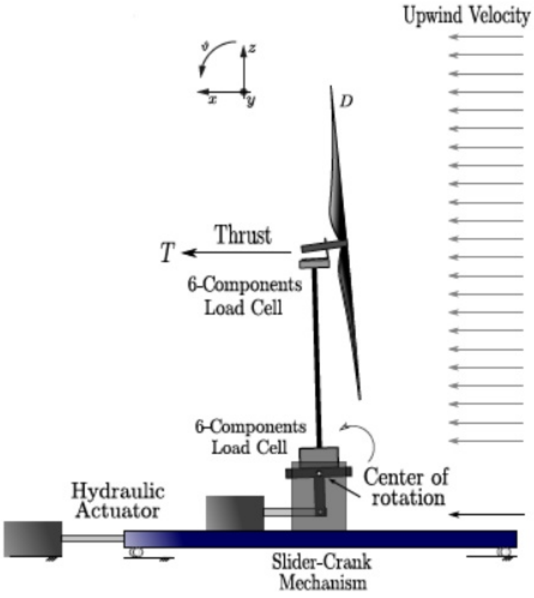

Figure 5.4. A representation of the experimental setup useful for testing the machine

In conclusion, for what regards the flow field inside the wind tunnel, the incoming wind speed was measured 5 m upstream the turbine at a height of 1.5 m.

5.2.2 Description of the machine

The characteristics of the scaled version of the DTU10MW Reference wind turbine tested in the wind tunnel are reported in the following table.

Configuration	3-bladed, clockwise upwind rotation
Control	Variable speed + individual pitch
Drivetrain	Transmission belt, epicyclic gearbox
Rotor diameter	2.38132 m
Blade length	1.10166 m
Hub height	2.086 m
Hub diameter	0.178 m
Overhang	0.09467 m
Tilt angle	5°
Coning angle	0°
Twr2Shft	0.03667 m
Tower Diameter	0.075 m

Table 5.5. characteristics of the scaled version of the DTU 10 MW wind turbine

As already observed for the NREL5MW, also in this case the system was equipped with an active control. However, the experimental tests were performed only considering a fixed rotor speed and a fixed pitch angle. The same thing was done for the simulations with the actuator line method, whose results will be shown later. As already mentioned, this allowed to put the attention only on the aerodynamic aspects avoiding any possible influence from other factors.

In the table below instead the distribution of the chord and the twist angle along the blade is reported. Moreover, each radial position is characterized by a different type of profile, chosen in order to optimize the operation of the machine.

Distance from blade root	Chord	Twist angle
0.00000 m	0.05585 m	17.07668°
0.05817 m	0.05678 m	17.04199°
0.13641 m	0.07573 m	15.77593°
0.21766 m	0.10620 m	12.30509°
0.30059 m	0.11490 m	9.98299°
0.38379 m	0.11044 m	8.65143°
0.46581 m	0.10236 m	7.56522°
0.54530 m	0.09272 m	6.38165°
0.62105 m	0.08288 m	5.08008°
0.69211 m	0.07356 m	3.79042°
0.75778 m	0.06516 m	2.61685°
0.81765 m	0.05778 m	1.59090°
0.87153 m	0.05141 m	0.71754°
0.91947 m	0.04604 m	0.03751°
0.96171 m	0.04163 m	-0.53510°
0.99860 m	0.03796 m	-1.03393°
1.03056 m	0.03440 m	-1.46251°
1.05807 m	0.03054 m	-1.61172°
1.08162 m	0.02541 m	-1.60710°
1.10166 m	0.00998 m	-1.72236°

Table 5.6. Distribution of the chord and the twist angle along the blade

5.2.3 Computational domain and mesh characteristics

The computational domain aimed at reproducing faithfully the Boundary Layer Test Section of the GVPM, where UNAFLOW tests were conducted. Its shape is represented by a parallelepiped with a cross section characterized by a width of 13.84 m and a height of 3.84 m. The dimension in the streamwise direction is instead 20.36 m. In particular the patch characterizing the inlet of the domain was placed 5 m upstream of the turbine. This was done in order to put the inlet of the computational domain in correspondence of the position where the inflow velocity was experimentally measured. This allowed to set the boundary conditions in a way as close as possible to the real ones. Then, by considering the overall length of the computational domain, it is possible to derive the position of the outlet section: it was placed 15.36 m downstream of the machine.

As already seen for the NREL 5MW wind turbine, the mesh inside the domain is structured and the cells are almost cubique. Once again, a certain number of local refinements was introduced in order to well capture the wake behind the turbine and to reconstruct in a right way the zone just upstream of the machine. The latter is in fact the zone that most influences the final performance of the machine and a good reconstruction of it allows to mimic the behaviour of the turbine as realistically as possible.

In the two figures below the computational domain is represented. The first one offers an overall view of it, whereas the second one shows the refined zone.

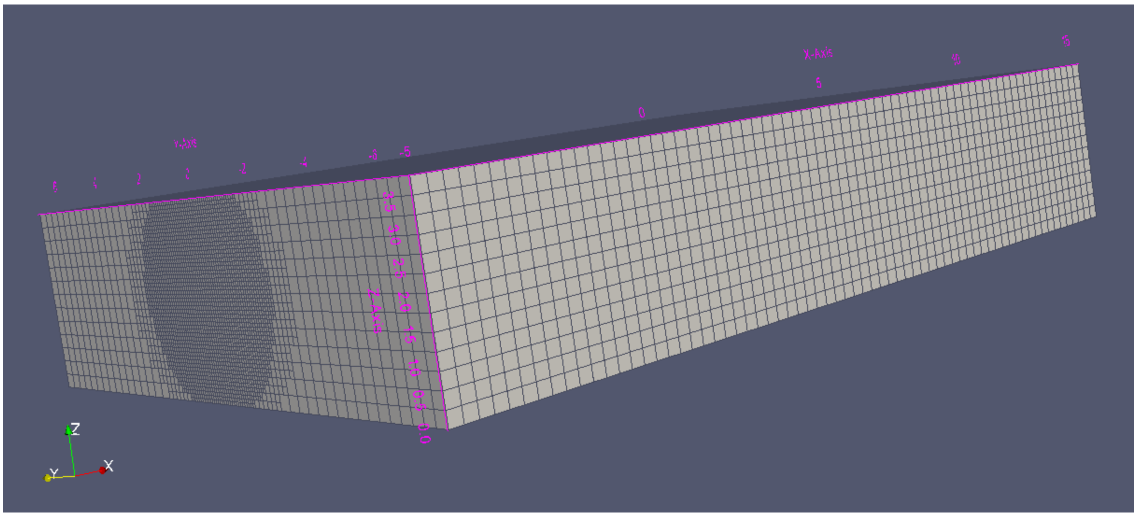

Figure 5.5. Computational domain for the DTU 10 MW scaled wind turbine case

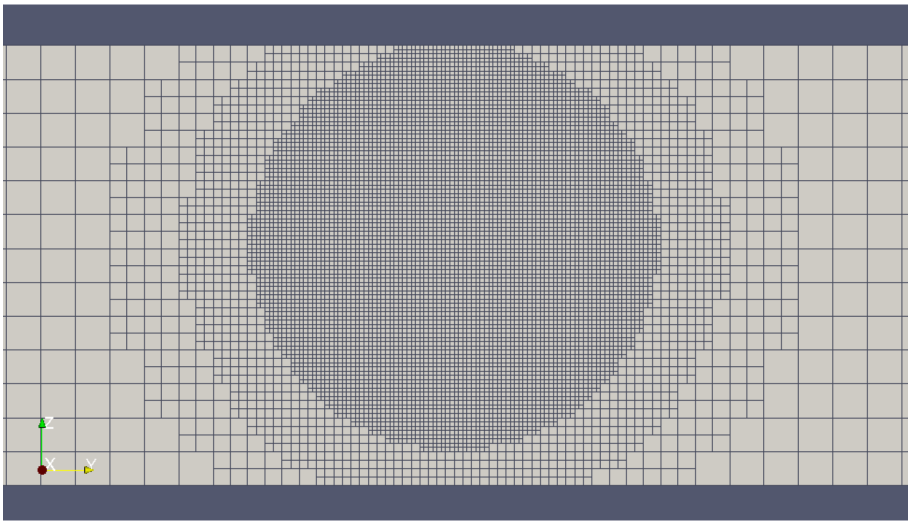

Figure 5.6. View of the refined zone in the area near the machine

In the table below, instead, the characteristics of the two meshes, each characterized by a certain level of refinement, are reported.

	First refinement level	Second refinement level
Number of cells	4202388	8211480
Cell dimension in the refined zone	0.037 m	0.029 m
Number of cells along the rotor diameter	64	80

Table 5.7. Characteristics of the two meshes

5.2.4 ALM parameters

Also for the simulations performed on the scaled version of the DTU10 MW Reference Wind Turbine, the option chosen for sampling the incoming velocity was the local one. The velocity in fact was sampled in correspondence of each actuator point and the value obtained was used in order to compute the forces acting on the blades. For what regards instead the width of the gaussian projection function, four different values were considered. They were 0.074 m, 0.01 m, 0.15 m and 0.22 m. This allowed to perform the analysis on how the ϵ-dependence varies after the introduction of the model.

Finally, as already mentioned, differently from the previous case, two options for the number of the actuator points along each blade were taken into account. Both the configuration with 40 points and the one with 300 points were tested. This was done in order to observe which are the advantages in choosing a higher number for the actuator points. Indeed, as will be shown, the difference in the results when considering the standard version of SOWFA is almost negligible, but when the model is introduced a difference can be observed. This is caused by the fact that the higher is the number of the actuator points along each blade, the more effective is the application of the correction to the incoming velocity. The model in fact tries to recover the real effects of the shed vorticities on the performances of the machine: with a too low number of points their effect cannot be well captured.

5.2.5 Boundary conditions

The conditions set at the boundaries of the computational domain are contained inside the following table:

	p	U	k	nuSgs
Inlet	zeroGradient	fixedValue	fixedValue	fixedValue
Outlet	fixedValue	InletOutlet	zeroGradient	zeroGradient
Lateral patches	zeroGradient	slip	zeroGradient	slip
Upper	zeroGradient	slip	zeroGradient	slip
Lower	zeroGradient	slip	zeroGradient	slip

Table 5.8. Boundary conditions

5.2.6 Numerical schemes

For the case of the DTU10MW wind turbine, the schemes chosen for the discretization of the terms inside the Navier Stokes equations are the following ones:

- the backward scheme for the time discretization;
- the Gauss linear scheme for the gradient discretization;
- the Gauss linear scheme for the divergence discretization;
- the Gauss linear scheme for the laplacian discretization.

5.2.7 Resolution algorithm

As for the case of the NREL 5 MW wind turbine, the algorithm devoted to the resolution process was the PISO (Pressure-Implicit with Splitting of Operators) one with a number of correctors equal to 3.

For the solution of the linear equations a conjugate-gradient solver with a GAMG pre-conditioner was used for the pressure and a bi-conjugate gradient solver with a diagonal incomplete LU pre-conditioner for the velocity.

5.2.8 Other simulation settings

Also for this case, some other important parameters need to be set. They are fundamental to perform reliable simulations able to mimic in the best way the reality. First of all the time step of the simulations was set equal to 0.001 s. As for the previous case, this was done in order to reach a Tip Courant number lower than one. This choice should bring to results not affected by spurious instabilities.

Differently from the NREL 5 MW case, the simulations performed for the scaled version of the DTU10MW reference wind turbine considered also the presence of the tower. This choice was taken just to make the simulations as close as possible to the experimental tests performed in the wind tunnel. In fact, even if the influence of the presence of the tower on the final results is almost negligible, the inclusion of the tower inside the computational domain allowed a more reasonable comparison between the results from the CFD and the experimental ones. The nacelle instead was not taken into account during the simulations. The rotor and the tower in fact were considered enough to describe in a complete way the presence of the wind turbine inside the wind tunnel.

Finally, as for the previous case, the value of the wind velocity at the inlet of the domain and the rotational velocity of the machine were chosen. They are both fixed and their values are respectively 4 m/s and 242 rpm. Once again, as already mentioned, no control strategies were introduced.

Chapter 6

Results

In this chapter all the results coming from the simulations performed on both the machines are grouped. The time history of some global quantities and the spanwise distribution of the local ones will be shown, the effectiveness of the model considering the two options for the implementation and different values for the gaussian projection function width will be analysed and a comparison between the two levels of refinement of the mesh considered for both the machines will be reported. Moreover, for what regards only the scaled version of the DTU 10 MW reference wind turbine, some extra aspects will be taken into account. First, a comparison considering 40 and 300 actuator points will be performed and the importance of using a higher number of actuator points when the model is applied will be evidenced. Then, the wake behind the machine will be analysed and the effect of the application of the model on the flow will be observed. Obviously for this type of analysis only the second option for the implementation of the model can be considered. This is in fact the one that applies directly the corrected forces inside the computational domain. In this way the flow around the turbine is influenced and it turns out different from the one with the standard version of SOWFA. Finally, a comparison of the DTU 10 MW wind turbine performances obtained from the simulations with some results coming from the experimental tests in the wind tunnel will be also considered.

6.1 NREL 5 MW wind turbine

6.1.1 Global quantities time history

The global quantitites chosen for showing their trend in time are the power and the thrust. Here below the results from the standard version of SOWFA, the ones from SOWFA with the first option of the model and the ones with the second option implemented are reported. For the moment, only the results related to the most refined mesh are shown.

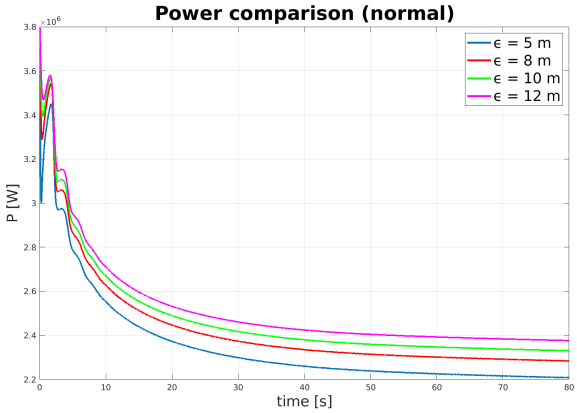

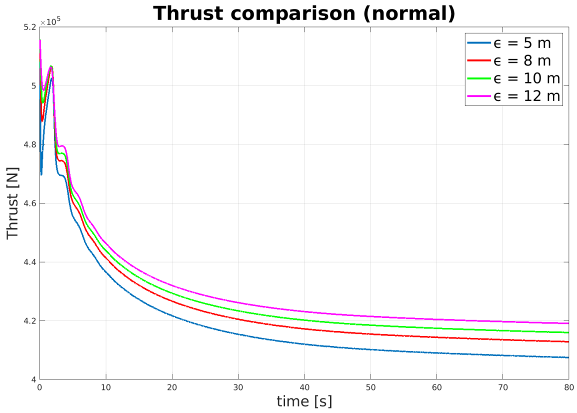

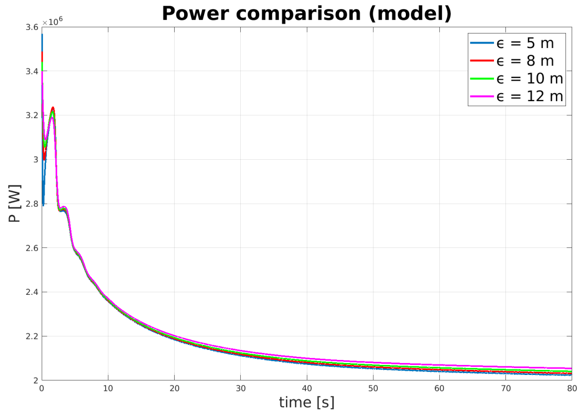

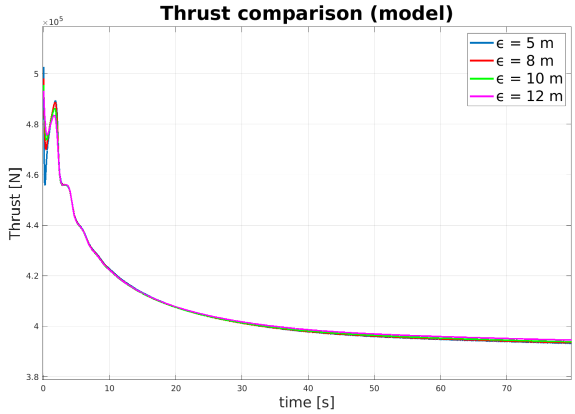

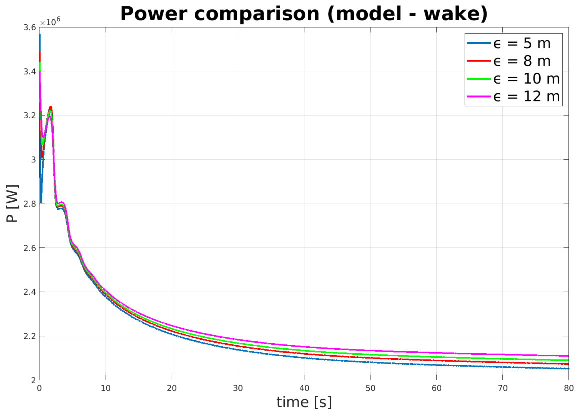

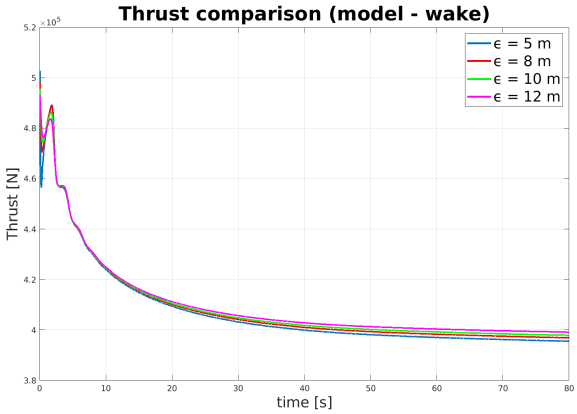

As can be clearly observed from a qualitative point of view in the charts, the total power and the total thrust with the standard version of SOWFA are extremely dependent from the value of the gaussian projection function width. As already explained this is due to a wrong representation of the shed vorticities along the blades when an ϵ value different from the optimal one is used. This causes an overestimation both of the power and of the thrust. When the model is applied instead the dependence on the ϵ value decreases a lot. For the first option of the implementation the dependence seems to almost cancel out. For the second option, instead,the dependence increases again a little bit, but for sure it remains extremely limited with respect to the standard version of SOWFA. Moreover, as already mentioned in chapter 4, the second option is very useful when there is the need to simulate more than one machine at the same time. In this case in fact it is very important to consider the effect of the model on the flow, because it influences the conditions at the inlet of the turbines behind the first one.

In order to highlight the fact that with a too high ϵ value the actuator line method overestimates the performances, a comparison of the power and the thrust between the standard version of SOWFA and the one with the model implemented was performed and the charts are reported here below. Only the first option for the implementation of the model was considered and the ϵ value chosen for the comparison was 12 m. This choice is based on the fact that, among the four ϵ values tested, 12 m is the one that brings to the most intense correction. In fact the higher is the difference between the actual projection function width value and the optimal one, the higher is the value of the correction and the more the standard performances are overestimated.

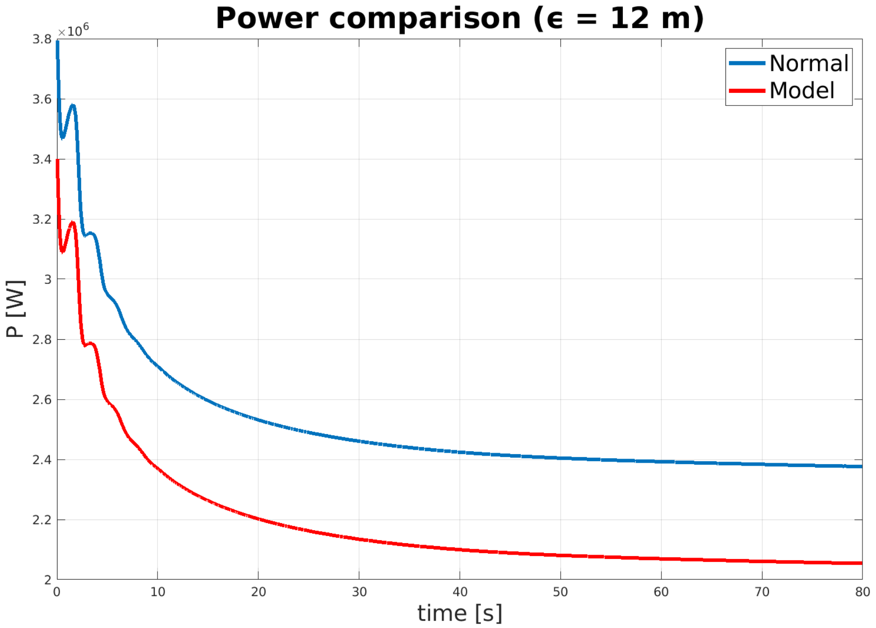
Power comparison (ϵ = 12 m)

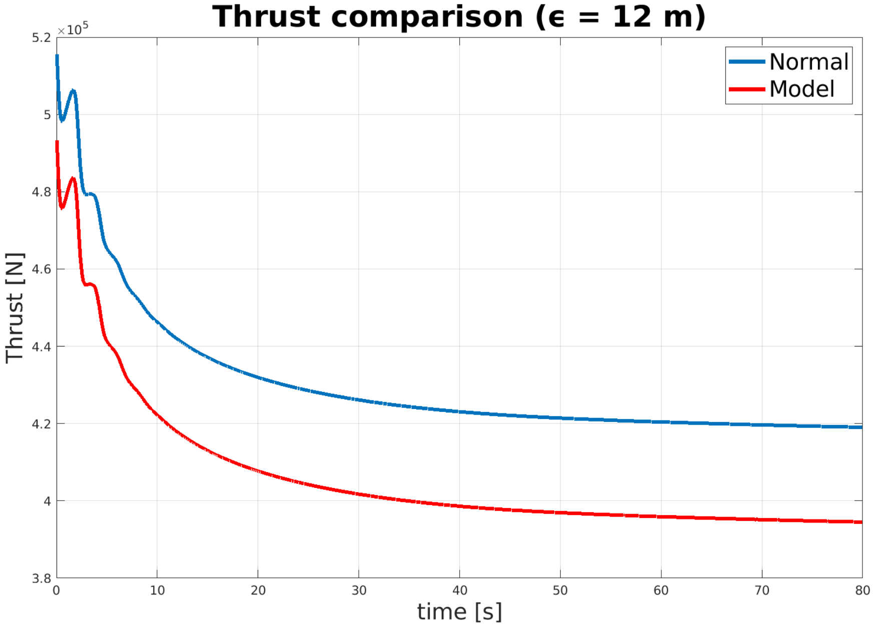
Thrust comparison (ϵ = 12 m)

From the two figures it is possible to note the way in which the correction acts. Both the power and the thrust in fact are decreased: the real effect of the vortices is recovered.

Finally, in the two tables below some quantitative values for the power and the thrust are reported. The first one contains their absolute values, whereas in the second one the percentage difference with respect to the case with an ϵ value equal to 5 m is present. This was done in order to understand once again the effectiveness of the model in decreasing the ϵ-dependence.

	POWER (NORMAL)	POWER (MODEL 1^{st} option)	POWER (MODEL 2^{nd} option)	THRUST (NORMAL)	THRUST (MODEL 1^{st} option)	THRUST (MODEL 2^{nd} option)
$\epsilon = 5$ m	$2.23 \cdot 10^6$ W	$2.04{\cdot}10^6$W	$2.07{\cdot}10^6$W	$4.09 \cdot 10^5$ N	$3.95{\cdot}10^5$N	$3.97{\cdot}10^5$N
$\epsilon = 8$ m	$2.31 \cdot 10^6$ W	$2.05{\cdot}10^6$W	$2.09{\cdot}10^6$W	$4.15 \cdot 10^5$ N	$3.95{\cdot}10^5$N	$3.97{\cdot}10^5$N
$\epsilon = 10$ m	$2.35 \cdot 10^6$ W	$2.06{\cdot}10^6$W	$2.11{\cdot}10^6$W	$4.18 \cdot 10^5$ N	$3.96{\cdot}10^5$N	$3.99{\cdot}10^5$N
$\epsilon = 12$ m	$2.40 \cdot 10^6$ W	$2.07{\cdot}10^6$W	$2.13{\cdot}10^6$W	$4.21 \cdot 10^5$ N	$3.96{\cdot}10^5$N	$4.01{\cdot}10^5$N

Table 6.1. Mean absolute values of the total power and the total thrust

	POWER (NORMAL)	POWER (MODEL 1^{st} option)	POWER (MODEL 2^{nd} option)	THRUST (NORMAL)	THRUST (MODEL 1^{st} option)	THRUST (MODEL 2^{nd} option)
$\epsilon = 5$ m	-	-	-	-	-	-
$\epsilon = 8$ m	3.4 %	0.38 %	0.98 %	1.30 %	0.046 %	0.32 %
$\epsilon = 10$ m	5.45 %	0.79 %	1.74 %	2.05 %	0.12 %	0.55 %
$\epsilon = 12$ m	7.49 %	1.41 %	2.64 %	2.78 %	0.28 %	0.84 %

Table 6.2. Percentage difference with respect to the $\epsilon = 5$ m case

6.1.2 Local quantities spanwise evolution

As already explained, the model acts by adding a component to the incoming velocity, perpendicular to it. This causes a reduction of the angle of attack that brings to a reduction of the lift coefficient and so also of the lift force. The latter is the main responsible of the final performance of the machine. The trend of the lift coefficient and of the lift force are reported in the charts below for the standard version of SOWFA and for the one with the two options of the model implemented. Once again only the results with the most refined mesh are considered.

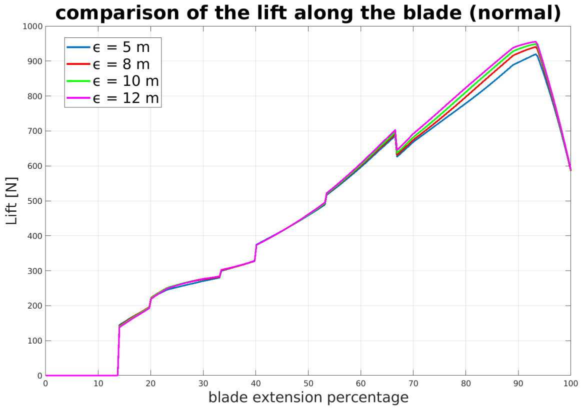

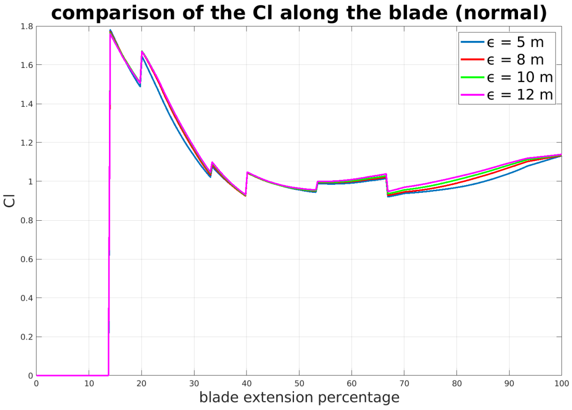

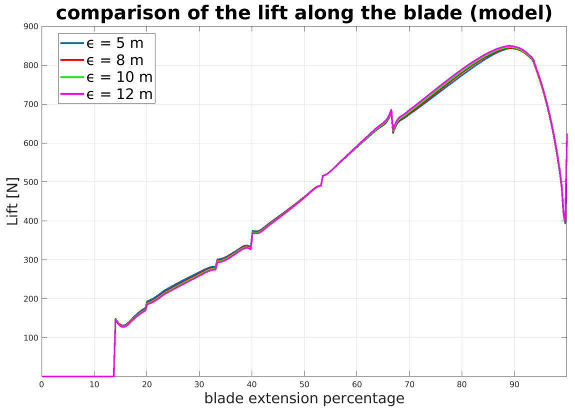

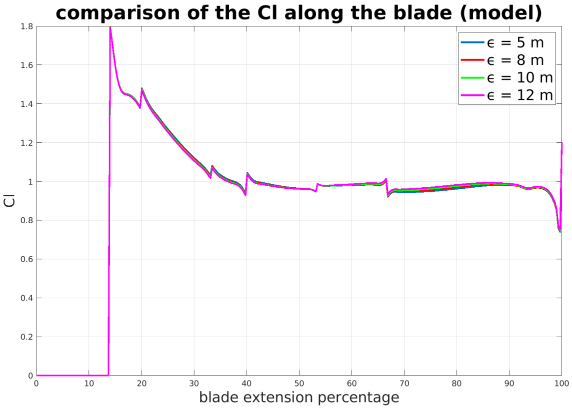

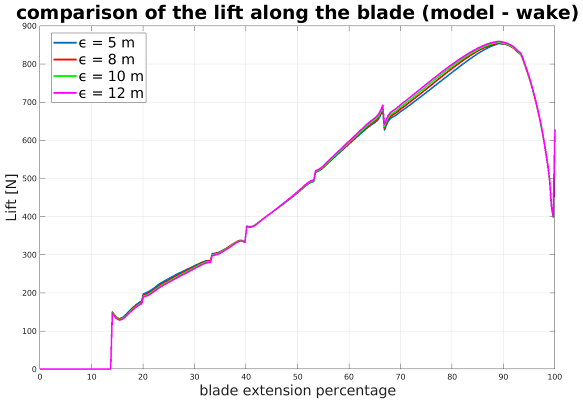

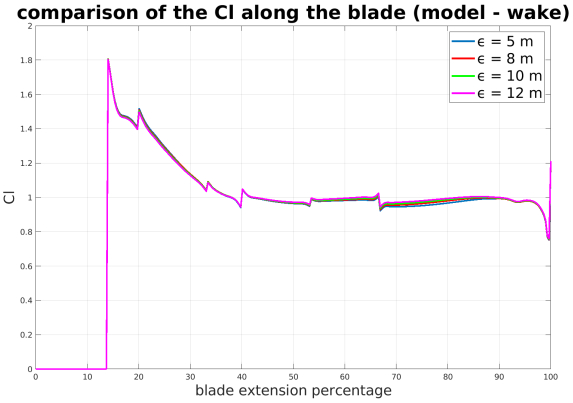

By looking at the spanwise distribution of these two local quantities it is possible to note once again how the dependence from the gaussian projection function width changes. Considering in fact the standard version of SOWFA, the four different curves, each representing a certain ϵ value, can be clearly distinguished, for both the lift force and the lift coefficient. When instead the model is applied, with both the first and the second option, the curves are much closer one each other. This means a strong reduction of the ϵ-dependence. Moreover, it is easy to note how the shape of the curves changes too. This happens especially in the tip zone, where the effect of the vortices (and so also of the correction) is the strongest. The tip zone is in fact also the zone where the highest ϵ-dependence is observed when considering the standard version of SOWFA.

As already done for the thrust and the power, here below two charts showing the comparison between the standard version of SOWFA and the first option of the model are reported. The aim is to allow a better comprehension of the way in which the correction works in order to highlight which are the zones more affected by it.

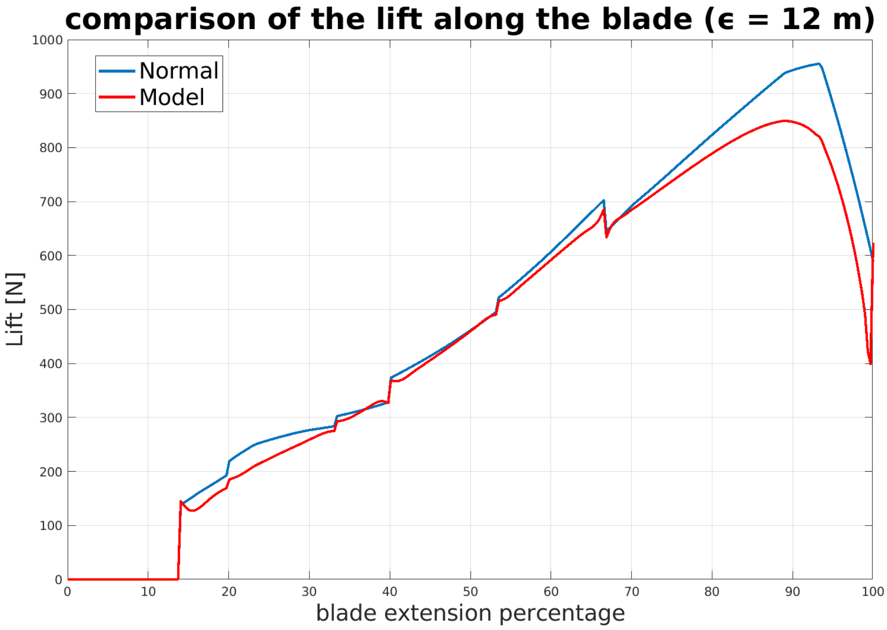

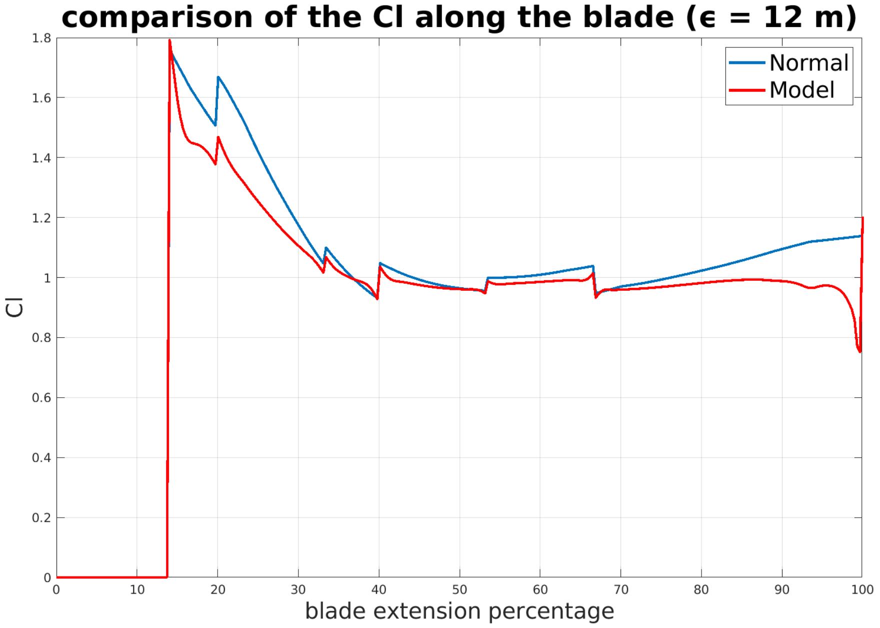

The zone in which the influence of the model is the highest is for sure the tip one. In this zone in fact, as already explained in chapter 4, the real turbines are highly affected by the downwash phenomenon caused by the presence of the tip vortices, generated by the difference in pressure between the two sides of the blade. The central zone instead is the one that is less affected by the correction introduced by the model. This zone in fact also in reality is little affected by the presence of the shed vorticity and for this reason the lift force and the lift coefficient are almost the same when considering the standard version of SOWFA and the one with the model implemented. Finally in the root zone (the one near the turbine rotor center) the influence of the model increases again. This is due to the presence of the root vortices that cause in

reality a decrease in the angle of attack in correspondence of the blade.
The correction applied can be fully characterized by the magnitude of the vector that is added to the incoming velocity (and that is perpendicular to it) and the difference between the initial angle of attack and the corrected one. These two quantities are plotted in the two charts below and the dependence from the gaussian projection function width is clearly highlighted.

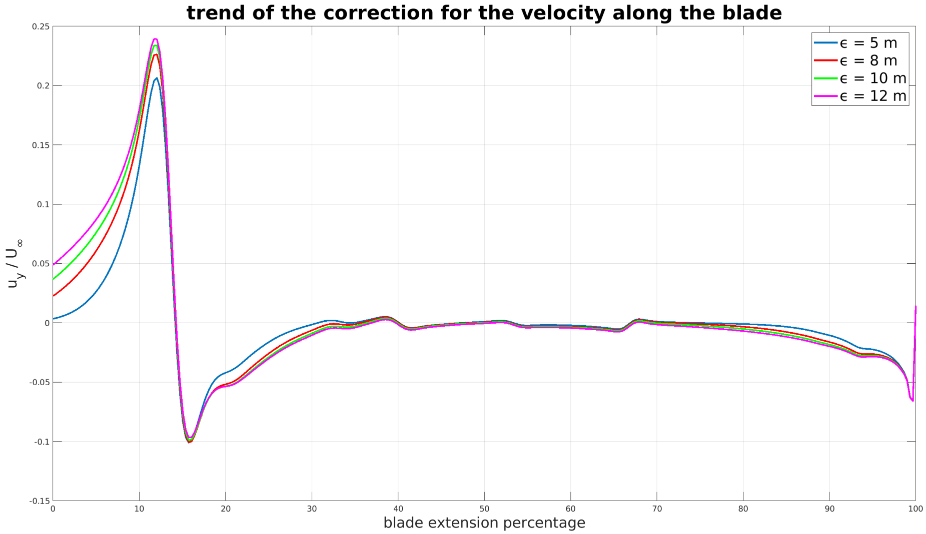

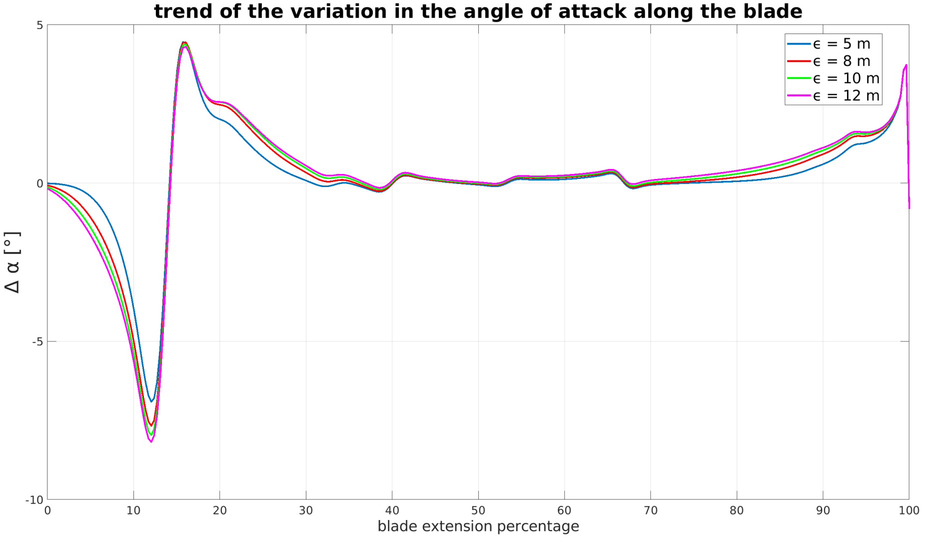

In both the charts it is possible to note a strange and unphysical behaviour in the first part of the blade. However, this zone is characterized by the presence of the cylinder (as can be read in table 5.6). This means that the lift is always zero and that the variation in the angle of attack does not influence the final performance of the machine. For what regards instead the rest of the blade, it is clearly visible that the two most affected zones are the tip zone and the root zone. Here in fact both the magnitude of the correction and the difference between the initial and the corrected angle of attack increase. In the central zone instead, so the one less influenced by the shed vorticities, the correction remains always zero. The same thing obviously happens for the variation of the angle of attack. Another important aspect that is at the basis of this thesis work and that thanks to these two charts can be easily observed is the way in which the correction varies by changing the ϵ value. The more the value of the projection function width increases, the more the conditions in which the simulations are performed are far from the optimal ones and the stronger needs to be the correction. This happens in order to try to always recover the results that can be obtained by using the optimal ϵ value.

6.1.3 Effect of the grid refinement level on the final results

In order to complete the analysis of the results obtained by performing simulations on the NREL 5 MW wind turbine, this final section will be dedicated to the effect of the grid refinement on the performances of the simulated machine. As already explained, two different grid refinement levels were considered. Until now only the results related to the most refined mesh have been shown. Here below, some charts representing the power, the thrust and the lift force of the machine with a mesh characterized by the first level of refinement are reported. For what regards the model, only the results related to the first option are shown.

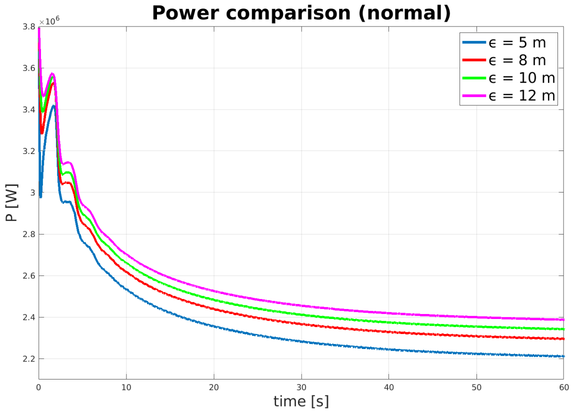

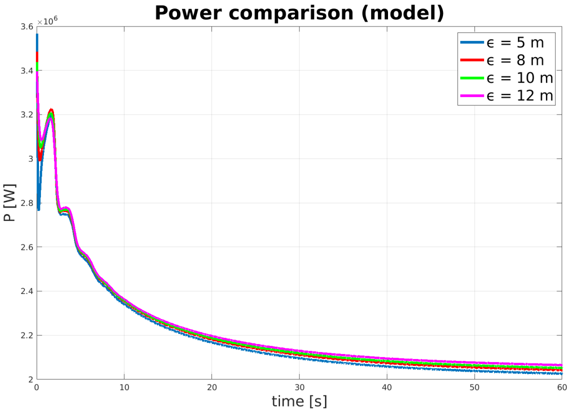

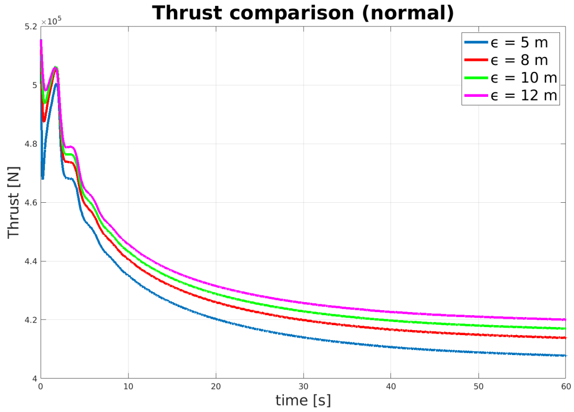

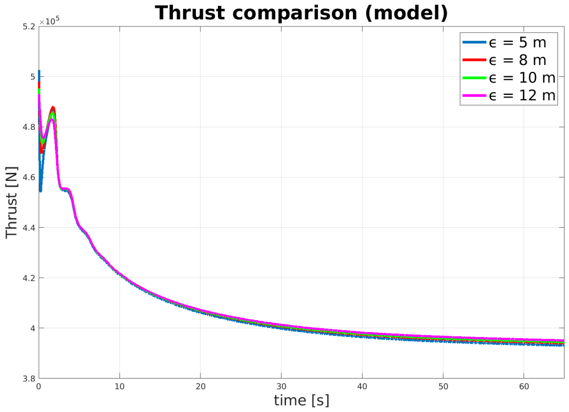

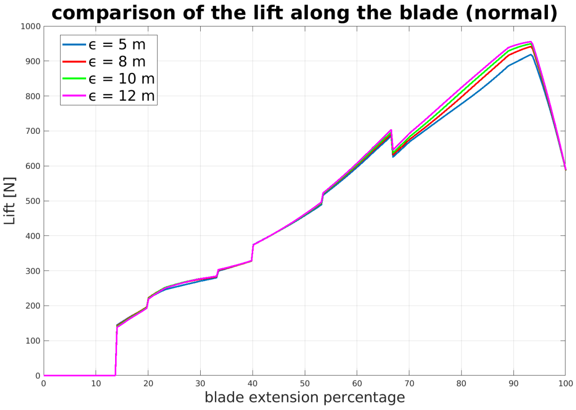

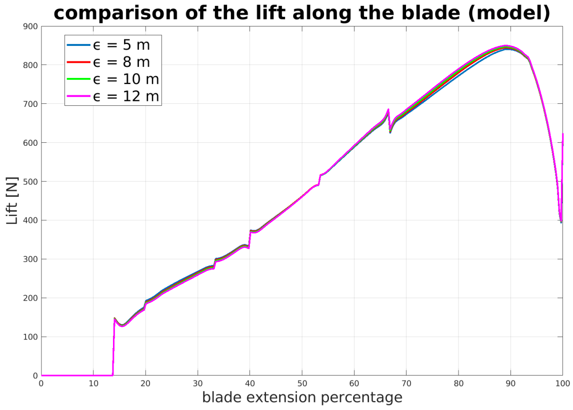

By looking at the charts it is possible to note how the model is effective also with a lower grid refinement level. The ϵ-dependence in fact decreases a lot when passing from the standard version of SOWFA to the one with the model implemented and the values of power, thrust and lift reached are decreased thanks to the application of the correction to the incoming flow. As already explained, in fact, the model must always work well, regardless of the grid refinement level.

At this point, a comparison between the results obtained by the two meshes considering the same ϵ value can be useful in order to understand which is the effect of the mesh on the final outputs. For this reason, the following charts contain a comparison between the two levels of refinement of the power and the thrust trend in time for both the standard version of SOWFA and the model. The two extreme ϵ values are considered: 5 m and 12 m. Once again, only the first option of the model is shown.

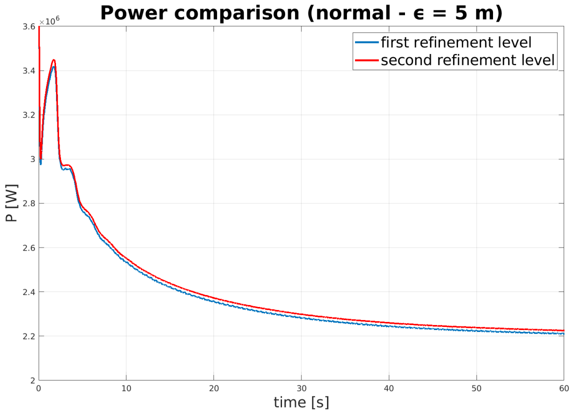

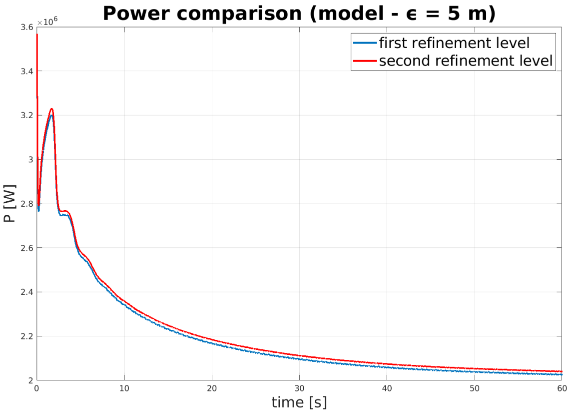

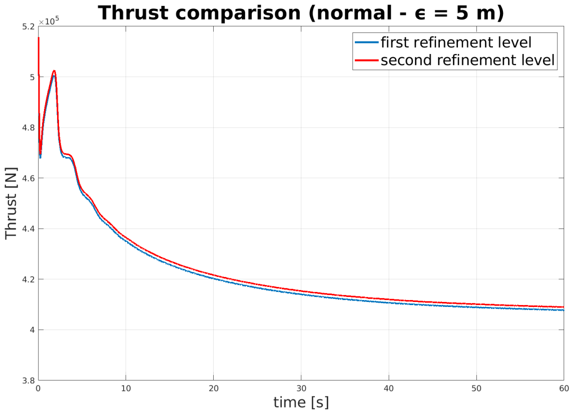
Thrust comparison (normal - ϵ = 5 m)

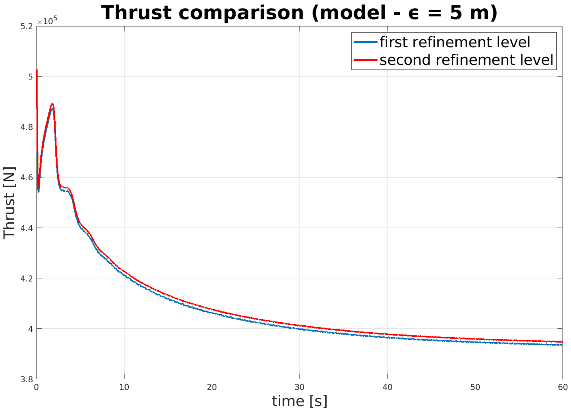
Thrust comparison (model - ϵ = 5 m)

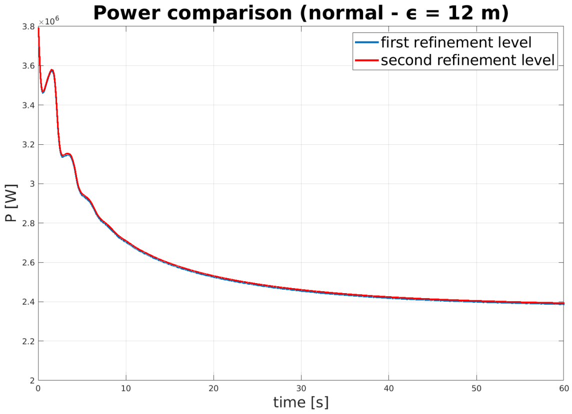
Power comparison (normal - ϵ = 12 m)

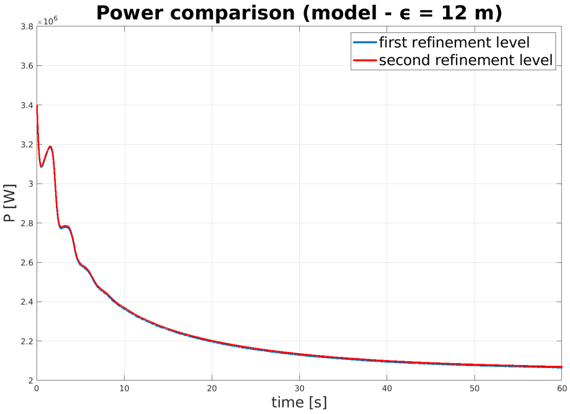
Power comparison (model - ϵ = 12 m)

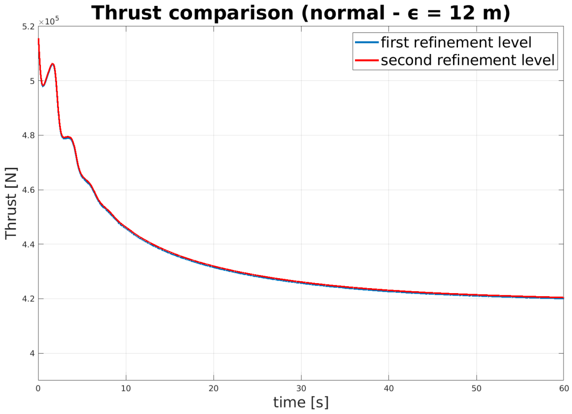
Thrust comparison (normal - ϵ = 12 m)

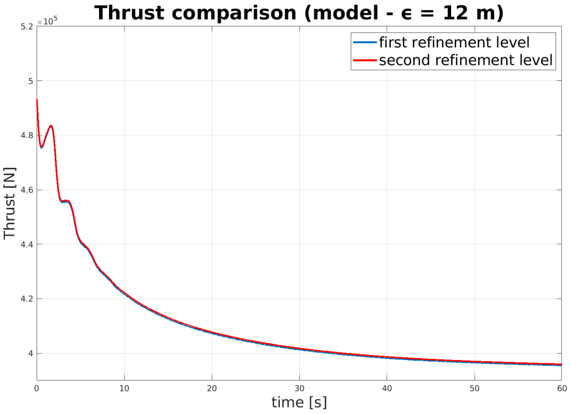
Thrust comparison (model - ϵ = 12 m)

The first thing that can be noticed by looking at the charts is the fact that the difference in the results between the two levels of refinement is very limited. This could be due to the fact that the number of cells along the rotor diameter is quite huge, already with the coarse mesh. 64 cells are probably sufficient to reconstruct in a precise way what happens along the rotor blades. An increase of the local refinement is able to lead only to limited improvements.
Another interesting aspect that can be highlighted is the fact that the results with an ϵ value of 5 m are affected (even if in a limited way) by the level of refinement of the grid. By looking instead at the power and the thrust with $\epsilon = 12m$, the dependence seems to cancel out. So, apparently, the grid dependence decreases with an increase of the gaussian projection function width. This phenomenon was observed also by Martinez, Churchfield and Leonardi in [35]. They stated in fact that the power production is

more grid dependent for smaller values of ϵ. Moreover they set a condition for the grid resolution: if $\Delta x < \epsilon/5$ the grid independence appears to occur (or at least the variation in the results is extremely limited). Considering the case with $\epsilon = 12m$, in fact, this condition is respected (the cell dimension in the rotor zone for the two meshes is respectively 1.5 m and 2 m) and in the four last charts no variations in the results are observed by changing the grid refinement level.

Hence, in conclusion, some considerations about the application of the model to meshes with different refinement levels can be made. As expected, the model works in the right way with both the meshes. In fact it must be able to correct the incoming flow field whatever is the level of refinement of the mesh. However, for what it is possible to understand by the graphs, the model is not able to act on the grid dependence. By comparing in fact the results with the standard version of SOWFA and the one with the model implemented, the way in which the level of refinement influences them seems to be the same.

6.2 DTU 10 MW wind turbine

6.2.1 Global quantities time history

As for the previous case the global quantities chosen in order to observe their time history are the rotor power and the rotor thrust. In the following graphs the results considering the standard version of SOWFA, the one with the first option of the model implemented and the one that takes into account the second option are reported. For now, only the mesh characterized by the first level of refinement and a number of actuator points equal to 300 are considered.

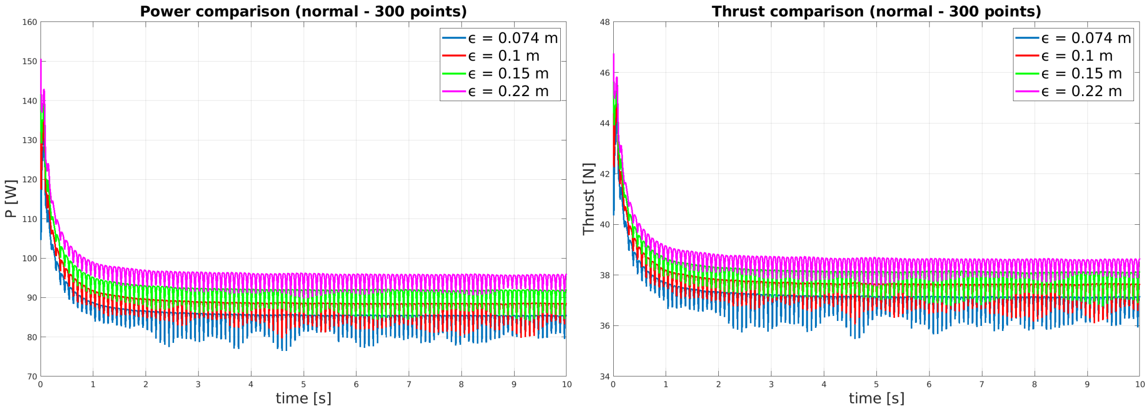

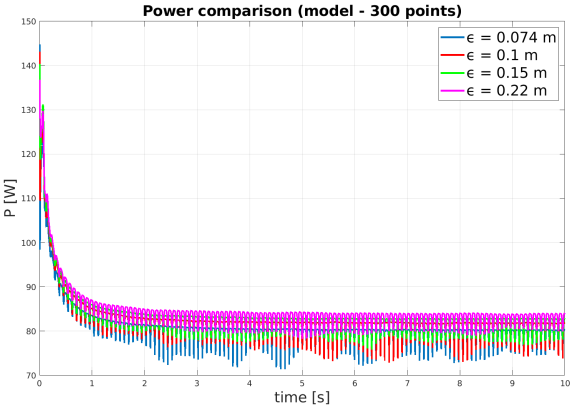

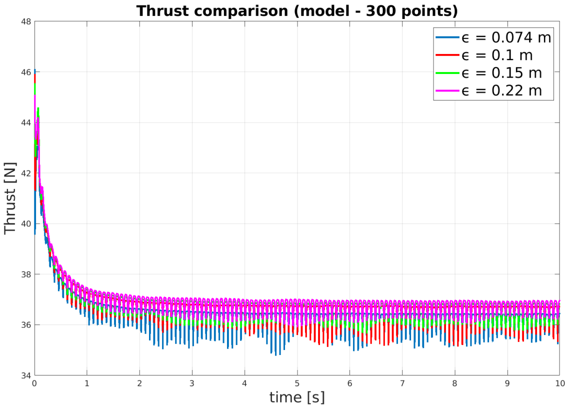

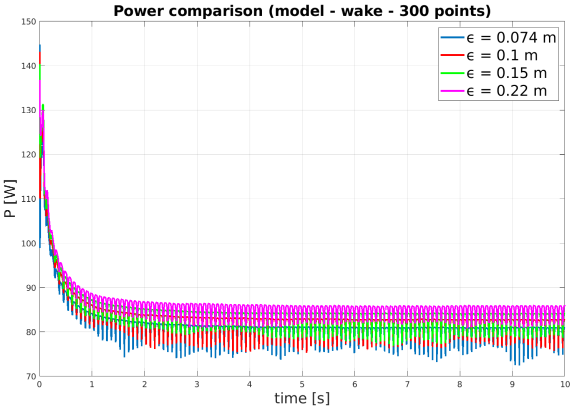

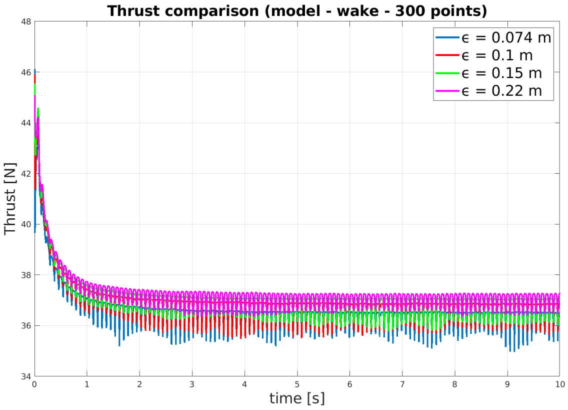

The first aspect that is clearly visible in the graphs and that differs from the case of the NREL 5 MW reference wind turbine is the presence of oscillations in the results (both for the power and the thrust). However, they are not an indication that the simulations performed were unstable. These oscillations are not spurious, but are simply caused by the presence of the tower. Each oscillation in fact represents the passage of each single blade in front of it.

For what regards instead the dependence from the value of the gaussian projection function width, the same trend observed in the previous case can be recognizable also for the DTU 10 MW wind turbine. By looking at the charts, in fact, it is possible to note how big is the ϵ-dependence when considering the standard version of SOWFA. Instead, when the correction to the incoming velocity is introduced, the dependence decreases a lot and the curves (for both the power and the thrust) become much closer one each other. This happens for both the first and the second option.

Another important aspect, already highlighted for the previous case, is the overestimation of both the power and the thrust when using the standard version of SOWFA. This can be clearly observed in the two following graphs that show the comparison between the results from the standard version of SOWFA and the ones coming from the first option of the model. Only the highest value for the gaussian projection function width (equal to 0.22 m) is considered.

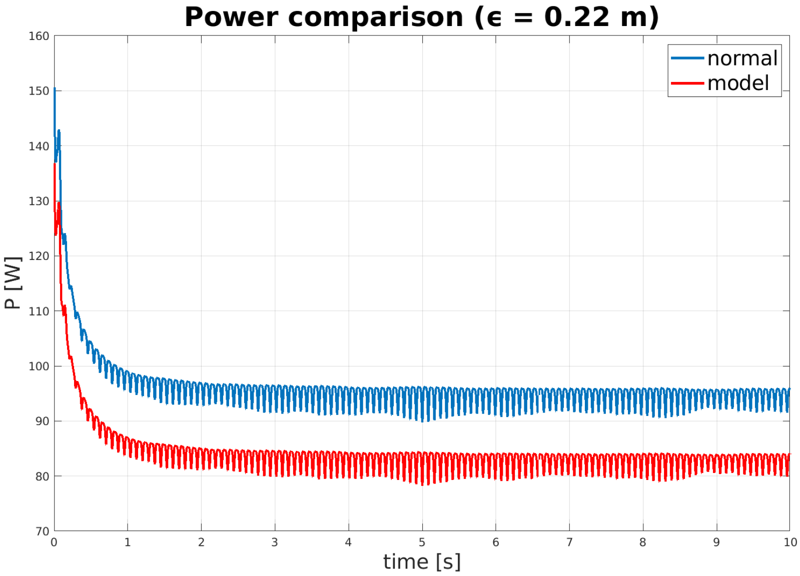

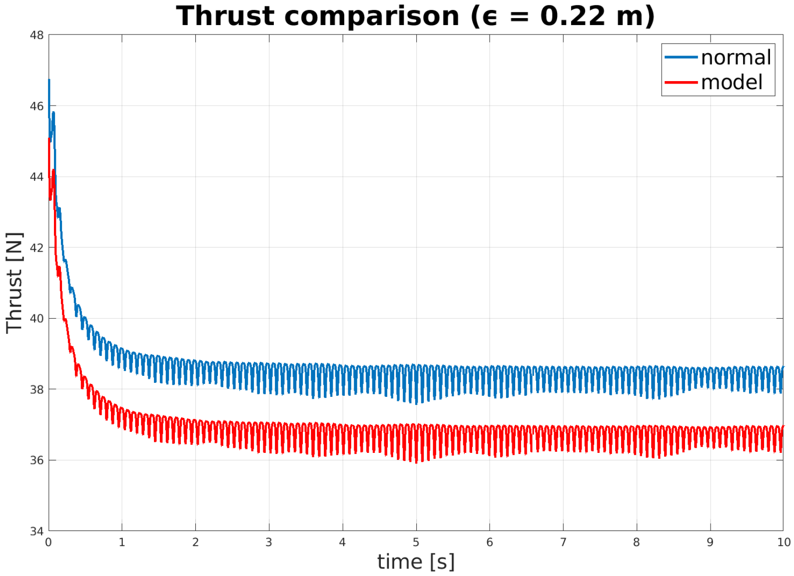

In the tables below instead some quantitative values are reported. The first one contains the absolute values of the power and the thrust for the standard version of SOWFA and the model with both the options. In the second one the percentage difference with respect to the case with $\epsilon = 0.074$ m can be found.

	POWER (NORMAL)	POWER (MODEL 1^{st} option)	POWER (MODEL 2^{nd} option)	THRUST (NORMAL)	THRUST (MODEL 1^{st} option)	THRUST (MODEL 2^{nd} option)
$\epsilon = 0.074$ m	84.54 W	79.42 W	80.11 W	36.96 N	36.26 N	36.36 N
$\epsilon = 0.10$ m	87.48 W	80.87 W	81.83 W	37.45 N	36.53 N	36.68 N
$\epsilon = 0.15$ m	90.74 W	81.81 W	83.10 W	37.90 N	36.65 N	36.86 N
$\epsilon = 0.22$ m	94.68 W	82.91 W	84.79 W	38.42 N	36.75 N	37.05 N

Table 6.3. Mean absolute values of the total power and the total thrust

	POWER (NORMAL)	POWER (MODEL 1^{st} option)	POWER (MODEL 2^{nd} option)	THRUST (NORMAL)	THRUST (MODEL 1^{st} option)	THRUST (MODEL 2^{nd} option)
$\epsilon = 0.074$ m	-	-	-	-	-	-
$\epsilon = 0.10$ m	3.47 %	1.84 %	2.14 %	1.32 %	0.75 %	0.88 %
$\epsilon = 0.15$ m	7.33 %	3.01 %	3.73 %	2.56 %	1.08 %	1.37 %
$\epsilon = 0.22$ m	11.96 %	4.39 %	5.84 %	3.95 %	1.35 %	1.91 %

Table 6.4. Percentage difference with respect to the $\epsilon = 0.074$ m case

By looking at the tables it is possible to note once again how the dependence from the gaussian projection function width decreases after the introduction of the model. As already said, this reduction is higher for the first option. This can be seen in the second table. However, the advantages reached thanks to the introduction of the second option of the model will be clearer when the analysis of the wake will be performed.
Finally, some results coming from the experimental tests performed in the wind tunnel are reported in the table below.

	POWER	THRUST
EXPERIMENTAL VALUES	83.79 W	35.91 N

Table 6.5. Power and thrust values from the experimental tests

By comparing it with the table 6.3 some comments can be made. First, by looking at the values of the power and the thrust coming from the standard version of SOWFA, it is possible to note that they are always overestimated and that the gap between the computed values and the experimentally measured ones increases with the increase of the gaussian projection function width. Considering now instead the results from the application of the model, it is possible to observe that with the first option the power seems to be a bit underestimated, whereas with the second one the power is a bit underestimated for almost all the ϵ values and a bit overestimated for the highest value. For what regards instead the thrust, considering both the options, it is always a bit overestimated. However, the values of the thrust obtained thanks to the introduction of the model remain much closer to the real thrust value with respect to the results coming from the standard version of SOWFA.

6.2.2 Local quantities spanwise evolution

As already done for the case of the NREL 5 MW wind turbine, this section is dedicated to the analysis of the evolution along the blade span of some local quantities. The local quantities chosen are the lift coefficient and the lift force. Here below their trend is reported for the standard version of SOWFA and the model with both the options applied. Only the mesh characterized by the first level of refinement and a number of actuator points equal to 300 are considered.

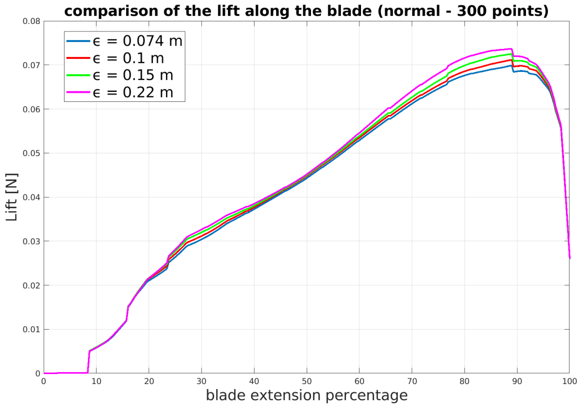

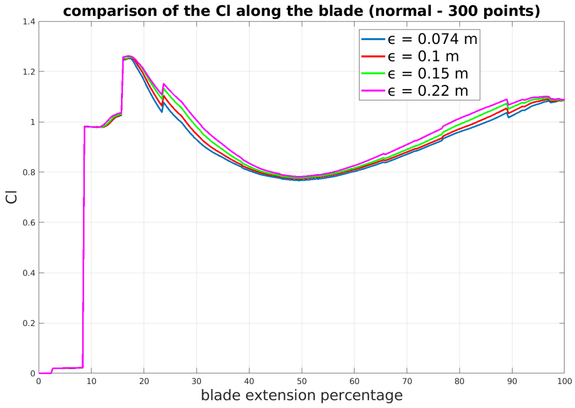

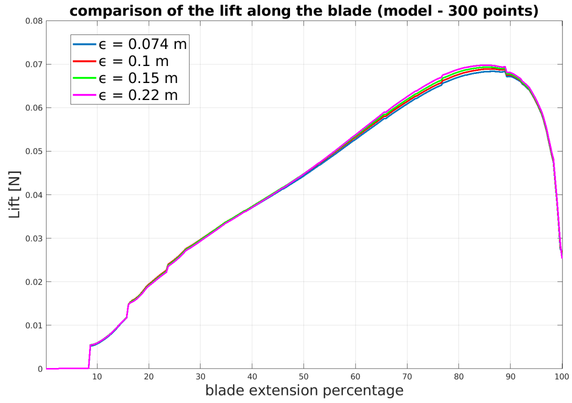

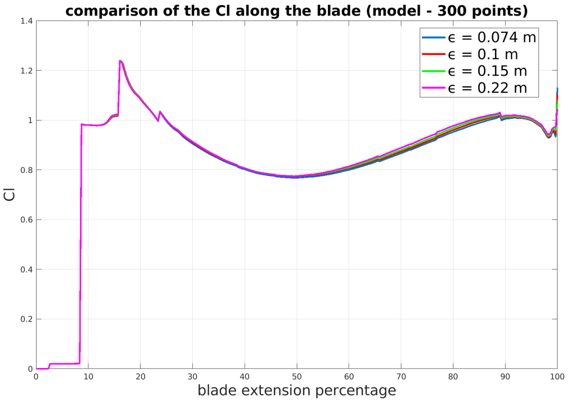

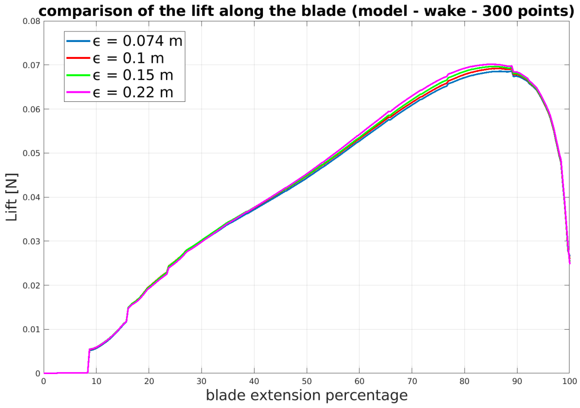

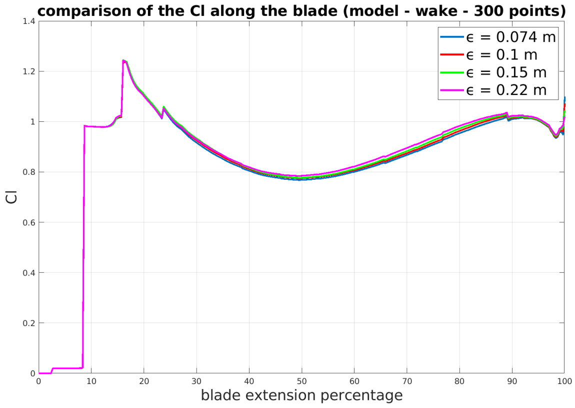

By looking at the spanwise distribution of these two local quantities, the effectiveness of the model is once again clearly visible. Considering the four values of the gaussian projection function width, in fact, it is possible to observe how the curves are much closer one each other when the model is applied both for the lift force and the lift coefficient. This happens for both the options for the implementation of the model. By putting the attention on the C_L spanwise distribution coming from the standard version of SOWFA the zones most dependent on the ϵ value are clearly visible. They are the zones near the root and the tip, that are also the ones most affected by the vortices in the reality. Therefore, in these two zones the intensity of the correction on the incoming velocity must be the highest.

In the two following graphs, representing the comparison between the results from the standard version of SOWFA and the ones coming from the application of the model, this aspect is even more evidenced.

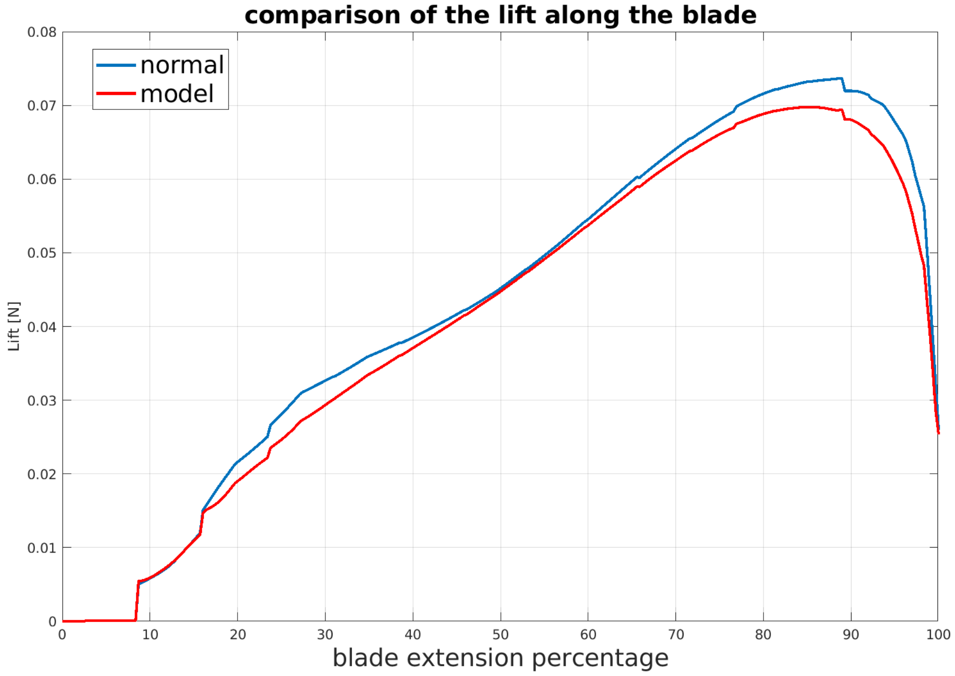

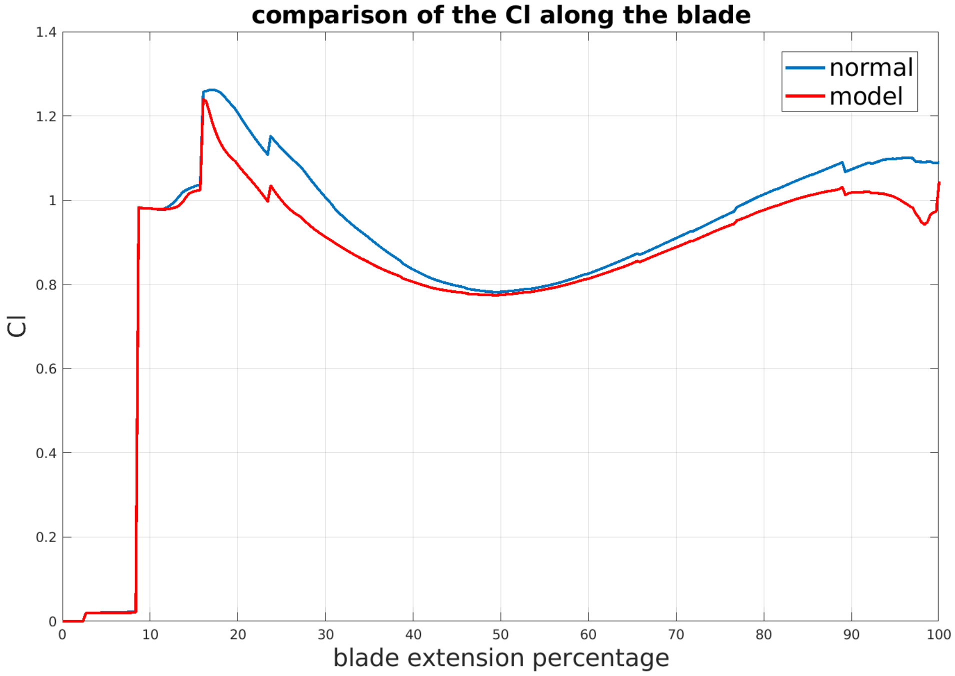

By looking at the charts, it is possible to note that in the central zone the curve related to the standard version of SOWFA and the one coming from the model are almost overlapped. In that zone in fact the effect of the shed vorticities is negligible and the intensity of the correction is almost null. In the root and the tip zone, instead, SOWFA in its normal version is not able to represent in a right way the effect of the vortices. The model acts in recovering the effect of the downwash phenomenon that

occurs in the reality. This causes a decrease of the lift coefficient (generated by a decrease of the angle of attack) that results in a decrease of the lift force along the blade.
In conclusion, as already done for the previous case, here below the trend of the correction along the blade span and the difference between the initial angle of attack and the corrected one are reported.

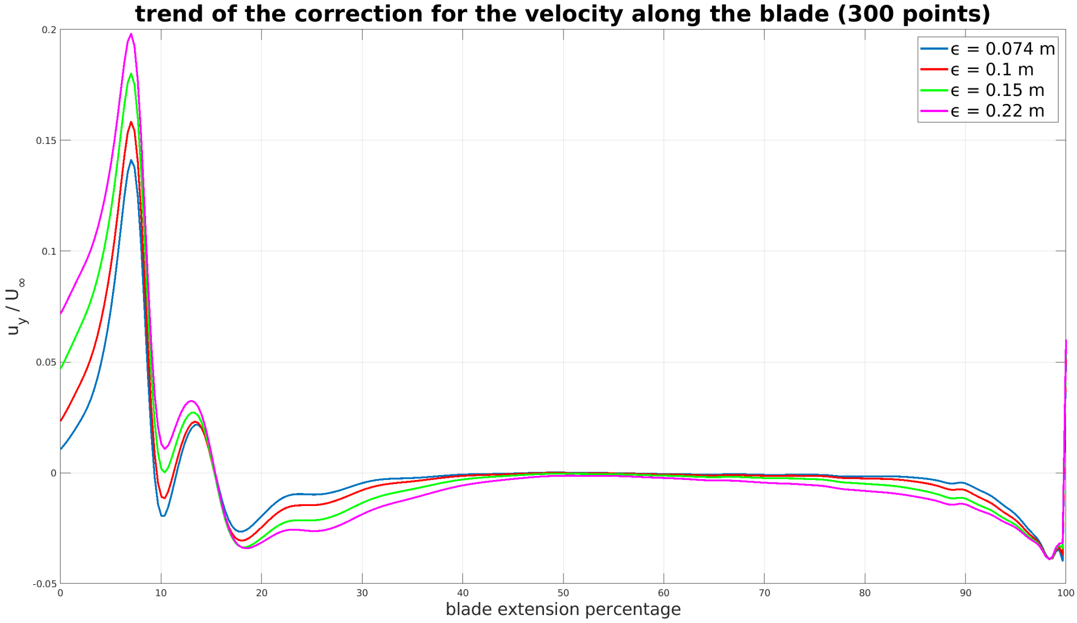

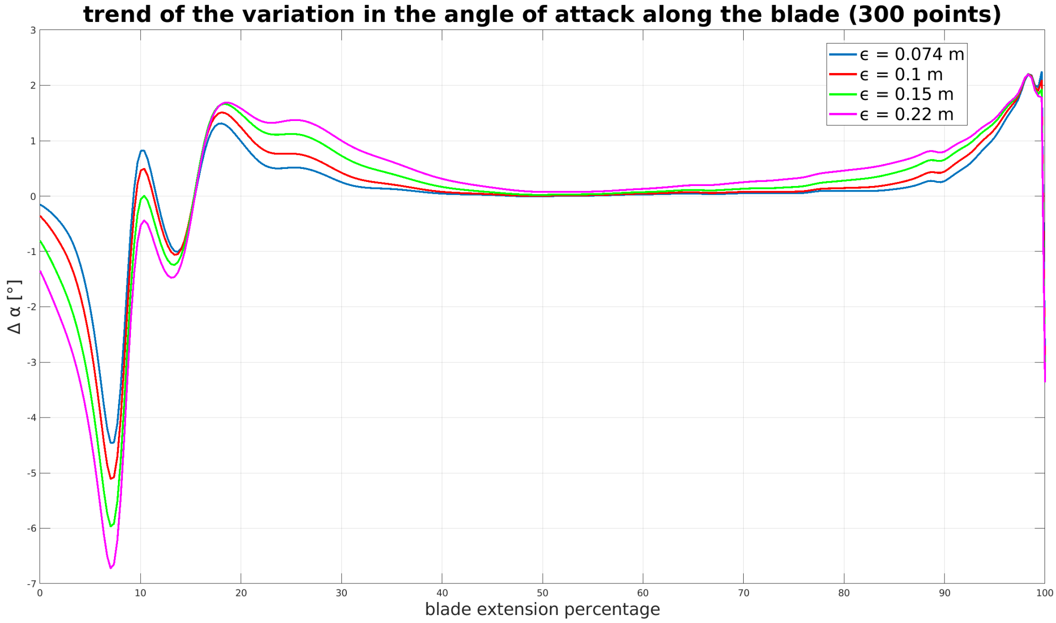

Thanks to these two charts what was previously mentioned can be even clearer. In the central zone, the one almost not affected by the effect of the vortices, the intensity of the correction is zero. Shifting towards the tip and the root zones, the intensity increases. As already mentioned several times, this is due to the fact that the stronger are the vortices the higher must be the intensity of the correction in order to recover the real effect of the downwash phenomenon upstream of the machine. Moreover the higher is the value of the gaussian projection function width the weaker is the effect of the represented vortices: the intensity of the correction must increase with the ϵ value.

6.2.3 Effect of the grid refinement level on the final results

As already mentioned, even if the model acts on the way in which the gaussian projection function width influences the results, another mesh characterized by a higher level of refinement was tested. The characteristics of the mesh can be found in table 5.7. In the charts below the obtained power, thrust and lift are shown. The results from the standard version of SOWFA and the ones from the implementation of the first option of the model are reported. Moreover only two ϵ values are considered: 0.1 m and 0.22 m.

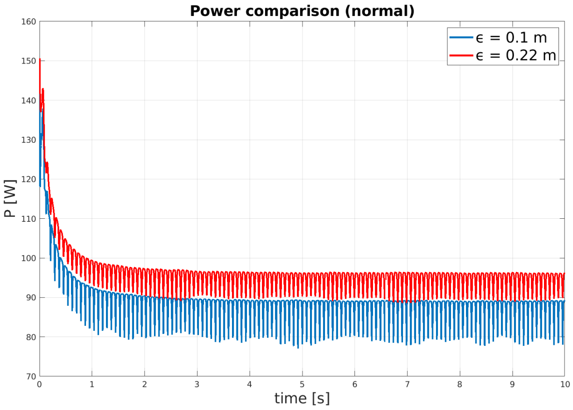

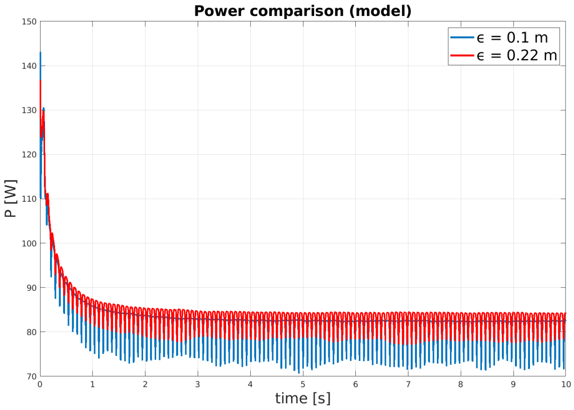

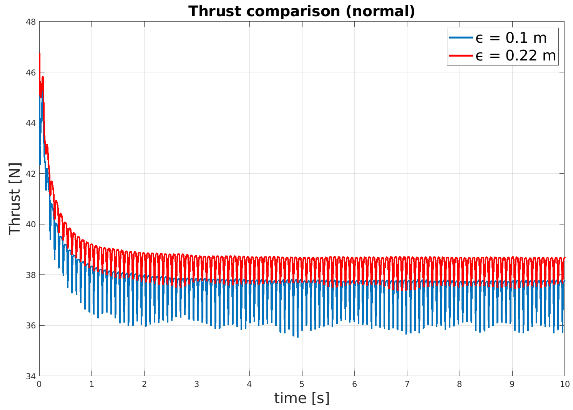

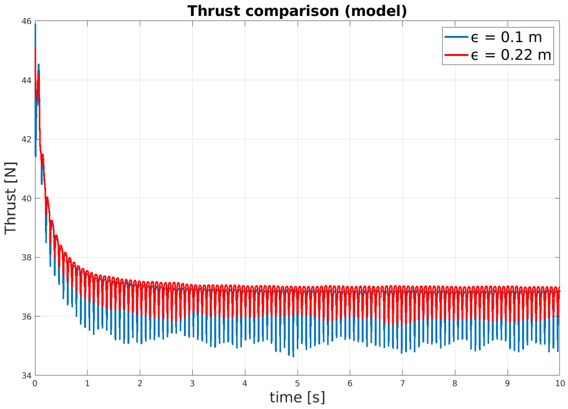

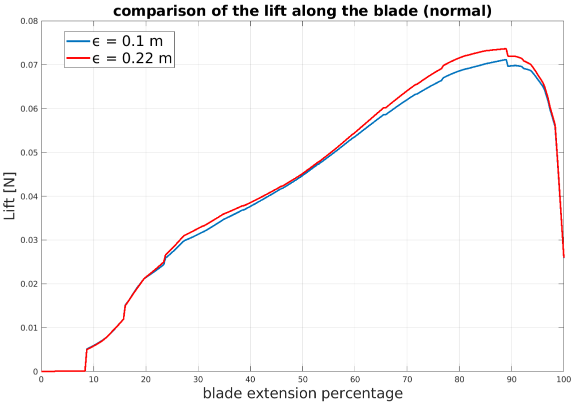
comparison of the lift along the blade (normal)

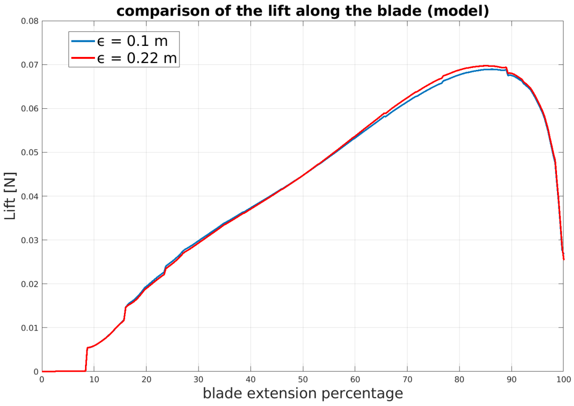
comparison of the lift along the blade (model)

By looking at the charts, the same behaviour already observed for the coarse mesh can be recognized again. Considering the case for which the model was introduced, in fact, the curves related to the two different ϵ values are much closer one each other with respect to the ones coming from the standard version of SOWFA. This is due to the application of the correction to the incoming flow, in order to recover the real effect of the shed vorticity. As already mentioned, the two zones in which the intensity of the correction is the highest are the root and the tip zone. This is clearly visible in the two last charts, representing the lift force distribution along the blade span, in which a quite high dependence from the value of the gaussian projection function width is present in these two zones when considering the standard version of SOWFA. This dependence is extremely reduced when the model is applied.

In the charts below, instead, a comparison between the two meshes is shown. Only the case with an ϵ value equal to 0.22 m is considered. Moreover only the first option of the model is shown.

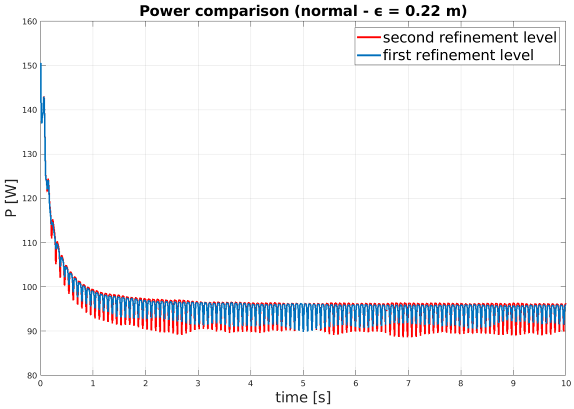
Power comparison (normal - ϵ = 0.22 m)

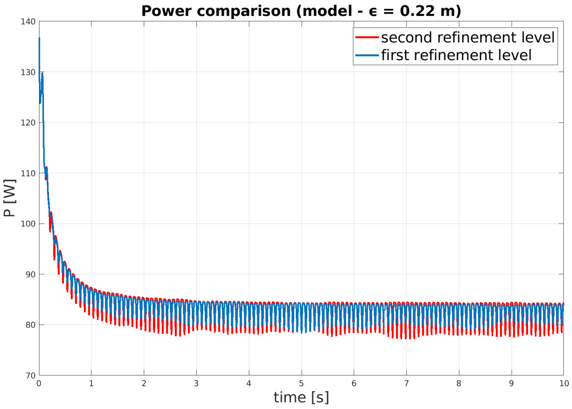
Power comparison (model - ϵ = 0.22 m)

The first aspect that can be easily noted is the fact that the value of the obtained power seems to be almost the same considering the two different levels of refinement. The only thing that varies considering a higher level of refinement is the amplitude of the oscillations that are caused by the passage of the blades in front of the tower. The variation of the mean value of the total power obtained, instead, can be assumed to be negligible. Moreover, as can be observed by comparing the two graphs, the application of the model seems to not have any influence on the effect that the grid refinement has on the final results. In fact, the relative position between the curves related to the two levels of refinement is exactly the same when considering the standard version of SOWFA and the case in which the model was applied. The same thing was already observed for the NREL 5 MW wind turbine case.

6.2.4 Effect of the number of actuator points on the final results

In this section an analysis of the effect that the number of actuator points chosen can have on the final results is contained. For doing this, the trend of some quantities (both global and local) considering 40 and 300 actuator points is compared. In the two charts below, for example, a comparison between the lift force blade span distributions with 40 and 300 actuator points resulting from SOWFA with the model implemented is shown. Only the first option for the implementation of the model is considered.

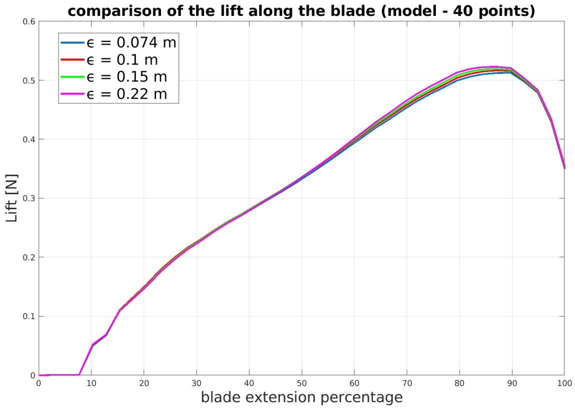

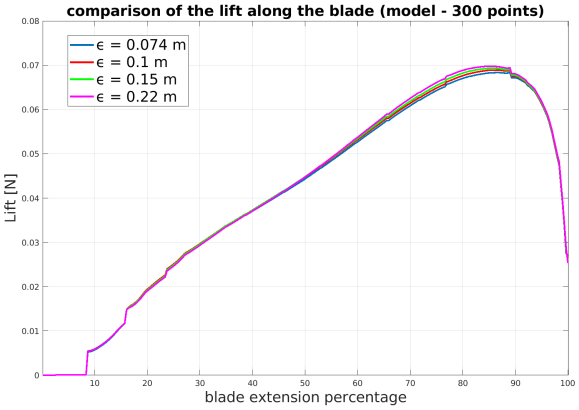

The first thing that is easily observable is the fact that the way in which the gaussian projection function width influences the computed performance of the machine does not change when considering 40 or 300 actuator points. The relative position among the curves, each related to a certain ϵ value, in fact, remains the same even when the number of actuator points varies. By looking instead at the shape of the lift force curve, it is possible to note that some differences arise. This happens especially in the tip zone. Here, in fact, the curve trend for 300 actuator points becomes much steeper than the one with 40 actuator points. This means that for the case on the right the tip losses (and so the reduction of the loads in correspondence of the tip blade as a consequence of the presence of the vortices) are more relevant than for the case on the left. This obviously affects also the computed global quantities characterizing the machine. In the chart below a comparison of the power when the model is applied for 40 and 300 actuator points is reported.

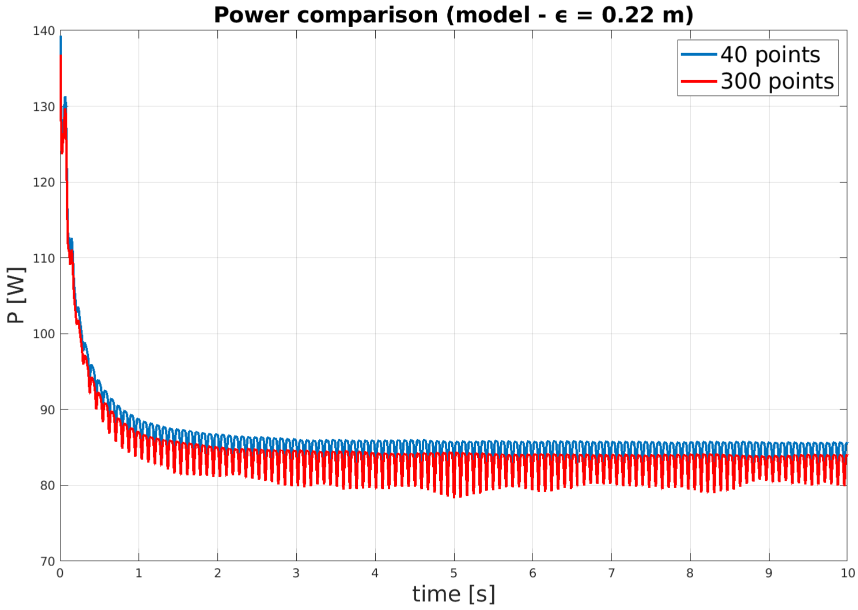

As is clearly visible, the power obtained with 300 actuator points is lower than the one with 40 actuator points. As just mentioned, this is due to the higher impact that the tip losses has on the final performance when considering the application of the model. By looking instead at the total power coming from the standard version of SOWFA (whose chart is reported here below) this is no more true.

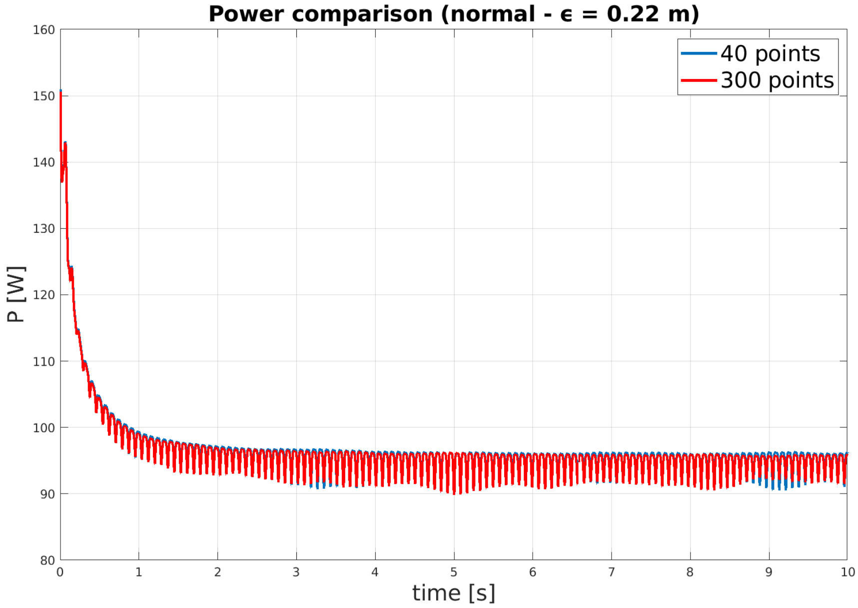

In this case in fact the curve related to the use of 40 actuator points and the one linked to 300 actuator points are overlapped. This means that, for the standard version of SOWFA, no improvements are reached by choosing a higher number of points. The loads along the blades are reconstructed in the same way and no variations are observed by comparing the two outputs. Hence, a higher number of actuator points is useful only when the model is introduced.

In order to better understand this aspect, another comparison that links the trend of the correction for the velocity along the blade for 40 and 300 points can be made. It is reported in the chart below.

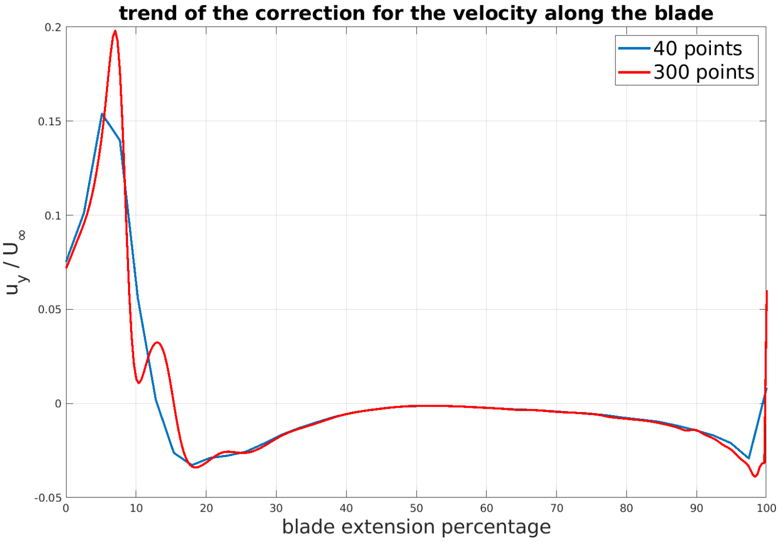

Without considering the first part near the root, where, as already said, a non physical trend is present (this zone is characterized by the presence of the cylinder, so the performances in this first part are not influenced by this strange trend), it is possible to observe that the two curves are almost overlapped for most of the blade length. The only zone in which a quite huge discrepancy between the two curves is visible is the one near the tip. Here in fact the effect of the vortices is the strongest and so the importance of the model increases. A higher number of actuator points allows to better reconstruct this effect and to recover the downwash phenomenon that occurs in reality.

Finally, in order to have a vision as complete as possible of the influence of the number of actuator points on the final results, also a comparison of the lift coefficient trends with both 40 and 300 points is reported.

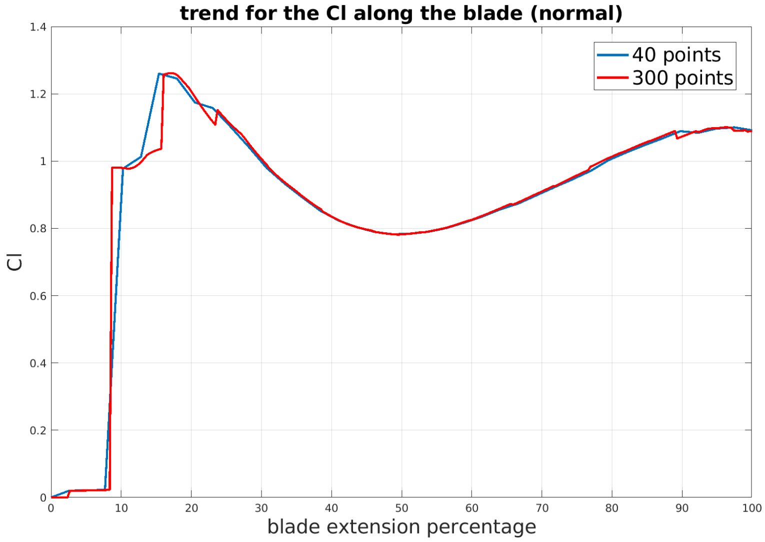

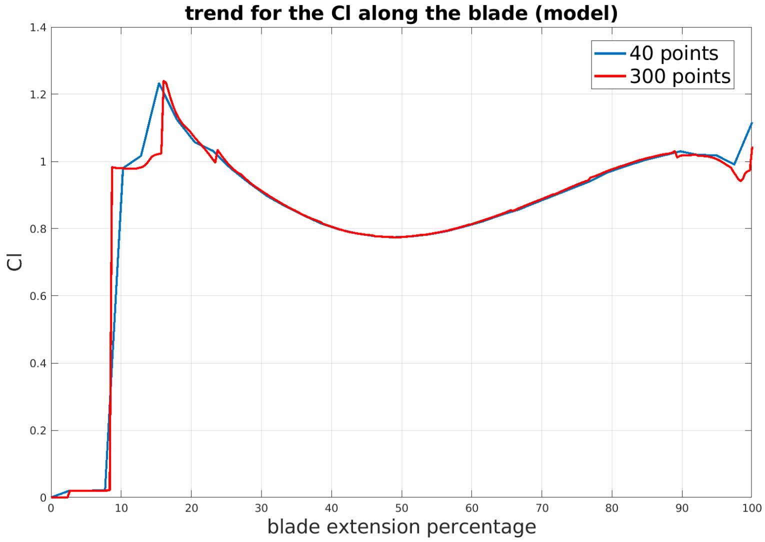

The first chart comes from the standard version of SOWFA, whereas the second one is linked to the implementation of the model. Once again, in the first chart the curves are almost overlapped along all the blade because no changes in the reconstructed blade loads are observed when using the two different numbers of points. For what regards instead the implementation of the model, the use of a higher number of points along the blade allows to reconstruct in a more precise way the effect of the vortices. As already mentioned, this happens especially in the tip zone where in the reality this effect is the strongest.
Hence, in conclusion, if one wants to apply the model to SOWFA in order to try to recover the real effect that the shed vortices have on the incoming flow field, the best choice is to use a number of actuator points higher than the usual one. This allows to apply in a very precise way the correction all along the blade, especially in the tip region. For what regards instead the standard version of SOWFA, the use of the usual number of points (equal about to 40) is the most sensible. In fact a higher number does not lead to any improvements in the final results.

6.2.5 Wake analysis

This is the last section related to the results coming from the simulations performed on the scaled version of the DTU 10 MW reference wind turbine. It is dedicated to the analysis of the wake that is generated behind the machine. The influence of the chosen gaussian projection function width on the turbulent structures that characterize the wake will be observed, the horizontal and the vertical axial velocity profiles, considering different ϵ values, will be studied and the effectiveness of the model applied will be analysed. Obviously only the second option for the implementation of the model in SOWFA will be considered. As already mentioned several times, in fact, only that one is able to influence the flow field around the machine. The first option instead acts only on the wind turbine performance, without affecting the flow field and the turbulent structures linked to it inside the computational domain.

First of all, in order to understand the weight that the choice of the ϵ value has on the turbulent structures that are generated after the passage through the machine, four images representing the intensity of the vorticity at a distance of 3 diameters behind the turbine are reported here below.

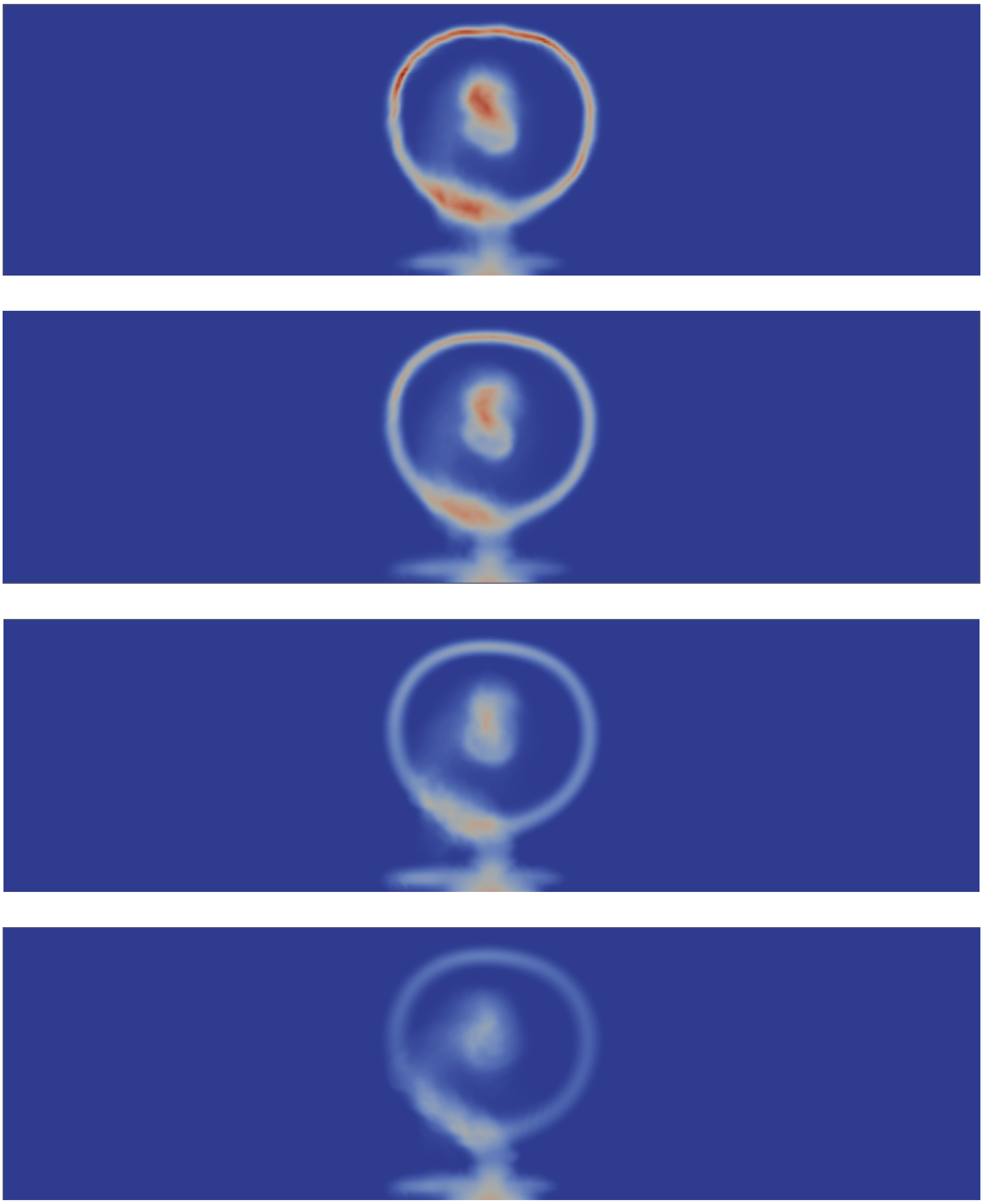

Figure 6.1. Vorticity intensity at a distance of 3D behind the machine considering $\epsilon = 0.074$ m, $\epsilon = 0.1$ m, $\epsilon = 0.15$ m, $\epsilon = 0.22$ m

From the first to the last image the value of the gaussian projection function width becomes higher and higher. As is clearly visible, the intensity of the vortices detaching from the machine becomes instead weaker and weaker. This is caused by the fact that

the use of a higher ϵ value means a wider zone in which the forces are projected. This can be translated in more diffused body forces, that generate more diffused (and so weaker) shed vortices. Also their effect on the flow field is obviously less intense and so the downwash phenomenon is underestimated with a too high ϵ value. This causes an underestimation of the induced drag, an overestimation of the angle of attack in correspondence of the blade and so the final performances of the machine (power, thrust, lift, etc.) are overestimated. As already said, this concept is at the basis of this thesis work and the introduction of the model has the aim of reaching results that can be independent of the choice of the ϵ value and as close as possible to the real performances.
The same phenomenon can be recognized by looking at the two following images:

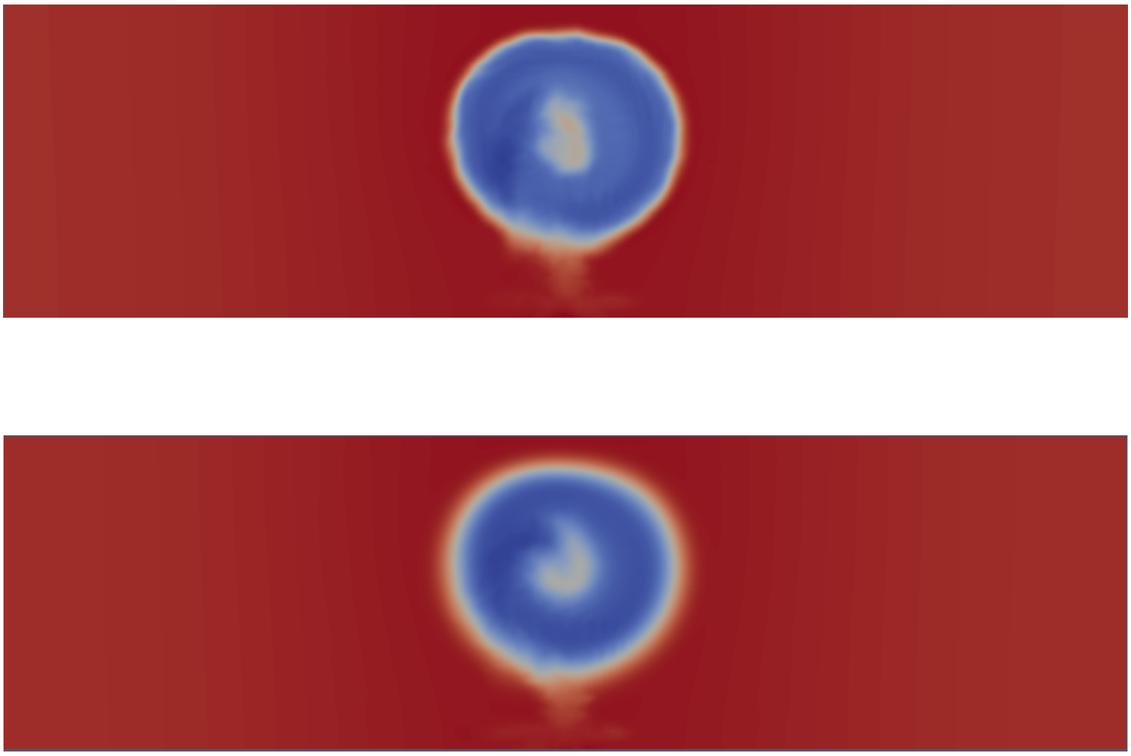

Figure 6.2. Cross section of the axial velocity distribution at a distance of 3D behind the machine considering $\epsilon = 0.074$m and $\epsilon = 0.22$ m

Also in this case it is possible to note how for the lowest ϵ value (the first image) the distribution of the axial velocity seems to be sharper and clearer. Instead, for the second image, the one related to a gaussian projection function width of 0.22 m, the distribution of the velocity seems to be much more diffused. Once again, this is due to the way in which the forces are projected into the computational domain. In the case of a low ϵ value, the zone influenced by the presence of the machine is more concentrated and so also the transversal region in which the incoming flow field is influenced is more easily recognizable. By increasing the gaussian projection function width the opposite phenomenon is observed: a more diffused zone influenced by the presence of the wind turbine causes a more diffused transversal region in which the incoming flow field feels it.

In order to highlight even more the big influence of the ϵ value on the performed simulations, also the turbulent kinetic energy can be analysed. In the chart below the turbulent kinetic energy function of the transversal dimension considering different values for the gaussian projection function width is shown. The distribution is related to a distance of 3 diameters behind the machine.

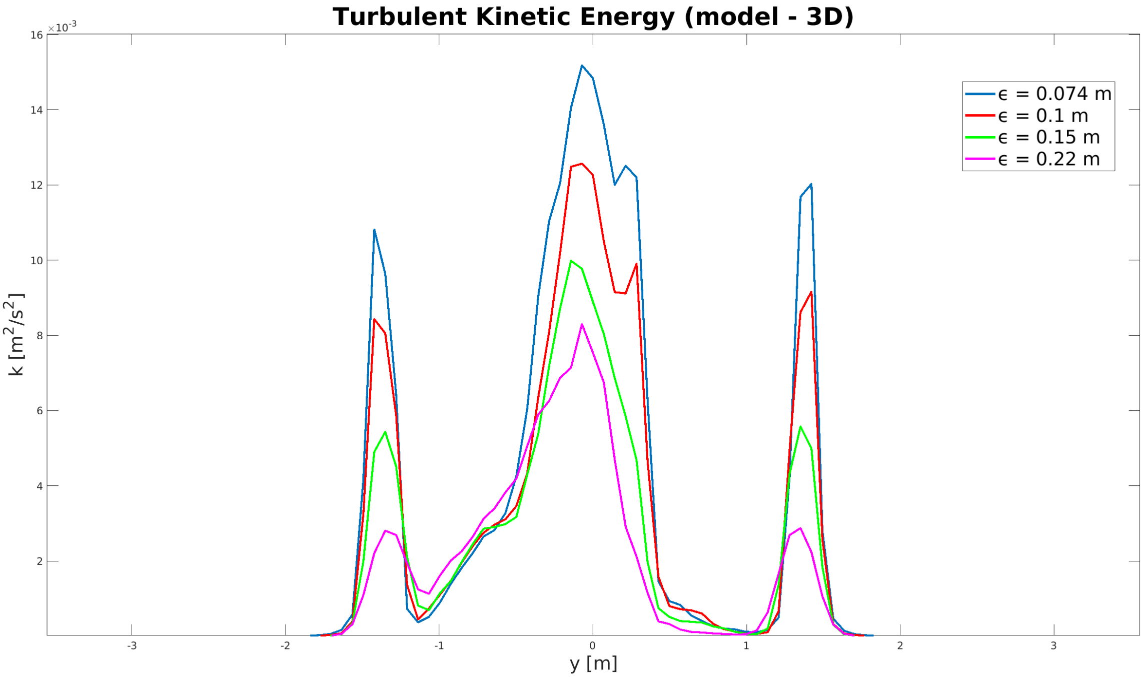

Figure 6.3. turbulent kinetic energy distribution in the transversal direction considering four different ϵ values

The turbulent kinetic energy is an appropriate subject to be studied if one is interested to the turbulent structures that are generated behind the machine. It is in fact an indicator of the turbulence level of the flow and so, obviously, also of the intensity of the vortices.

This is clearly visible in figure 6.3. It is possible to recognize the presence of the tip vortices (at the two extremities) and of the root vortices (in correspondence of y = 0 m). In these zones the level of the turbulent kinetic energy increases a lot, whereas in the others it is much lower. Moreover, it is possible to note that the highest level is reached for the lowest ϵ value. Once again this is due to the fact that a lower gaussian projection function width leads to more concentrated, sharpened and intense shed vortices. They cause a great increase of the turbulence level.

Another aspect that needs to be highlighted is that the chart refers to a simulation performed with the model implemented in SOWFA. The model in fact acts on the angle of attack and causes a variation of the exchanged forces. It is not able to change the way in which the forces are then projected into the computational domain and so it cannot influences the intensity of the generated vortices. For these reasons the turbulent flow behind the wind turbine still appears very dependent from the ϵ value, even when the model is applied.

Now it can be useful to consider the axial velocity profiles (both horizontally and vertically) in order to observe which is the effect of the gaussian projection function width on them and which are the benefits introduced by the application of the model. In the two charts below the horizontal profile of the axial velocity for both the standard version of SOWFA and the one in which the model is implemented is reported. Four different ϵ values are considered. The distance in correspondence of which the velocity was sampled is equal to 3 diameters.

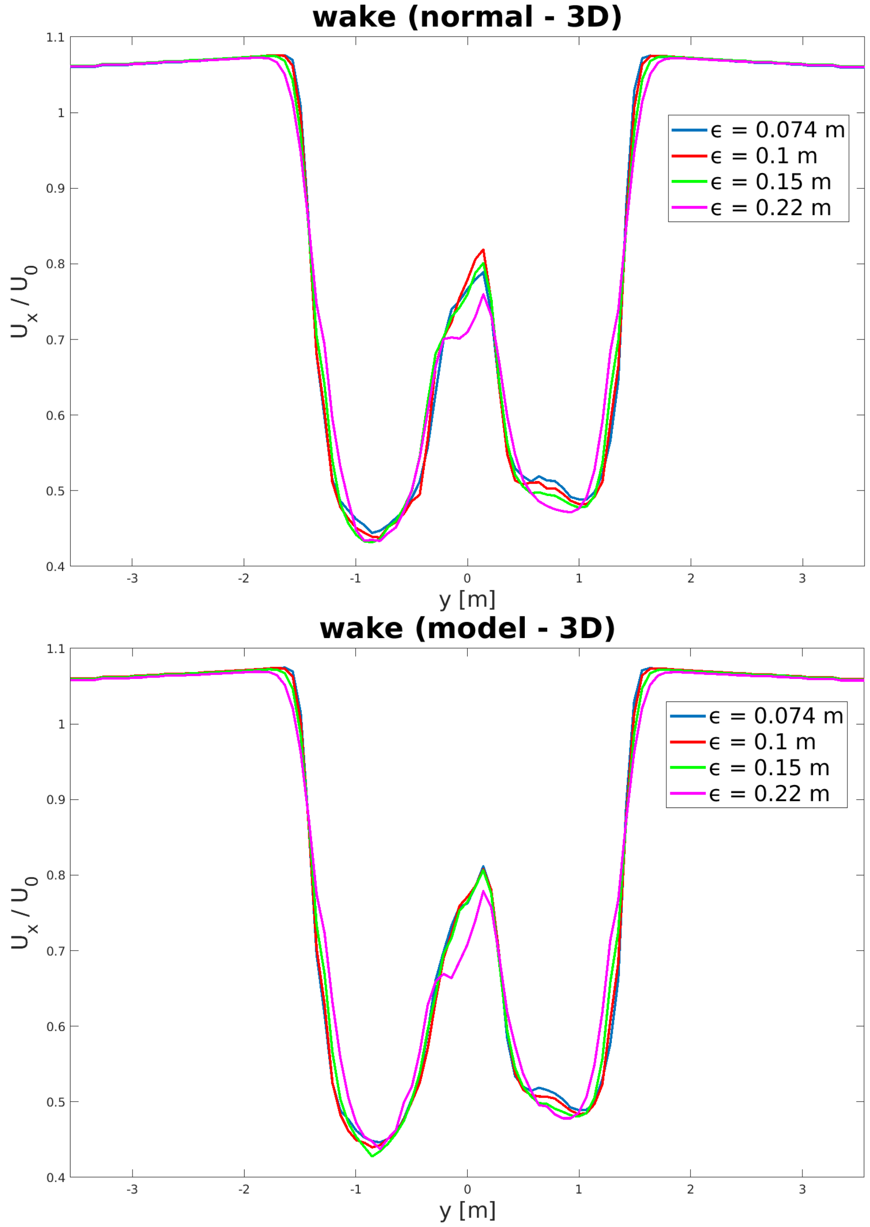

Figure 6.4. Horizontal axial velocity profile

The first thing that can be noted by looking at graphs is that the ϵ-dependence for the standard version of SOWFA is much less visible than when the analysis of the wind turbine performances was performed. This leads also to a less recognizable effectiveness of the model in decreasing this dependence. Nevertheless, by observing the second image it is possible to note that in the central part the curves related to the different ϵ values are closer one each other. This seems to happen, even if in a less intense way, also in the zone on the right where the velocity is decreased due to the impact of the flow on the blades.

The same behaviour can be found also by considering the profile of the axial velocity in the vertical direction. This is shown in the two images below.

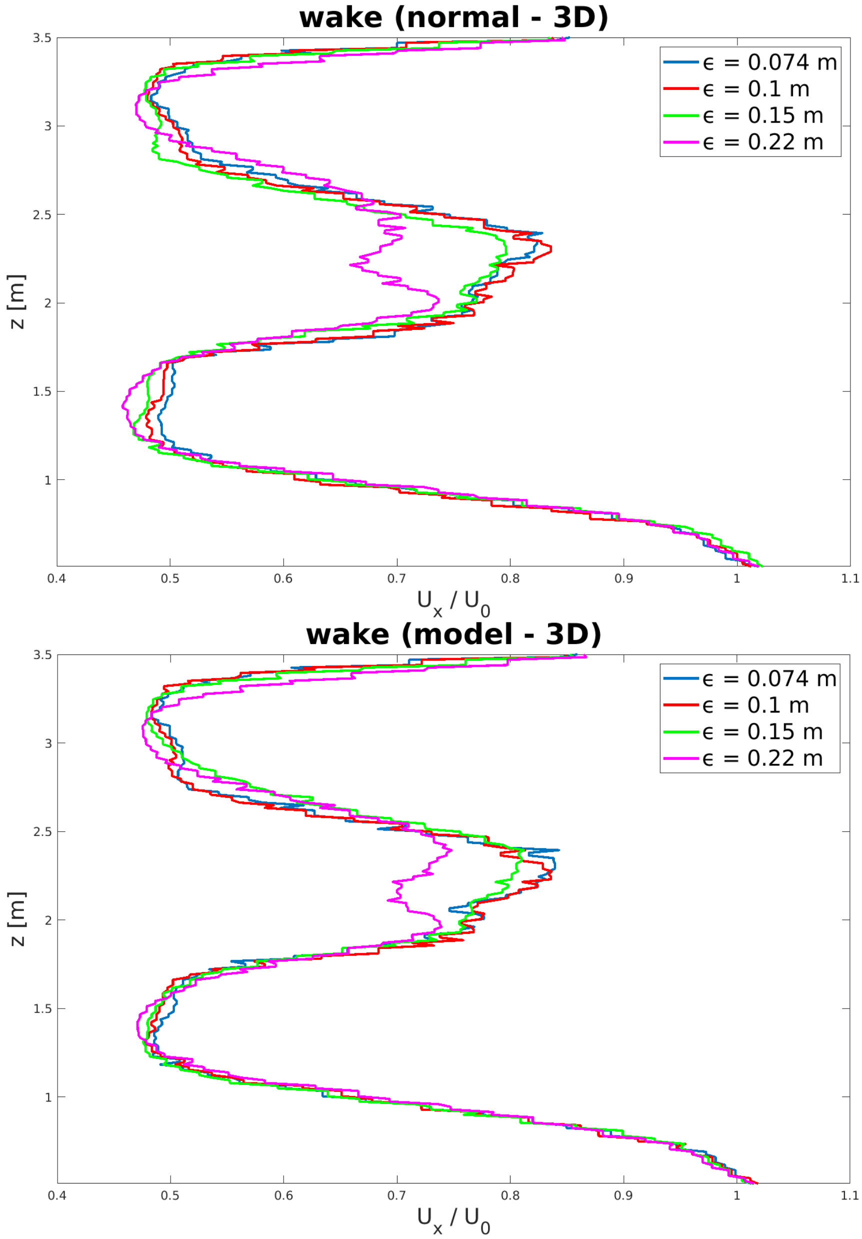

Figure 6.5. Vertical axial velocity profile

Once again, by looking at the second chart, the curves related to the different ϵ values seems to be a bit closer one each other. This means that the dependence from the gaussian projection function width chosen is reduced.

An effective method to recognize the influence of the model on the flow could be represented by the comparison between the standard version of SOWFA and the one with the model implemented, considering the two extreme ϵ values (0.074 m and 0.22

m) in separated charts.
In the two images below is in fact represented the comparison of the horizontal axial velocity profiles.

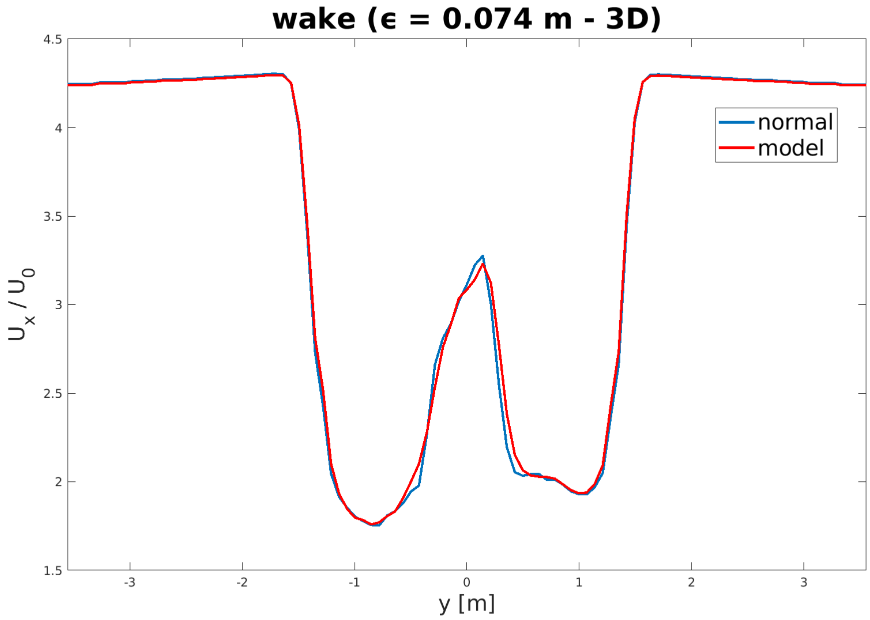

Figure 6.6. Comparison of the horizontal axial velocity profile coming from the standard version of SOWFA and from the model implementation for $\epsilon = 0.074$ m

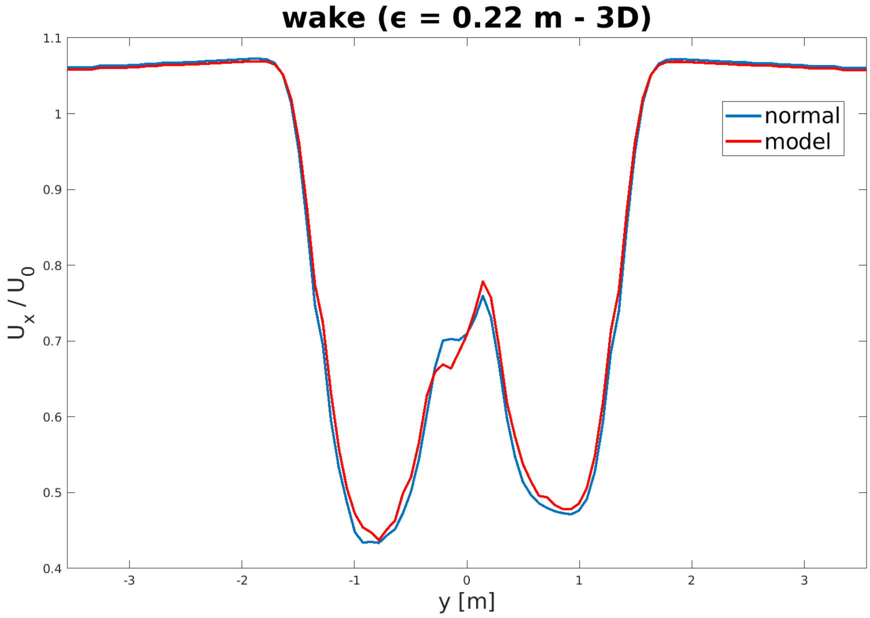

Figure 6.7. Comparison of the horizontal axial velocity profile coming from the standard version of SOWFA and from the model implementation for $\epsilon = 0.22$ m

It can be seen that in the first chart the curves seems to be almost overlapped,

whereas in the second one a certain difference between them can be noted. As already mentioned, this happens because $\epsilon = 0.074$ m is closer to the ϵ_{opt} value than $\epsilon = 0.22$ m. In fact, the higher is the value of the gaussian projection function width the higher is the intensity of the correction to the incoming velocity and the wider is the difference between the results coming from the standard version of SOWFA and the ones coming from the implementation of the model.
Obviously, the same comments can be made also by considering the vertical profile of the axial velocity.

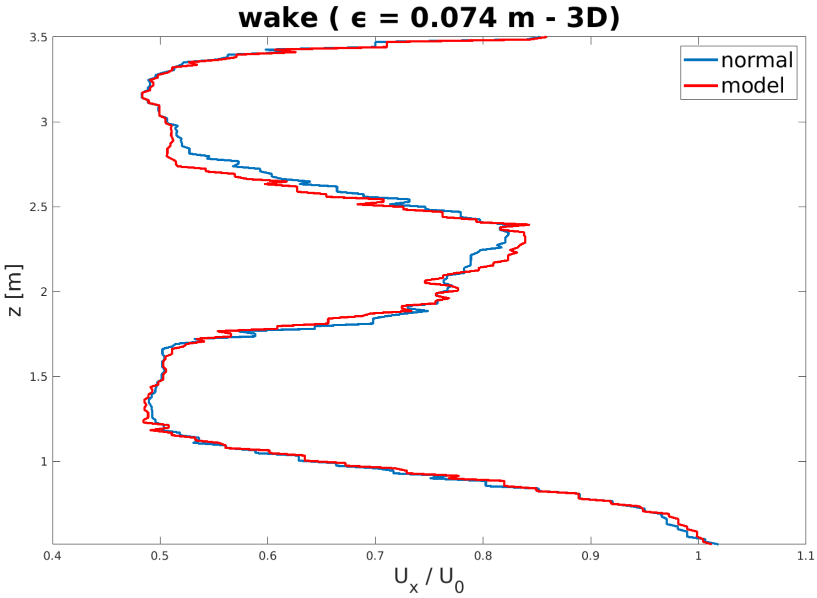

Figure 6.8. Comparison of the vertical axial velocity profile coming from the standard version of SOWFA and from the model implementation for $\epsilon = 0.074$ m

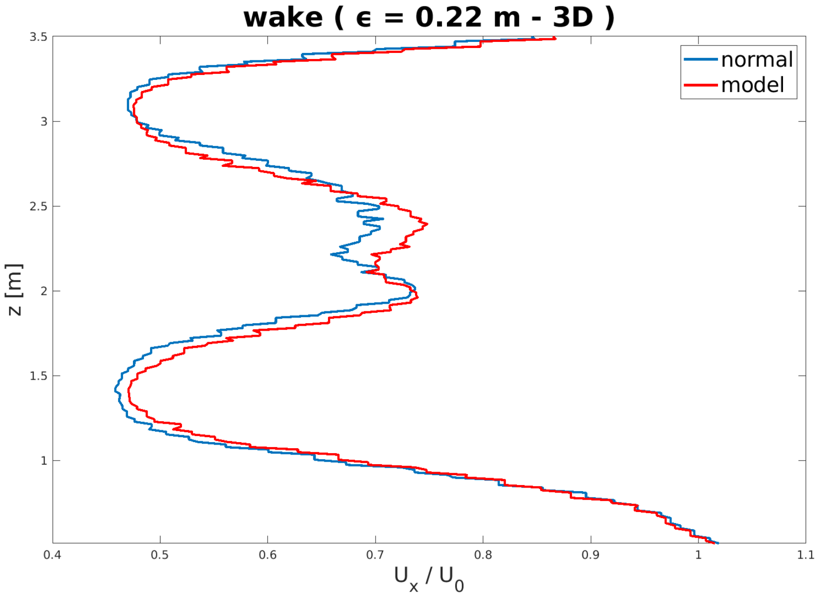

Figure 6.9. Comparison of the vertical axial velocity profile coming from the standard version of SOWFA and from the model implementation for $\epsilon = 0.22$ m

The curves of the first chart are again almost overlapped, whereas a certain distance can be observed between the two of the second image. This denotes a more intense correction introduced by the model for the second case.

Chapter 7

Conclusions and Future Works

7.1 Conclusions

The AL method has brought, since its introduction in 2002, enormous advantages to the wind turbines modeling. However, its big limitation is the high dependence from the different parameters concerning it that need to be set. One of the most important parameters is the width (ϵ) of the gaussian function used for projecting the forces in the area surrounding the blades. This parameter acts also on the intensity of the generated vortices and so it influences the downwash phenomenon inside the computational domain too. This causes the fact that, with an ϵ value higher than the optimal one (as usually happens in wind farm simulations), the predicted performances are overestimated.

The problem brought two scientists, Martinez and Meneveau, to the development of a model based on the Filtered Lifting Line Theory [3], with the aim of trying to solve it. They applied it on different fixed wings subjected to a flow and they obtained very good results. The performances of the wings appeared to be independent of the width of the gaussian function and almost equal to the ones reachable with the optimal value.

The aim of this thesis work was to implement the model in SOWFA, the Simulator for Offshore Wind Farm Applications, in order to see if the same results obtained with a fixed wing could be reached also in the case of a wind turbine. Two different options for the implementation were considered. The first one seems to be more effective in making the simulations independent of the ϵ value, but it is not able to influence the flow: the correction is applied only on the outputs of the machine operation, whereas the flow still feels the uncorrected forces. The second one instead is a bit less effective for what regards the independence from the ϵ value, but it introduces also a variation in the flow field. Both the options of the model were tested with two different machines: the NREL 5 MW wind turbine, a turbine designed by NREL that can be representative of typical utility-scale multimegawatt turbines, and the scaled version of the DTU 10 MW reference wind turbine, experimentally tested during the UNAFLOW project in the wind tunnel of POLIMI. From the simulations very good results were reached. The dependence from the gaussian projection function width decreases a lot with respect to the standard version of SOWFA. The model seems to be effective in representing the effect of the vortices on the zone at the inlet of

the machine. However, especially when considering the second option, the complete independence from the ϵ value has not yet been reached.
Only for the scaled version of the DTU 10 MW the wake analysis was performed too. This was done in order to observe the effect of the model on the flow (considering therefore the second option). The variations in the flow introduced for the application of the model are clearly visible, but its effect on the ϵ-dependence is less recognizable with respect to the performances analysis. The wake in fact is highly affected by the turbulent structures generated by the rotation of the blades. The model is not able to act on them, but it causes a variation only in the computed performances, correcting the angle of attack at the inlet. This is probably the reason for which the effect of the model is much more visible by looking at the obtained local and global output quantities, than by analysing the flow and the turbulent structures that characterize it.
Finally, two different meshes were taken into account for both the wind turbines. This was done to understand if the model can have any effect also on the way in which the grid refinement influences the performances of the simulated machines. However, by looking at the results with both the meshes, it is possible to deduce that this does not happen. Comparing in fact the results coming from the first and the second mesh, the way in which they change by increasing (or decreasing) the level of refinement of the mesh is the same when considering the standard version of SOWFA and the one with the model implemented. This means that it is not able to have any effect on the grid resolution influence.
Hence, in conclusion, the model has proved to be very effective in reducing the dependence from the gaussian projection function width, without having any influence on the effect of the grid resolution on the final results.

7.2 Future Works

With the implementation of the model in SOWFA, big improvements with respect to the basic AL approach have been observed. The reduction of the ϵ-dependence was considerable and this allowed to almost solve an important problem that affects wind farm simulations. Nevertheless, other adjustments can be made in order to improve more and more the code. The dependence on the gaussian projection function width, even if significantly reduced, was not completely eliminated. Some modifications can therefore be added and several other tests need to be performed in order to try to reach even better results. This has to be done especially for the second option for the implementation of the model. As deeply explained in this thesis work, it is in fact the one able to influence the flow field. An optimization of the code could lead to flow conditions closer and closer to the real ones. This is extremely useful when more than one machine need to be simulated. A realistic representation of the incoming flow conditions and an ϵ-dependence more and more decreased could allow to reach always the optimal conditions even with a large number of wind turbines tested at the same time.
In addition, the model could be tested considering different configurations. For this thesis work in fact only one fixed value for the rotational velocity has been considered. Other simulations could be performed by varying that value, in order to observe if

anything changes in the ϵ-dependence. Moreover, also a control strategy could be introduced. Until now, in fact, it was not considered in order to highlight only the aerodynamic aspects. However, its introduction would lead to simulations closer and closer to the reality and would make the implementation of the model more and more useful from a practical point of view.

Furthermore, a larger number of machines could be tested. In this work only one was taken into account, but, by increasing the number of the wind turbines that work at the same time, the effectiveness of the model on an entire simulated wind farm could be verified.

In conclusion, the model has proven to be greatly effective in decreasing the dependence of the final results from the gaussian projection function width, but it was shown that the way in which the computed performances varies with the grid resolution level is not influenced by the introduction of the model. A future work could be represented in fact by the introduction of some modifications that allow to reach results not only independent of the ϵ value, but also of the grid refinement level. This would lead to very big advantages: a wind farm could be simulated always in optimal conditions, whatever is the ϵ value, and with reasonable computational costs, much lower than the current ones.

Appendix A

Appendix: computeBladeFilteredWindVectors

Here below the part of the code related to the *computeBladeFilteredWindVectors* function is reported:

```
void horizontalAxisWindTurbinesALMAdvanced::
computeBladeFilteredWindVectors()
{

forAll(bladeWindVectors, i)
{
int m = turbineTypeID[i];
// Proceed blade by blade.
forAll(bladeWindVectors[i], j)
{
forAll(bladeWindVectors[i][j], k)
{
vector bladeWindVectorsInt = bladeWindVectors[i][j][k];

// Zero the wind vector.
bladeWindVectors[i][j][k] = vector::zero;

// Now put the velocity in that cell into blade-oriented
//coordinates
// and add on the velocity due to blade rotation.
bladeWindVectors[i][j][k].x() = (bladeAlignedVectors[i][j][0] &
bladeWindVectorsInt);
bladeWindVectors[i][j][k].y() = (bladeAlignedVectors[i][j][1] &
bladeWindVectorsInt) + (rotorSpeed[i] * bladePointRadius[i][j][k]
* cos(PreCone[m][j]));
bladeWindVectors[i][j][k].z() = (bladeAlignedVectors[i][j][2] &
bladeWindVectorsInt);
// Find the local velocity magnitude compose of only the
//axial and tangential flow (do not include the radial
//(along blade span) flow).
```

```
// Get the angle of the wind with respect to rotor plane
//tangent direction.
scalar windAng = Foam::atan2(bladeWindVectors[i][j]
[k].x(),bladeWindVectors[i][j][k].y())/degRad;

// Angle of attack is local angle of wind with respect
//to rotor plane tangent minus local twist.
bladePointAlpha[i][j][k] = windAng - bladePointTwist[i][j][k] -
bladePitch[i];
bladePointAlphaNoCorrection[i][j][k] = bladePointAlpha[i][j][k];
// This quantity is saved in order to then be stored
//in the postProcessing file
bladeWindVectorsSampled[i][j][k]=bladeWindVectors[i][j][k];
if (bladePointClOld[i][j][k]==-1)
{
bladePointClOld[i][j][k]=interpolate(bladePointAlpha[i][j][k],
airfoilAlpha[bladePointAirfoil[i][j][k]],
airfoilCl[bladePointAirfoil[i][j][k]]);

bladePointVmag[i][j][k]=Foam::pow((Foam::pow(bladeWindVectors[i]
[j][k].x(),2) + Foam::pow(bladeWindVectors[i][j][k].y(),2)),0.5);
}
else
{
bladePointClOld[i][j][k] = 0.1 * bladePointCl[i][j][k]
+ 0.9 * bladePointClOld[i][j][k];
// without the under-relaxation some numerical issues
//arise

}

G[i][j][k]=0.5 * bladePointClOld[i][j][k] * bladePointVmag[i][j]
[k] * bladePointVmag[i][j][k] * bladePointChord[i][j][k];
// In order to compute G the quantities at the
//previous time are considered (For the first
//time step the quantities at the current time
//step are used)
}
}
}
forAll(bladeWindVectors, i)
{
forAll(bladeWindVectors[i], j)
{
forAll(bladeWindVectors[i][j], k)
{

if(k==0)
```

```
{
dG[i][j][k]=G[i][j][k];
}
else if (k==numBladePoints[i]-1)
{
dG[i][j][k]=-G[i][j][k];
}
else
{
dG[i][j][k]=0.5*(G[i][j][k+1]-G[i][j][k-1]);
}
}
}
}
// Compute numerically the new (not yet relaxed) induced
//perturbation velocities for the current epsilon (LES)
//and for the optimal one (OPT)
forAll(bladeWindVectors, i)
{
int m = turbineTypeID[i];
// Proceed blade by blade.
forAll(bladeWindVectors[i], j)
{
forAll(bladeWindVectors[i][j], k)
{
scalar sumLES=0;
scalar sumOpt=0;
for (int n = 0; n < numBladePoints[i]; n++)
{
if (bladePointRadius[i][j][k] == bladePointRadius[i][j][n])
{
sumLES+=0;
sumOpt+=0;
}
else

{
scalar epsThickness = bladeEpsilon[i][0];


sumLES+=(-1/bladePointVmag[i][j][n])*dG[i][j][n]*(1/
(4*Foam::constant::mathematical::pi*(bladePointRadius[i][j][k]-
bladePointRadius[i][j][n]))*(1 -
(Foam::exp(-(Foam::pow((bladePointRadius[i][j][k]-
bladePointRadius[i][j][n]),2)) /
(Foam::pow((epsThickness),2))))));

sumOpt+=(-1/bladePointVmag[i][j][n])*dG[i][j][n]*(1/
(4*Foam::constant::mathematical::pi*(bladePointRadius[i][j][k]-
bladePointRadius[i][j][n]))*(1 -
```

```
(Foam::exp(-(Foam::pow((bladePointRadius[i][j][k]-
bladePointRadius[i][j][n]),2)) /
(Foam::pow((0.25*bladePointChord[i][j][n]),2))))));
}
}
// Apply underRelaxation
bladePointPerturbation[i][j][k]=sumOpt-sumLES;
if (bladePointPerturbationOld[i][j][k]!=0)
{
bladePointPerturbation[i][j][k]=
0.1*bladePointPerturbation[i][j][k]+
0.9*bladePointPerturbationOld[i][j][k];
}
bladePointPerturbationOld[i][j][k]=sumOpt-sumLES;

// The vector for the correction is here computed
vector notInfluencedVelocityParallelVector =
bladeAlignedVectors[i][j][0] *
bladeWindVectors[i][j][k].x() + bladeAlignedVectors[i][j][1] *
bladeWindVectors[i][j][k].y();
notInfluencedVelocityParallelVector =
notInfluencedVelocityParallelVector/
mag(notInfluencedVelocityParallelVector);
vector bladePointPerturbationVector =
notInfluencedVelocityParallelVector ^
bladeAlignedVectors[i][j][2];
bladePointPerturbationVector = bladePointPerturbation[i][j][k]
* bladePointPerturbationVector;
// get the new wind vectors
bladeWindVectors[i][j][k] = bladeWindVectors[i][j][k] +
bladePointPerturbationVector;
}
}
}
}
```

Acronyms

POLIMI	Politecnico di Milano
FOWT	Floating Offshore Wind Turbine
BEM	Blade Element Momentum
CFD	Computational Fluid Dynamics
DNS	Direct Numerical Simulations
LES	Large Eddy Simulations
RANS	Reynolds Averaged Navier Stokes
SGS	Subgrid-scale
PISO	Pressure-Implicit with Splitting of Operators
EVM	Effective Velocity Model
NREL	National Renewable Energy Laboratory
SOWFA	Simulator for Offshore Wind Farm Applications
ALM	Actuator Line Method
ADM	Actuator Disk Method
FR	Fully Resolved
GWEC	Global Wind Energy Council
GHG	Green House Gases
CAE	Computer-aided engineering
GAMG	Generalised Algebraic Multi-Grid
TNO	The Netherlands Organisation for applied scientific research
DTU	Technical University of Denmark
USTUTT	University of Stuttgart
UNAFLOW	Unsteady Aerodynamics of FLOating Wind turbines

Bibliography

[1] M. J. Churchfiled, "An advanced actuator line method for wind energy applications and beyond," *AIAA SciTech Forum*, 2017.

[2] L. Martìnez-Tossas, M. J. Churchfiled, and C. Meneveau, "Optimal smoothing length scale for actuator line models of wind turbine blades based on gaussian body force distribution," *WIND ENERGY*, 2017.

[3] L. Martìnez-Tossas and C. Meneveau, "Filtered lifting line theory and application to the actuator line model," *Journal of Fluid mechanics*, vol. 863, pp. 269–292, 2019.

[4] L. Martìnez-Tossas, M. J. Churchfiled, and C. Meneveau, "A highly resolved large-eddy simulation of a wind turbine using an actuator line model with optimal body force projection," *Journal of Physics*, 2016.

[5] GWEC, "Global wind report," 2021.

[6] J. N. Sørensen and W. K. Carsten, "A model for unsteady rotor aerodynamics," *Journal of fluids engineering*, 1995.

[7] J. N. Sørensen and W. Z. Shen, "Numerical modelling of wind turbine wakes," *Journal of fluids engineering*, 2002.

[8] E. Kalvig, S Manger and B. Hjertager, "Comparing different CFD wind turbine modelling approaches with wind tunnel measurements," *Journal of fluids engineering*, 2014.

[9] P. Schito, "Large eddy simulation of wind turbines: interaction with turbulent flow," PhD Thesis, Politecnico di Milano, 2012.

[10] L. Bernini and M. M. Caccialanza, "Development of the effective velocity model for wind turbines aerodynamics numerical simulation through an actuator line approach," Master Thesis, Politecnico di Milano, 2014.

[11] C. Muscari, "An actuator line model for wind farm performance evaluation," Master Thesis, Politecnico di Milano, 2019.

[12] H. Rahimi, J. G. Schepers, W. Z. Shen, N. Ramos García, M. S. Schneider, C. J. Micallef, D andSimao Ferreira, E. Jost, L. Klein, and I. Herráez, "Evaluation of different methods for determining the angle of attack on wind turbines blades with CFD results under axial inflow conditions," *Renewable Energy*, vol. 125, pp. 866–876, 2018.

[13] R. Merabet and E. Laurendeau, "Parametric study on the velocity sampling techniques for the actuator line method in 2D," *AIAA SciTech Forum*, 2019.

[14] P. Jha, M. J. Churchfiled, P. J. Moriarty, and S. Schmitz, "Accuracy of state-of-the-art actuator-line modeling for wind turbine wakes," 51^{st} *AIAA Aerospace Sciences Meeting including the New Horizons Forum and Aerospace Exposition*, January 2013.

[15] M. J. Churchfiled, P. J. Moriarty, S. Schmitz, and P. Jha, "Guidelines for volume force distributions within actuator line modeling of wind turbines on large-eddy simulation-type grids," *Journal of Solar Energy Engineering*, August 2014.

[16] M. O. L. Hansen, *Aerodynamics of Wind Turbines.* Earthscan, 2^{nd} edition, 2008.

[17] J. F. Manwell, J. G. McGowan, and A. L. Rogers, *Wind Energy explained.* Wiley, 2^{nd} edition, 2009.

[18] M. Sathyajith, *Wind Energy, Fundamentals, Resource Analysis and Economics.* Springer, 2006.

[19] J. H. Ferziger and M. Perić, *Computational Methods for Fluid Dynamics.* Springer, 3^{rd} edition, 2002.

[20] H. Versteeg and W. Malalasekera, *An Introduction to Computational Fluid Dynamics, The Finite Volume Method.* Pearson, 2^{nd} edition, 2007.

[21] J. D. M. Anderson, *Computational Fluid Dynamics, The basics with applications.* McGraw-Hill, 1995.

[22] G. Persico and G. Montenegro, "Lecture notes of the course of modeling techniques for fluid machines."

[23] "OpenFOAM v7 User Guide," https://cfd.direct/openfoam/user-guide/.

[24] H. Jasak, A. Jemcov, and Z. Tukovic, "OpenFOAM: A C++ library for complex physics simulations," *International Workshop on Coupled Methods in Numerical Dynamics*, 2007.

[25] A. Mittal, K. Sreenivas, L. K. Taylor, and L. Hereth, "Improvements to the actuator line modeling for wind turbines," *33rd Wind Energy Symposium*, 2015.

[26] S. Xie, "An actuator-line model with lagrangian-averaged velocity sampling and piecewise projection for wind turbine simulations," *John Wiley & Sons*, January 2021.

[27] M. Shives and C. Crawford, "Mesh and load distribution requirements for actuator line cfd simulations," *Wind energy*, vol. 16, pp. 1183–1196, 2012.

[28] M. Churchfield, S. Lee, and P. Moriarty, "Overview of the Simulator fOr Wind Farm Application (SOWFA)," 21^{st} May 2012.

[29] SOWFA, https://github.com/NREL/SOWFA.

[30] N. Troldborg, “Actuator line modeling of wind turbine wakes,” PhD Thesis, DTU, June 2008.

[31] J. Jonkman, S. Butterfield, W. Musial, and G. Scott, “Definition of a 5-MW reference wind turbine for offshore system development,” *National Renewable Energy Laboratory*, February 2009.

[32] I. Bayati, M. Belloli, L. Bernini, and A. Zasso, “Aerodynamic design methodology for wind tunnel tests of wind turbine rotors,” *Journal of Wind Engineering and Industrial Aerodynamics*, vol. 167, pp. 217–227, 2017.

[33] C. Bak, F. Zahle, R. Bitsche, T. Kim, A. Yde, L. C. Heriksen, M. H. Hansen, J. P. A. A. Balsques, M. Gaunaa, and A. Natarajan, “Description of the DTU 10 MW reference wind turbine,” *DTU Wind Energy*, 2013.

[34] I. Bayati, M. Belloli, L. Bernini, D. M. Boldrin, K. Boorsma, M. Caboni, M. Cormier, R. Mikkelsen, T. Lutz, and A. Zasso, “UNAFLOW project: UNsteady Aerodynamics of FLOating Wind turbines,” *Journal of Physics*, 2018.

[35] L. A. Martínez, S. Leonardi, and M. J. Churchfield, “Large eddy simulations of the flow past wind turbines: actuator line and disk modeling,” *Wind energy*, vol. 18, pp. 1047–1060, 2015.

[36] S. Mancini, “An experimental, analytical and numerical study of FOWT’s unsteady aerodynamics,” Master Thesis, Politecnico di Milano, 2020.

[37] A. Frigerio, “Advanced simulation for wind farm applications,” Master Thesis, Politecnico di Milano, 2017.

[38] J. N. Sørensen and K. O. Dag, “A new tip correction for actuator line computations,” *Wind Energy*, vol. 23, pp. 148–160, 2020.

[39] A. Robertson, R. Bergua, A. Fontanella, and J. Jonkman, “OC6 phase III definition document.”

[40] EWEA, “Wind energy scenarios for 2030,” August 2015.

[41] L. A. Martínez, S. Leonardi, M. J. Churchfield, and P. J. Moriarty, “A comparison of actuator disk and actuator line wind turbine models and best practices for their use,” 50^{th} *AIAA Aerospace Sciences Meeting*, January 2012.

[42] W. Z. Shen, M. O. L. Hansen, and J. N. Sørensen, “Determination of the angle of attack on rotor blades,” *John Wiley & Sons*, 2008.

[43] L. A. Martínez and S. Leonardi, “Wind turbine modeling for computational fluid dynamics,” *National Renewable Energy Laboratory*, 2012.